PRESSURE DISTRIBUTION MEASUREMENTS ON SEVERAL RIGID HYPERFLO MODELS AT MACH 3.0 AND 4.0

R. A. NOREEN
R. P. HOSKER, JR.

UNIVERSITY OF MINNESOTA

This document is subject to special export controls and each transmittal to foreign governments or foreign nationals may be made only with prior approval of the Vehicle Equipment Division (FDF), Air Force Flight Dynamics Laboratory, Wright-Patterson AFB, Ohio.

FOREWORD

This report was prepared by the Department of Aeronautics and Engineering Mechanics of the University of Minnesota in compliance with U. S. Air Force Contract No. AF 33(615)-5029, "Theoretical Deployable Aerodynamic Decelerator Investigations," Task 606503, "Parachute Aerodynamics and Structures," Project 6065, "Performance and Design of Deployable Aerodynamic Decelerators."

The work accomplished under this contract was sponsored jointly by U. S. Army Natick Laboratory, Department of the Army; Bureau of Aeronautics and Bureau of Ordnance, Department of the Navy; and Air Force Systems Command, Department of the Air Force and was directed by a Tri-Service Steering Committee concerned with Aerodynamic Retardation. The work was administered under the direction of the Recovery and Crew Station Branch, Air Force Flight Dynamics Laboratory, Research and Technology Division. Mr. James H. DeWeese was the project engineer.

The study was conducted under the direction of Professor H. G. Heinrich and in cooperation with Messrs. E. L. Haak and R. J. Niccum. Several students of Aerospace Engineering of the University of Minnesota participated in the performance of the tests and data reduction. The authors wish to express their gratitude to all who rendered their services to the accomplishment of this work.

The manuscript was released by the authors in June 1967 for publication as an AFFDL Technical Report.

This technical report has been reviewed and is approved.

GEORGE A. SOLT, JR.
Chief, Recovery and Crew Station Branch
AF Flight Dynamics Laboratory

ABSTRACT

The internal and external surface pressures on rigid wind tunnel models of Hyperflo canopies of 5%, 10%, and 15% geometric porosity, with mesh and grid porous areas, were measured, and Schlieren flow photographs were taken. The measurements were conducted in a 12 in. x 12 in. supersonic wind tunnel in freestream and in the wake of a cone-cylinder forebody at Mach numbers of 3.0 and 4.0 and Reynolds numbers/ft from 0.86×10^6 to 2.99×10^6.

TABLE OF CONTENTS

PAGE

I. Introduction 1

II. Models 2

A. Canopy Design. 2

B. Pressure Distribution Models 3

C. Forebody Configuration 3

III. Test Program and Procedure 4

A. Porosity and Stand-off Distance Effects. . 4

B. Mach Number Effects. 4

C. Reynolds Number Effects. 4

IV. Results. 6

A. Comparison of Flow Photographs 6

B. Pressure Distributions Results 7

1. $M_\infty \doteq 3.0$, $Re/ft \doteq 2.12 \times 10^6$ 8

2. $M_\infty \doteq 3.0$, $Re/ft \doteq 1.10 \times 10^6$ 9

3. $M_\infty \doteq 4.0$, $Re/ft \doteq 2.99 \times 10^6$ 9

4. $M_\infty \doteq 4.0$, $Re/ft \doteq 1.36 \times 10^6$ 10

5. $M_\infty \doteq 4.0$, $Re/ft \doteq 0.86 \times 10^6$ 10

C. The Blown Wake 11

D. Pressure Measurements in the Canopy Near-Wake. 11

V. Summary. 12

VI. References 14

Appendix I - Calculation of Canopy Parameters. 74

Appendix II - Flow Coefficient Measurement . . 83

Appendix III - $M_\infty \doteq 3.0$ Wake Survey. 87

ILLUSTRATIONS

FIGURE		PAGE
1.	Established Profile of Hyperflo Parachute. . .	15
2.	Porous Region Parameters for Mesh-roofed and Grid-roofed Hyperflo Models.	16
3.	Exploded Views of the Hyperflo Models.	17
4.	Nominal Tap Location for all Tapped Hyperflo Models	18
5.	Sting for Internal Pressure Measurements ($\frac{1}{2}$ Scale).	19
6.	Sting for External Pressure Measurements ($\frac{1}{2}$ Scale).	20
7.	Method of Recessing Pressure Tap Tubes Into Canopy Surface	21
8.	Side and Top Views of Forebody	22
9.	Model Installed in the Wind Tunnel	23
10.	Schematic of a Hyperflo Model in the Forebody Wake	24
11.	Comparison of Normal and Blown Wakes ($M_\infty \doteq 4.0$, $X/D_B = 7$)	25
12.	Comparison of Mach 3 and Mach 4 ($X/D_B = 7$) . .	26
13.	Comparison of Reynolds Numbers ($M_\infty \doteq 3.0$, $X/D_B = 6$).	27
14.	Comparison of Mesh and Grid Models ($M_\infty \doteq 3.0$, $Re/ft \doteq 2.12 \times 10^6$, $X/D_B = 6$).	28
15.	Comparison of Models With and Without Pressure Taps ($M_\infty \doteq 3.0$, $Re/ft \doteq 2.12 \times 10^6$, $X/D_B = 6$).	29
16.	Comparison of Internal and External Pressure Tap Models ($M_\infty \doteq 3.0$, $Re/ft \doteq 2.12 \times 10^6$, $X/D_B = 6$).	30
17.	Comparison of 5% and 15% Models ($M_\infty \doteq 3.0$, $Re/ft \doteq 2.12 \times 10^6$, $X/D_B = 8$).	31
18.	Comparison of $X/D_B = 6$ and $X/D_B = 9$ ($M_\infty \doteq 3.0$, $Re/ft \doteq 2.12 \times 10^6$).	32

FIGURE		PAGE
19.	Comparison of Wake and Freestream Flow, Double Exposure Schlieren Photographs ($M_\infty \doteq 3.0$, $Re/ft \doteq 2.12 \times 10^6$)	33
20.	Schematic of Net Pressure Coefficient at $X/D_B = 6$ ($M_\infty \doteq 3.0$, $Re/ft \doteq 2.12 \times 10^6$)	34
21.	Schlieren Photographs at $X/D_B = 6$ ($M_\infty \doteq 3.0$, $Re/ft \doteq 2.12 \times 10^6$)	35
22.	Schematic of Net Pressure Coefficient at $X/D_B = 7$ ($M_\infty \doteq 3.0$, $Re/ft \doteq 2.12 \times 10^6$)	36
23.	Schlieren Photographs at $X/D_B = 7$ ($M_\infty \doteq 3.0$, $Re/ft \doteq 2.12 \times 10^6$)	37
24.	Schematic of Net Pressure Coefficient at $X/D_B = 8$ ($M_\infty \doteq 3.0$, $Re/ft \doteq 2.12 \times 10^6$)	38
25.	Schlieren Photographs at $X/D_B = 8$ ($M_\infty \doteq 3.0$, $Re/ft \doteq 2.12 \times 10^6$)	39
26.	Schematic of Net Pressure Coefficient at $X/D_B = 9$ ($M_\infty \doteq 3.0$, $Re/ft \doteq 2.12 \times 10^6$)	40
27.	Schlieren Photographs at $X/D_B = 9$ ($M_\infty \doteq 3.0$, $Re/ft \doteq 2.12 \times 10^6$)	41
28.	Schematic of Net Pressure Coefficient at $X/D_B = 11$ ($M_\infty \doteq 3.0$, $Re/ft \doteq 2.12 \times 10^6$)	42
29.	Schlieren Photographs at $X/D_B = 11$ ($M_\infty \doteq 3.0$, $Re/ft \doteq 2.12 \times 10^6$)	43
30.	Schematic of Net Pressure Coefficient at $X/D_B = \infty$ ($M_\infty \doteq 3.0$, $Re/ft \doteq 2.12 \times 10^6$)	44
31.	Schlieren Photographs at $X/D_B = \infty$ ($M_\infty \doteq 3.0$, $Re/ft \doteq 2.12 \times 10^6$)	45
32.	Schematic of Internal Pressure Coefficients for 10% Mesh and 10% Grid Models at $X/D_B = 6$ and 8 ($M_\infty \doteq 3.0$, $Re/ft \doteq 1.10 \times 10^6$)	46
33.	Schlieren Photographs of 10% Mesh and 10% Grid Models at $X/D_B = 6$ and 8 ($M_\infty \doteq 3.0$, $Re/ft \doteq 1.10 \times 10^6$)	47

ILLUSTRATIONS (CONT.)

FIGURE PAGE

34. Schematic of Net Pressure Coefficients for 10% Mesh and 10% Grid Models at $X/D_B = 5, 6,$ and 7 ($M_\infty \doteq 4.0$, Re/ft $\doteq 2.99 \times 10^6$) 48

35. Schlieren Photographs of 10% Mesh and 10% Grid Models at $X/D_B = 5, 6,$ and 7 ($M_\infty \doteq 4.0$, Re/ft $\doteq 2.99 \times 10^6$). 49

36. Schematic of Net Pressure Coefficients for 10% Mesh and 10% Grid Models at $X/D_B = 8, 9,$ and ∞ ($M_\infty \doteq 4.0$, Re/ft $\doteq 2.99 \times 10^6$) 50

37. Schlieren Photographs of 10% Mesh and 10% Grid Models at $X/D_B = 8, 9,$ and ∞ ($M_\infty \doteq 4.0$, Re/ft $\doteq 2.99 \times 10^6$). 51

38. Schematic of Internal Pressure Coefficients for 10% Mesh and 10% Grid Models at $X/D_B = 6$ and 7 ($M_\infty \doteq 4.0$, Re/ft $\doteq 1.36 \times 10^6$) 52

39. Schlieren Photographs of 10% Mesh and 10% Grid Models at $X/D_B = 6$ and 7 ($M_\infty \doteq 4.0$, Re/ft $\doteq 1.36 \times 10^6$). 53

40. Schematic of Internal Pressure Coefficients for 10% Mesh and 10% Grid Models at $X/D_B = 8$ and ∞ ($M_\infty \doteq 4.0$, Re/ft $\doteq 1.36 \times 10^6$) 54

41. Schlieren Photographs of 10% Mesh and 10% Grid Models at $X/D_B = 8$ and ∞ ($M_\infty \doteq 4.0$, Re/ft $\doteq 1.36 \times 10^6$). 55

42. Schlieren Photographs of 10% Mesh and 10% Grid Models at $X/D_B = 6, 8,$ and ∞ ($M_\infty \doteq 4.0$, Re/ft $\doteq 0.86 \times 10^6$). 56

43. Schlieren Photographs of 10% Grid Model at $X/D_B = 7$ ($M_\infty \doteq 4.0$). 57

44. Maximum X/D_B, Maximum Re/ft, Blown Wake Condition for a 10% Model at Mach 3 and Mach 4 58

45. Canopy Near Wake Pressure for 5% Mesh and Grid Models at $X/D_B = 6, 7, 8, 9,$ and 11 ($M_\infty \doteq 3.0$, Re/ft $\doteq 2.12 \times 10^6$) 59

46. Canopy Near Wake Pressures for 10% and 15% Mesh and Grid Models at $X/D_B = 6$ and 8 ($M_\infty \doteq 3.0$, Re/ft $\doteq 2.12 \times 10^6$) 60

ILLUSTRATIONS (CONT.)

FIGURE		PAGE
47.	Scheme of Mesh-roofed Hyperflo Canopy Model. .	75
48.	Geometric Relations on Circle Covered by Solid Ribbons of Width B_R and Spacing ℓ_R	77
49.	Flow Coefficient Measurement Apparatus	84
50.	Flow Coefficient of Ribbon Grids as a Function of Grid Ribbon Width	86
51.	Schematic of Cruciform Rake as Used for Forebody Wake Survey at $M_\infty \doteq 3.0$ (3/4 Scale), and Dimensionless Rake Probe Location Relative to Center Line.	88
52.	Wake Static to Freestream Total Pressure Ratios in the Horizontal Plane ($M_\infty \doteq 3.0$). . .	92
53.	Wake Total Pressure Ratios in the Horizontal Plane ($M_\infty \doteq 3.0$)	93
54.	Wake Static to Freestream Total Pressure Ratios in the Vertical Plane ($M_\infty \doteq 3.0$). . . .	94
55.	Wake Total Pressure Ratios in the Vertical Plane ($M_\infty \doteq 3.0$)	95

TABLES

TABLE		PAGE
I.	Coordinates of Established Hyperflo Parachute Profile.	61
II.	Exact Tap Locations for the Hyperflo Models.	62
III.	Test Program	63
IV.	Pressure Coefficients at $X/D_B = 6$ ($M_\infty \doteq 3.0$, $Re/ft \doteq 2.12 \times 10^6$).	64
V.	Pressure Coefficients at $X/D_B = 7$ ($M_\infty \doteq 3.0$, $Re/ft \doteq 2.12 \times 10^6$).	65
VI.	Pressure Coefficients at $X/D_B = 8$ ($M_\infty \doteq 3.0$, $Re/ft \doteq 2.12 \times 10^6$).	66
VII.	Pressure Coefficients at $X/D_B = 9$ ($M_\infty \doteq 3.0$, $Re/ft \doteq 2.12 \times 10^6$).	67
VIII.	Pressure Coefficients at $X/D_B = 11$ ($M_\infty \doteq 3.0$, $Re/ft \doteq 2.12 \times 10^6$).	68
IX.	Pressure Coefficients at $X/D_B = \infty$ ($M_\infty \doteq 3.0$, $Re/ft \doteq 2.12 \times 10^6$).	69
X.	Internal Pressure Coefficients for 10% Mesh and 10% Grid Models at $X/D_B = 6$ and 8 ($M_\infty \doteq 3.0$, $Re/ft \doteq 1.10 \times 10^6$)	70
XI.	Pressure Coefficients for 10% Mesh and 10% Grid Models at $X/D_B = 5$, 6, and 7 ($M_\infty \doteq 4.0$, $Re/ft \doteq 2.99 \times 10^6$).	71
XII.	Pressure Coefficients for 10% Mesh and 10% Grid Models at $X/D_B = 8$, 9, and ∞ ($M_\infty \doteq 4.0$, $Re/ft \doteq 2.99 \times 10^6$).	72
XIII.	Internal Pressure Coefficients for 10% Mesh and 10% Grid Models at $X/D_B = 6$, 7, 8, and ∞ ($M_\infty \doteq 4.0$, $Re/ft \doteq 1.36 \times 10^6$)	73
XIV.	Mesh-edge Coordinates for Hyperflo Models.	81
XV.	Construction Parameters for Ribbon Grid Hyperflo Models.	82
XVI.	Wake Pressure Ratios $X/D_B = 6$ and 7 ($M_\infty \doteq 3.0$)	89

TABLES (CONT.)

TABLE		PAGE
XVII.	Wake Pressure Ratios X/D_B = 8 and 9 ($M_\infty \doteq 3.0$)	90
XVIII.	Wake Pressure Ratios $X/D_B = \infty$ ($M_\infty \doteq 3.0$) . . .	91

SYMBOLS*

A	area
a	speed of sound
A_j	area of jth ribbon
A_m	area covered by wire mesh
A_p	area covered by perlon screen
A_R	total area covered by ribbons of grid model
A_1	area of canopy from roof center to lower edge of porous region
A_2	area of solid central polygon of the mesh model
A_λ	open area
B_R	width of support ribbons of mesh model
C_p	pressure coefficient
d	a diameter
D_B	base diameter of cone-cylinder forebody
D_p	canopy projected diameter
j	summation index
K	ratio of actual mass flow to ideal mass flow
$\overline{\underline{K}}$	ASME orifice coefficient (Ref 4)
ℓ_R	ribbon spacing on grid model
ℓ_1	arc length from roof center to lower mesh edge
ℓ_2	arc length from roof center to upper mesh edge
ℓ_3	arc length from upper to lower mesh edge
M_∞	freestream Mach number
$\dot{m}_a$	actual mass flow
$\dot{m}_i$	ideal mass flow

*As defined in Ref 1 where applicable.

SYMBOLS (CONT.)

n	number of non-porous support ribbons or gores
n_R	total number of ribbons to right or left of center
p_ℓ	local static pressure
p'_{o_ℓ}	local total pressure behind a normal shock wave
p_{o_∞}	freestream total pressure
p_∞	freestream static pressure
R	gas constant
Re	Reynolds number
R_p	$D_p/2$
r_G	radius of flat perforated grid
S_o	total canopy surface area
T	temperature
v	velocity
V_∞	freestream velocity
X	distance between forebody base and parachute model skirt plane
X_c/R_p	canopy profile dimensionless coordinate
Y	horizontal distance perpendicular to X
Υ	ASME expansion factor (Ref 4)
Y_c/R_p	canopy profile dimensionless coordinate
Z	vertical distance perpendicular to X
γ	ratio of specific heats
γ_a	specific weight
ρ	density
θ_j	see Fig 48
λ_a	aerodynamic porosity, ratio of total open area to canopy inlet area

SYMBOLS (CONT.)

λ_g	geometric porosity, ratio of total open area to total area
λ_m	geometric porosity of mesh
λ_{rg}	geometric porosity of ribbon grid

Subscripts

$(\ )_{rg}$	ribbon grid
$(\ )_m$	mesh
$(\ )_p$	perlon screen

Superscript

II	values from Ref 2

I. INTRODUCTION

The Hyperflo parachute has evolved as a supersonic decelerator after a large number of wind tunnel tests on many flexible models of slightly different designs. Recently, studies were completed on the effects of some of the design parameters on the performance of the Hyperflo parachute (Ref 2). Since knowledge of the pressure distribution on the surface of a parachute is of great importance in predicting or explaining parachute behavior, or for modification and improvement of a design concept, this study was initiated to determine the surface pressure distributions on rigid Hyperflo models under test conditions similar to those in Ref 2. To maintain as much similarity as possible, Mach and Reynolds numbers were duplicated as closely as wind tunnel facilities permitted, the profile of the rigid models in this study was obtained from flexible models, and the rigid models were scaled with the requirement that the porous roof allowed the same mass flow per unit area as that of the actual flexible parachutes.

II. MODELS

A. Canopy Design

Using data supplied by the procuring agency on textile Hyperflo parachutes of flat roof and isotensoid designs at various Mach numbers, and using data from Ref 2, an average profile for the canopy models was established (Fig 1, Table I). In accordance with wind tunnel requirements, the projected diameter of these models was set at 3.00 inches.

The models were constructed as bodies of revolution, with the porous area, composed of either mesh or a ribbon grid, entirely in the roof section. The geometric porosities, λ_g, of the mesh type models amounted to 5%, 10%, and 15%, corresponding to aerodynamic porosities, λ_a, of 14.3%, 28.6%, and 42.9%, respectively. Three grid-roofed models were constructed with sufficient porosity to provide the same mass flow as their counterpart mesh models. Methods of calculation (Appendix I) were developed to provide the necessary construction parameters, and the results are shown in Fig 2.

The requirement of equal mass flow results in geometric porosities for the grid-type canopies of 5.05%, 10.9%, and 16.8%, corresponding to aerodynamic porosities of 14.4%, 31.2%, and 48.0%, respectively. The differences in the porosities of the grid and mesh models is caused by the difference in supercritical discharge coefficients of the mesh and grid. For convenience, the models have been designated by their geometric porosities in this report.

The Hyperflo model canopies were spun in two pieces to the design profile from 0.031 in. thick type 304 stainless steel. A sandwich construction was employed for the wire mesh-covered porous regions. Sheets of 0.007 in. thick brass were formed to the correct profile, and eight gore panels, separated by 0.010 in. solid support ribbons, were removed. One such sheet was then placed on each side of a similarly formed piece of wire mesh, and this "sandwich" was soldered together. The top of a spun steel canopy was then removed and replaced by the mesh unit. For the grid-type models, sheets of 0.025 in. thick brass were perforated with square holes of 0.100 in. edge, and then formed to the desired profile. It was hoped that this procedure would approximate fairly well the deformation and stretching of a textile grid upon inflation. The formed grid was then attached to a canopy shell from which the corresponding roof region had been removed. Exploded views of typical assemblies are shown in Fig 3. Agreement of the actual model profiles with the design profile was found to be very good.

B. Pressure Distribution Models

Using the basic canopies described above, three sets of models of the nominal geometric porosities 10% and 15% were constructed. One set had external static pressure taps, another had internal static pressure taps, and the third was an untapped, or so-called "clean", configuration. This latter set of models was employed to evaluate the influence of the pressure taps upon the flow field about the canopies, with the aid of Schlieren photographs. In the case of the models of 5% nominal geometric porosity, only the tapped versions were constructed.

Each tapped model has twelve pressure taps whose nominal locations are shown in Fig 4; exact locations are given in Table II. Duplicate taps are located near the inlet, at the point of maximum diameter, and near the point corresponding to the lower mesh edge of a model of 10% geometric porosity. When the models were placed in the wind tunnel the pressure taps were in a vertical plane with Tap Number 1 at the top.

To minimize interference with the particular flow field to be studied, two different stings were designed (Figs 5 and 6). The pressure tap tubing ran through the hollow sting to the canopy. Portions of the tubing which crossed solid regions of the model were recessed into slots milled into the surface (Fig 7). The sting designed for internal flow measurements (Fig 5) was also equipped with a small pressure rake, with both static and total pressure probes.

All Hyperflo models were equipped with eight braided nylon suspension lines of 0.024 in. diameter, or 0.8% of the canopy diameter. The free length of these lines was 6.66 in., so that the line length to canopy projected diameter ratio was 2.22.

C. Forebody Configuration

The Hyperflo models were tested in the wake of a cone-cylinder forebody of base diameter $D_B = 1.20$ in., cone half-angle 13°, and total length of 7.428 in. (Fig 8). The canopy projected diameter to forebody diameter ratio was $D_P/D_B = 2.50$.

The forebody was mounted with its support wings horizontal. A hollow cylindrical extension of diameter 1.20 in. and length 1.20 in. was added to the forebody base when parachute models were tested at $X/D_B = 5$.

III. TEST PROGRAM AND PROCEDURE

The objectives of this study were to establish the pressure distributions on the Hyperflo parachute models described in the previous section and to determine the effects of variation of Mach and Reynolds numbers. The test program is shown in Table III.

A. Porosity and Stand-off Distance Effects

Pressure data was obtained at $M_\infty \doteq 3.0$, Re/ft $\doteq 2.12 \times 10^6$; for all models at six stand-off distances between forebody and parachute model, including the freestream condition $X/D_B = \infty$. This data enabled comparison of both porosity and stand-off distance effects.

B. Mach Number Effects

Ten percent porosity models at X/D_B's of 5, 6, 7, 8, 9, and ∞ were tested at $M_\infty \doteq 4.0$, Re/ft $\doteq 2.99 \times 10^6$, and compared to the Mach 3 data at the same Reynolds number in order to determine Mach number effects.

C. Reynolds Number Effects

The Reynolds number effects on the pressure distributions were obtained by testing at two Reynolds numbers per Mach number. At Mach 3 these Reynolds numbers/ft were 1.10×10^6 and 2.12×10^6. The Mach 4 tests were conducted at Reynolds numbers/ft of 1.36×10^6 and 2.99×10^6.

The test points at the lower Reynolds numbers and small X/D_B's in Table III are used to determine the conditions necessary for a diverging or "blown" forebody wake, which is defined by the lack of a trailing recompression shock wave from the forebody and the absence of a canopy bow shock wave (Ref 2).

The tests were conducted in a 12 in. x 12 in. blow-down wind tunnel at the University of Minnesota Rosemount Aeronautical Laboratories. For all conditions an atmospheric inlet was used, except at $M_\infty \doteq 4.0$, Re/ft $\doteq 2.99 \times 10^6$, where a high pressure inlet was employed.

Figure 9, a photograph of the wind tunnel with a side wall removed, shows the test setup with the Mach 4.0 nozzle blocks. Rotating the swept parachute model support and changing strut base plates provided the various stand-off distances, except for $X/D_B = 5$, where an extension was added to the forebody.

A thin steel wire served as a riser to connect the suspension line confluence point to either the base of the forebody or, in the freestream tests, a 0.025 in. wire stretched between the tunnel walls 15.5 in. upstream of the model.

The pressures on the model and the static and stagnation pressures of the wind tunnel were measured with a multi-tube mercury manometer board. The manometer board had a so-called guillotine clamp, which enabled taking pressures during a run, sealing the manometer board, and then reading the board indications after the run. The small diameter tubing between the model and the manometer board and the construction of the manometer board itself made accurate measurement of pressures less than 0.3 in. Hg abs. impossible. This determined the choice of the Re/ft $\doteq$ 2.99 x 10^6 at Mach 4.0.

Two or three wind tunnel runs where manometer board stabilization was reached provided the reported pressure readings. During one of these runs a flow photograph was obtained using a double-pass Schlieren system.

IV. RESULTS

A. Comparison of Flow Photographs

Figure 10 is a schematic drawing of the flow field for a typical test configuration at Mach 3.0. The flow is typical of a low-porosity decelerator combined with a slender forebody. Starting from the wake centerline and moving outward are: (1) the wake recompression shock; (2) the trailing shock from the forebody support wings; and (3) the support wing leading edge shock, the forebody bow shock, and the test rhombus boundary, all nearly superimposed because of the design and position of the forebody. The canopy has a strong, irregular, detached bow shock (4), with considerable interaction between the bow shock and the suspension lines. In view of the notation used before, the wake is defined as blown when there is no canopy bow shock (4), nor a wake recompression shock (1). As an illustration, Fig 11 shows a normal and a blown wake.

The Schlieren photographs have an exposure time of only several microseconds; hence, nearly all motion has been stopped. In reality, however, the canopy bow shock is constantly in motion with fairly small amplitudes but at several thousand cycles per second. Hence, any two Schlieren photographs of the same model at a given test condition will not be identical, but will show small changes in shock shape or position.

Figure 12 compares a 10% grid model at $X/D_B = 7$ for $M_\infty \doteq 3.0$, $Re/ft \doteq 2.12 \times 10^6$, and $M_\infty \doteq 4.0$, $Re/ft \doteq 2.99 \times 10^6$. The canopy bow shocks and flow fields are similar. However, the decrease in shock angle of all of the forebody shock waves due to the increase in Mach number is evident.

Two Reynolds numbers, $Re/ft \doteq 2.12 \times 10^6$ and $Re/ft \doteq 1.10 \times 10^6$, at $M_\infty \doteq 3.0$ are compared in Fig 13 for a 10% grid model. At $Re/ft \doteq 2.12 \times 10^6$, the sonic flow out of the grid spaces is clearly visible, while at the lower Reynolds number this flow cannot be seen. The wake recompression shocks are barely discernible, but indicate that there has been no change in wake geometry, nor is there a significant change in the canopy bow shock. Of course, the poorer resolution of the low Reynolds number pictures is due to the lower air density.

Schlieren photographs of a 10% mesh and 10% grid model at $M_\infty \doteq 3.0$, $Re/ft \doteq 2.12 \times 10^6$, and $X/D_B = 6$ are shown in Fig 14. The visible flow out of the grid spaces is the only noticeable difference between the two flow fields, and this is probably the consequence of the stronger individual jet streams between the ribbons.

Figure 15 compares the 10% mesh model without pressure taps to the 10% mesh model with pressure taps at $M_\infty \doteq 3.0$, $Re/ft \doteq 2.12 \times 10^6$, $X/D_B = 6$. The canopy bow shocks are slightly different, but these are instantaneous photographs and one should remember that the bow shocks are constantly shifting. Therefore, it cannot be concluded that pressure taps cause disturbances of the flow field. The canopy wake formation is clearly visible in Fig 15a, and Fig 15b shows that the small pressure rake hardly alters this wake.

The possible effects of the two different model supporting stings are compared at $M_\infty \doteq 3.0$, $Re/ft \doteq 2.12 \times 10^6$, in Fig 16; but the Schlieren photographs show no significant differences in either the canopy bow shocks or the wakes.

The canopy bow shocks on the 15% mesh and grid models were consistently more oblique than the shocks on the 5% and 10% models (Fig 17). The more oblique shock was also unstable. Occasionally, it would suddenly move into the position typical of the lower porosity models, remain there for a very short period of time, then return to the more oblique position. The frequency of this motion changed from just an occasional movement of the shock at low stand-off distances, to an almost continuous cyclic oscillation with approximately 10 cycles per second when the canopy model was suspended in freestream.

For the models with 5% and 10% porosity, the canopy bow shock also tended to become more oblique and less stable as stand-off distance was increased. This is illustrated in Fig 18 which compares the 10% mesh canopy at $X/D_B = 6$ and $X/D_B = 9$. At the higher stand-off distances, such as $X/D_B = 9$, 11, and ∞ , the canopy bow shock waves for the 5% and 10% models assume a shape somewhat similar to those of the 15% models but appear to be more stable.

Double exposure photographs (Fig 19) of the 10% mesh model at $X/D_B = 7$ and $X/D_B = \infty$, with an interval of about two seconds between exposures, indicate typical shock wave movements in the wake and in freestream. Figure 19b also shows a certain model vibration which is characteristic for all freestream experiments where considerable shock wave unsteadiness was observed.

B. Pressure Distribution Results

The pressure distributions were measured under the same Mach and Reynolds number conditions as described in the flow pattern study. In particular, these flow conditions are Mach number 3.0 with Reynolds numbers per foot of 2.12 and 1.10×10^6, and Mach number 4.0 with Reynolds numbers per foot of 2.99 x 10^6, 1.36 x 10^6, and 0.86 x 10^6. Details of these experiments are shown in the following sections and include tabulated values of the pressure coefficients, schematic representations of the pressures on the canopy profile and the appropriate Schlieren photograph of each test condition. The pressure readings taken on the surfaces of the models are presented as pressure coefficient C_p, where

$$C_p = \frac{P_\ell - P_\infty}{(\frac{1}{2}\rho V_\infty^2)} \quad .$$

The tabulated values of the internal and external pressure coefficients are averages from the individual taps from at least two wind tunnel runs. The net pressure coefficient is defined as the difference between the internal and external pressure coefficients. The pressure coefficients are shown schematically along the canopy profile by plotting a scaled length perpendicular to the canopy surface at the corresponding approximate pressure tap location. The uniform dashed line represents a C_p value of 1.0, and a dashed break in the curve drawn through the ends of the C_p vectors indicates that the pressure measured at that tap may be in error.

1. $M_\infty \doteq 3.0$, Re/ft $\doteq 2.12 \times 10^6$

Tables IV through IX and Figs 20 to 31 show the pressure distributions and Schlieren photographs for all models at X/D_B's of 6, 7, 8, 9, 11 and in freestream.

The pressure distributions are not exactly symmetric, which may be due to the irregular, unsteady canopy bow shock. The sharp drop in net C_p at the canopy inlet is due to the large positive external pressure, which is in some cases great enough to produce a negative net C_p at the inlet. However, over the remainder of the canopy surface, the external C_p's are quite uniform and have small negative values and produce only a small effect on the overall pressure distribution.

The most important conclusion to be drawn from the $M_\infty \doteq 3.0$, Re/ft $\doteq 2.12 \times 10^6$, data is that there are only very small changes in C_p over the range of test variables. The average net C_p, excluding the edge taps, is approximately 1.2. There is no distinct difference in the pressure distributions on the mesh and grid models, and only a very slight decrease, if any, of net C_p with increasing porosity. The net C_p decreases about 10% as the stand-off distance increases from $X/D_B = 6$ to $X/D_B = 11$. The freestream values are slightly higher than those of the stand-off distance $X/D_B = 11$ and closer to those associated with smaller stand-off distances.

The Schlieren photographs tend to support the pressure distribution results. The change in the canopy bow shock with increasing porosity did not cause a significant change in the pressure distributions, and the tendency for the shock to become more oblique at larger stand-off distances may be reflected in the decrease in C_p.

2. $M_\infty \doteq 3.0$, $Re/ft \doteq 1.10 \times 10^6$

Internal pressure distribution data at $M_\infty \doteq 3.0$, $Re/ft \doteq 1.10 \times 10^6$, is shown in Table X and Fig 32, with Schlieren photographs in Fig 33. The data is presented as before, but for the remainder of the program only 10% mesh and 10% grid models were tested, and in some cases pressures could not be measured because of manometer board limitations. Data was obtained at $X/D_B = 6$ and 8 to determine the effect of Reynolds number on the pressure distribution, and to establish the wake configuration. The 48% decrease in Reynolds number decreased the net C_p by slightly less than 20%; the average net C_p at $M_\infty \doteq 3.0$, $Re/ft \doteq 1.10 \times 10^6$, for the four configurations is slightly less than 1.0. The 10% grid model at $X/D_B = 6$ has a slightly larger net C_p than the others, but there is not an appreciable difference between the configurations. The Schlieren photographs show that the wake was not blown, and except for the slight loss in picture quality due to the decrease in density, the flow is the same as $Re/ft \doteq 2.12 \times 10^6$.

3. $M_\infty \doteq 4.0$, $Re/ft \doteq 2.99 \times 10^6$

The 10% mesh models were tested at $X/D_B = 5$, 6, 7, 8, 9, and ∞; 10% grid models at $X/D_B = 6$, 7, 8, 9, and ∞. Internal, external, and net C_p's are shown in Tables XI and XII, Figs 34 and 36, and Schlieren photographs in Figs 35 and 37. The external C_p's at this condition are generally positive but very small, except for the high external pressure at the canopy edge. The 10% mesh model at $X/D_B = 5$ caused a blown wake; hence, the extremely small C_p values. The remaining pressure distributions at Mach 4.0 in the wake of the forebody are considerably unsymmetric, but the cause of the unsymmetry could not be located. Since the unsymmetry decreases with increasing stand-off distance and disappears in freestream, the forebody is most likely the cause; yet the forebody alignment and position were checked carefully and adjusted as accurately as possible, but the pressure data remained the same. A wake survey, which may have shown some unsymmetric distribution, was, unfortunately, not available. There is some difficulty in interpreting these results because of this unsymmetry. At first glance, it appears that an average of taps 4 to 9 may be close to an expected pressure. This approach gives an average net C_p of about 1.2 at the lower stand-off distances, which decreases to about 1.0 at $X/D_B = 9$, and is lower yet in freestream. This fairly strong decrease in C_p was not found at Mach 3.0, nor does the high value of 1.2 for the net C_p, the same as at Mach 3.0, agree with the decrease in drag coefficient found in Ref 2 with an increase of Mach number from 3.0 to 4.0. If the freestream values at Mach 4.0 are assumed correct, and the wake values are assumed to follow the same trends as at Mach 3.0, then the more correct pressures would be the low values. With this approach there would be little change in C_p with varying stand-off distance, and the magnitudes would agree with a decrease in drag coefficient from Mach 3.0 and Mach 4.0.

The flow photographs (Figs 35 and 37) show slight changes in the forebody shock waves due to the increase in Mach number, but other than the blown wake condition at $X/D_B = 5$, the canopy flow field is essentially the same as at Mach 3.0.

4. $M_\infty \doteq 4.0$, $Re/ft \doteq 1.36 \times 10^6$

For comparison, the 10% mesh and grid models with internal pressure taps were studied at $M_\infty \doteq 4.0$, $Re/ft \doteq 1.36 \times 10^6$. Table XIII, and Figs 38 and 40, show the internal C_p's and the Schlieren photographs are presented in Figs 39 and 41. At this decreased Reynolds number, the wake is blown at $X/D_B = 6$, as shown by the low internal C_p's and the flow photographs.

At larger stand-off distances the pressure distributions are again unsymmetric, but they show a decrease in internal C_p accompanied by the decrease in Reynolds number. Because of the unsymmetry, it is difficult to give the magnitude of the decrease, but it appears to be consistent with the Mach 3.0 results. With the exception of the $X/D_B = 6$ position, the Schlieren photographs show no changes in flow configuration, compared to those from the $M \doteq 4.0$, $Re/ft \doteq 2.99 \times 10^6$ recordings.

5. $M_\infty \doteq 4.0$, $Re/ft \doteq 0.86 \times 10^6$

For further comparison, Schlieren photographs of the 10% mesh and grid models at $X/D_B = 6$, 8, and ∞ are shown in Fig 42. Because of the very low static pressure, pressure distribution data could not be obtained at this condition; but the tests were made in order to see if the wake at $X/D_B = 7$ was converging or blown. Figure 43 shows that at $Re/ft \doteq 0.86 \times 10^6$ the wake is converging, and hence the flow configurations did not change. However, with a further Reynolds number decrease, to $Re/ft \doteq 0.56 \times 10^6$, the wake changed and assumed a blown characteristic.

C. The Blown Wake

A blown or diverging wake configuration was found at several conditions in this study. Several of these conditions have already been mentioned, but in the interest of completeness the findings may be repeated as follows. At a Mach number of 4.0, diverging or blown wakes occurred at $X/D_B = 5$, $Re/ft \doteq 2.99 \times 10^6$; $X/D_B = 6$, $Re/ft \doteq 1.36 \times 10^6$ and 0.86×10^6; and $X/D_B = 7$, $Re/ft \doteq 0.56 \times 10^6$. At a Mach number of 3.0, and using models with mesh roof only, a blown wake was found at $X/D_B = 5$ and $Re/ft \doteq 1.10 \times 10^6$. Schlieren photographs of the flow pattern with a maximum Reynolds number, at which a diverging wake was observed for a given Mach number and X/D_B position, are shown in Fig 44. The sharp decrease of the C_p value, found in this study for a steady but blown wake condition, agrees well with the decrease in drag coefficient reported in Ref 2 for flexible models in a blown wake.

D. Pressure Measurements in the Canopy Near-Wake

Total and static pressures were measured in the canopy near wake by means of the small pressure rake shown in Fig 5. The measured, total or static, pressure to freestream total pressure ratios are presented for the 5% models at $X/D_B = 6$, 7, 8, 9 and 11 in Fig 45, and for the 10% and 15% models at $X/D_B = 6$ and 8 in Fig 46. The static pressures in the wake were fairly uniform at P_ℓ / P_{o_∞} of 2×10^{-2}, and the total pressures increased markedly with increasing distance from canopy centerline. The pressure ratios shown indicate that in most cases the flow behind the canopy is supersonic, but an examination of the Schlieren photographs failed to show shock waves on the pressure probes. This is obviously a discrepancy. But a literature survey showed statements by several authors that the measured pressures in highly turbulent flow are mostly higher than the actually existing pressures. Thus the described pressure ratios are not reliable either. Therefore, there may not be supersonic flow in existence or the density may actually be so low that possible shock waves cannot be readily recorded. **Because the existence or non-existence of supersonic flow cannot be established, note that the "total" pressures presented in Figures 45 and 46 are the measured pitot tube pressures.**

V. SUMMARY

Pressure distribution measurements were made at Mach 3 and 4 at Reynolds numbers per foot from 1.10×10^6 to 2.99×10^6. Excluding the canopy edges the main contribution to the net pressure is provided by the positive internal pressure, since the magnitude of the external pressure amounts to 5%, or less, of the internal pressure. At the canopy edges the external pressure is positive and about equal to the internal pressure. This yields a very small net pressure difference, which was in some cases even negative. Schlieren photographs showed that in all cases the canopies had strong, detached bow shock waves which oscillated rapidly. This phenomenon is typical for parachute canopies with relatively low geometric porosity.

The effects of the porosity upon the pressure distribution when the parachute is located in the freestream or at different positions in the wake of a forebody were investigated at Mach and Reynolds numbers of $M_\infty \doteq 3.0$ and $Re/ft \doteq 2.12 \times 10^6$. In freestream an approximate average value of the net pressure coefficients, excluding the area of the canopy edge, amounts to $C_p = 1.2$, with a negative external pressure of $C_p = 0.06$. In the wake at six diameters behind the forebody, $X/D_B = 6$, the net pressure coefficient amounted to about $C_p = 1.2$, and decreased by approximately 10% as the rearward location increased to $X/D_B = 11$. Neither the type of porous roof material, mesh or grid, nor the geometric porosity of the model, 5%, 10%, or 15%, had a significant effect on these averages.

In order to study Mach number effects, experiments were made at Mach numbers of $M_\infty \doteq 3.0$ and $M_\infty \doteq 4.0$ with Reynolds numbers per foot of 2.12×10^6 and 2.99×10^6, respectively, in freestream and in the wake of a forebody. In freestream it was observed that the distribution of internal pressure at Mach numbers 3 and 4 was about the same. However, the external pressure at Mach number 3 was negative whereas it was positive at Mach number 4, and the average net pressure coefficients resulting from the Mach number 4-tests amount to approximately 0.8, whereas those of the Mach number 3-tests were in the order of 1.2. General conclusions concerning the Mach number effects of the parachute when located in the wake cannot be extracted from the conducted tests because the freestream Mach number cannot be considered a valid characteristic for the wake conditions, and the presence of the forebody has caused unsymmetrical pressure distribution which so far has not been explained. Detailed observations are presented in Section IV.

A certain Reynolds number effect upon the pressure distribution of the parachute canopy can be extracted from the experiments at Mach number 3 and Reynolds numbers per foot of 1.10×10^6 and 2.12×10^6 under wake conditions, and at Mach number 4 with Reynolds numbers per foot of 1.36×10^6 and 2.99×10^6 under freestream conditions. In detail it was found that in the Mach number 3-tests the average internal pressure coefficient increased from 1.0 to 1.14 with increasing Reynolds number. In the Mach 4-tests the internal pressure coefficient increased from 0.6 to 0.8 with the respective Reynolds number increase. In all of these experiments the external pressure was negligibly small compared to the internal pressure.

A blown or diverging wake configuration was found at several flow conditions. This was associated with a very low net pressure coefficient and a relatively stable flow field around the canopy.

Pressures in the canopy near wake were measured for several stand-off distances at $M_\infty \doteq 3.0$, Re/ft $\doteq 2.12 \times 10^6$. The pressure measurements indicated supersonic flow but the probes of the pressure rake failed to show shock waves. Therefore, these results must be considered with caution because of the limitations of pressure recordings with standard pressure probes in turbulent supersonic flow.

VI. REFERENCES

1. Performance of and Design Criteria for Deployable Aerodynamic Decelerators, WADC Technical Report, ASD-TR-61-579, December 1963.

2. L. W. Sims: The Effects of Design Parameters and Local Flow Fields on the Performance of Hyperflo Supersonic Parachutes and High Dynamic Pressure Parachute Concepts, AFFDL-TR-65-150, Vol. I, October 1965.

3. R. A. Pinker and M. V. Herbert: The Pressure Loss Associated with Compressible Flow Through Square-Mesh Wire Gauges, AD-489654, National Gas Turbine Est. Report No. R. 281, 1966.

4. The American Society of Mechanical Engineers: Supplement to ASME Power Test Codes, Chapter 4, "Flow Measurement Instruments and Apparatus," PTC 19.5;4-1959.

5. Equations, Tables and Charts for Compressible Flow, NACA Report 1135, 1953.

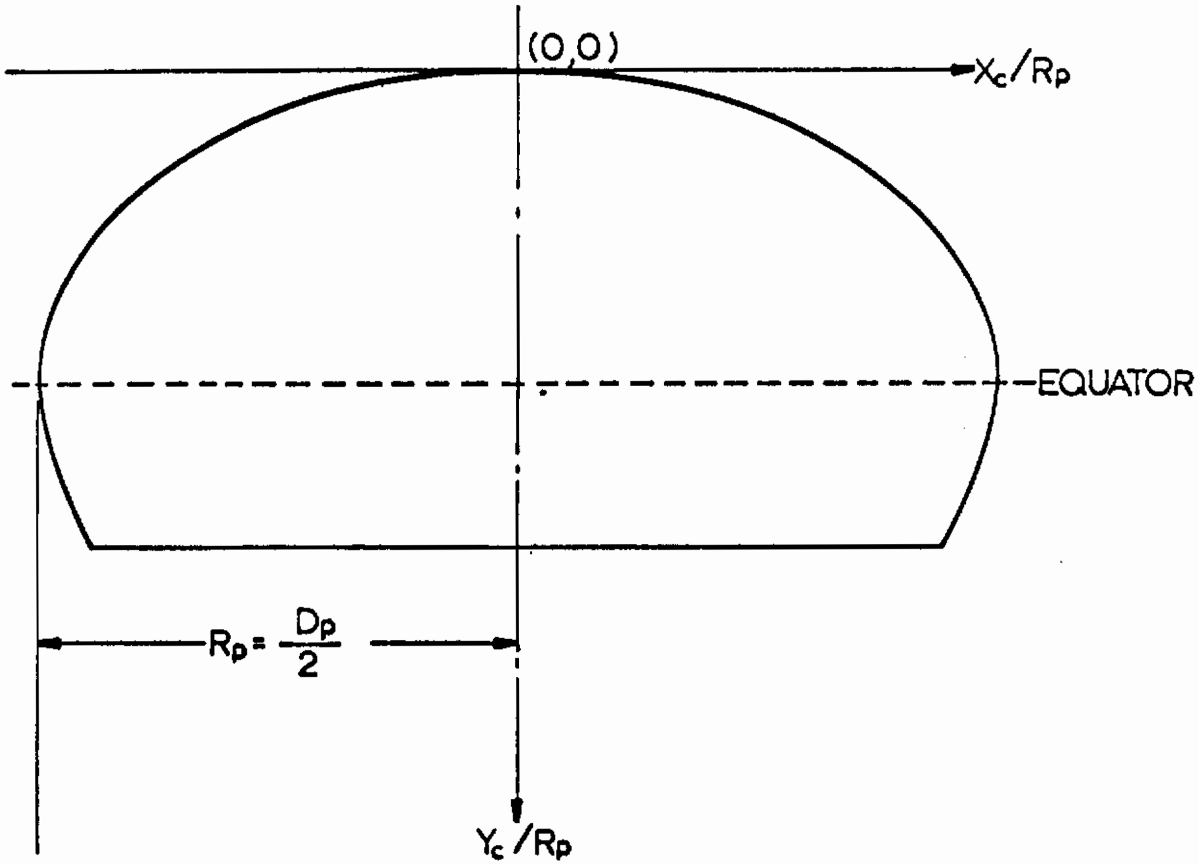

Fig 1. Established Profile of Hyperflo Parachute

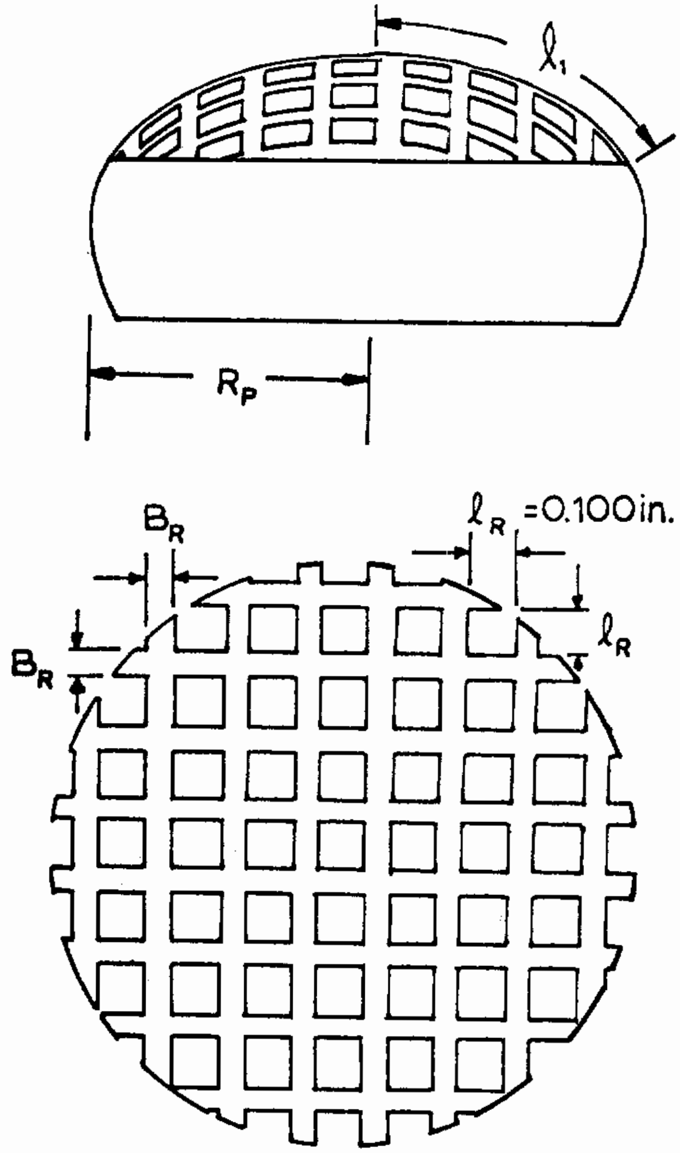

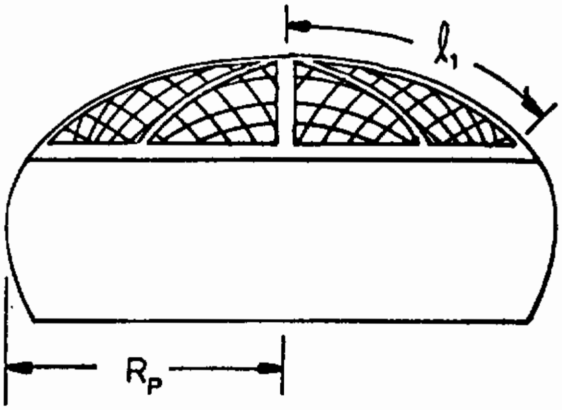

NOTE: THERE ARE EIGHT SYMMETRICALLY PLACED RIBBONS, 0.100 in. WIDE, BETWEEN MESH GORES.

a) MESH-ROOFED MODEL

APPROX. GEOMETRIC POROSITY	ℓ_1/R_P	$(K\lambda)_m$
15 %	0.980	0.464
10 %	0.803	0.464
5 %	0.572	0.464

b) GRID-ROOFED MODEL

APPROX. GEOMETRIC POROSITY	B_R/ℓ_R	ℓ_1/R_P	COMPUTED GEOMETRIC POROSITY
15 %	0.56	0.980	16.8 %
10 %	0.91	0.980	10.9 %
5 %	1.69	0.980	5.05 %

Fig 2. Porous Region Parameters for Mesh-roofed and Grid-roofed Hyperflo Models

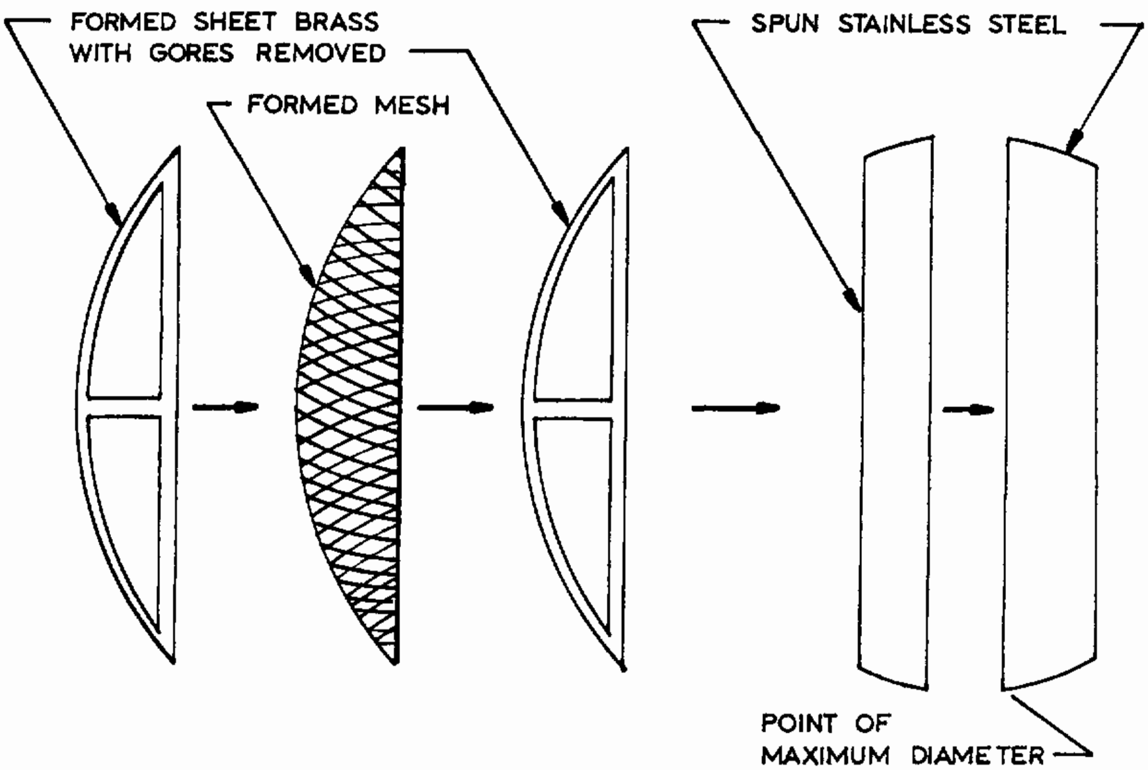

a. MESH-ROOFED MODEL

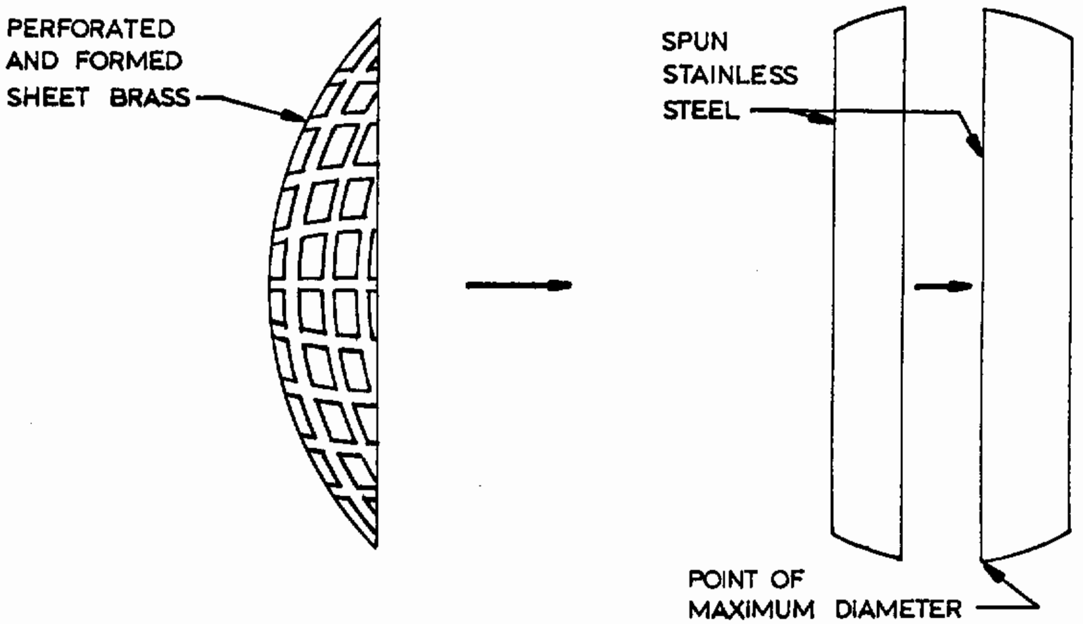

b. GRID-ROOFED MODEL

Fig 3. Exploded Views of the Hyperflo Models

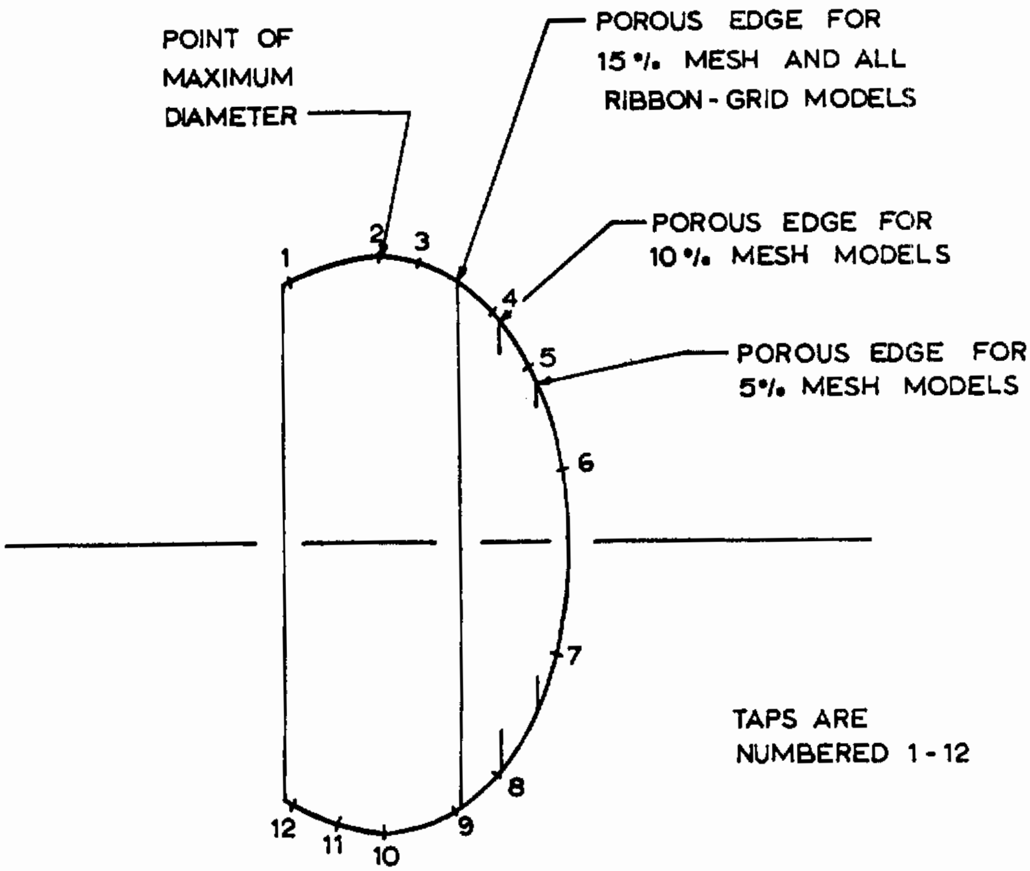

DUPLICATE TAPS
1 & 12
2 & 10
4 & 8

Fig 4. Nominal Tap Location for all Tapped Hyperflo Models

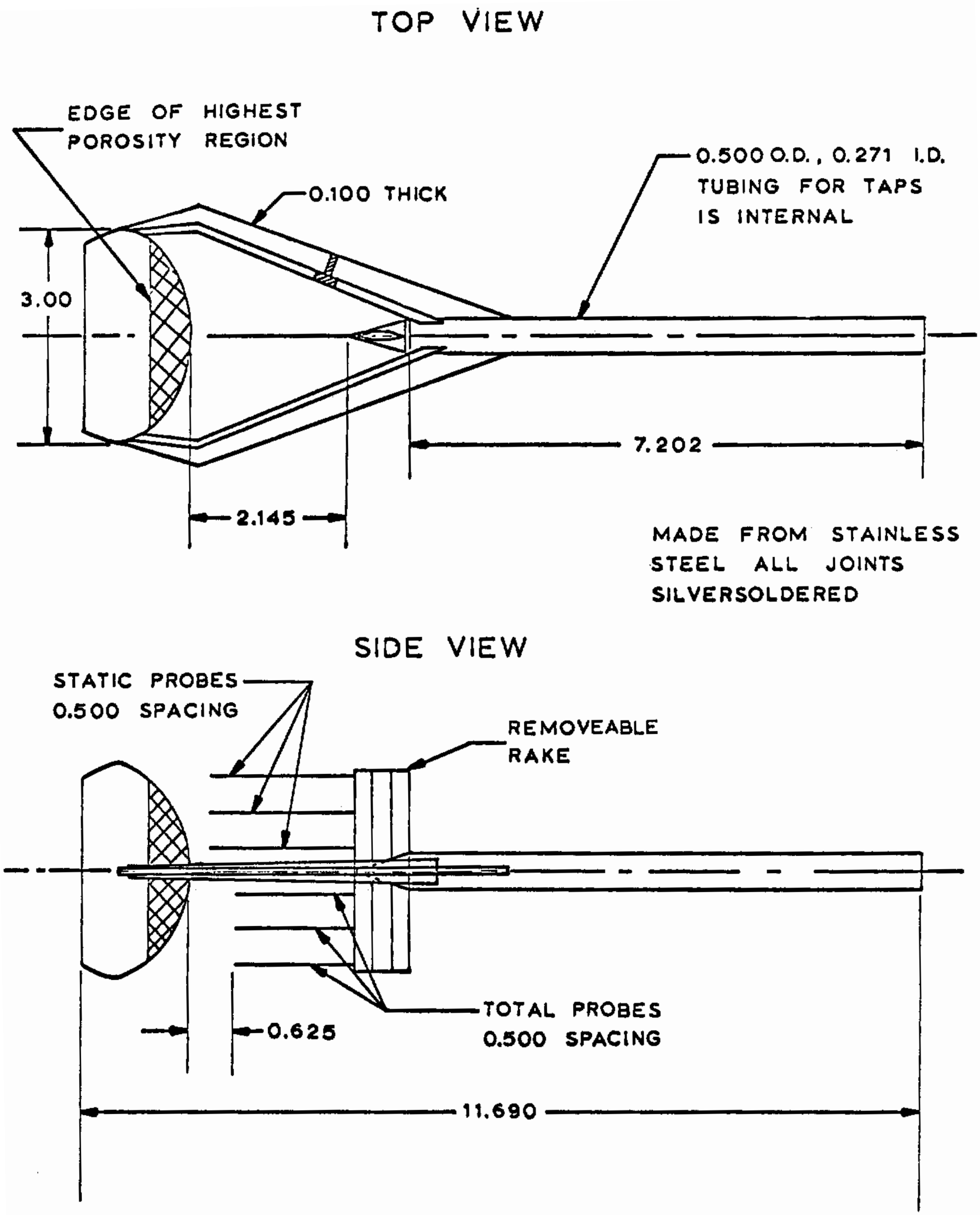

Fig 5. Sting for Internal Flow Pressure Measurements ($\frac{1}{2}$ Scale)

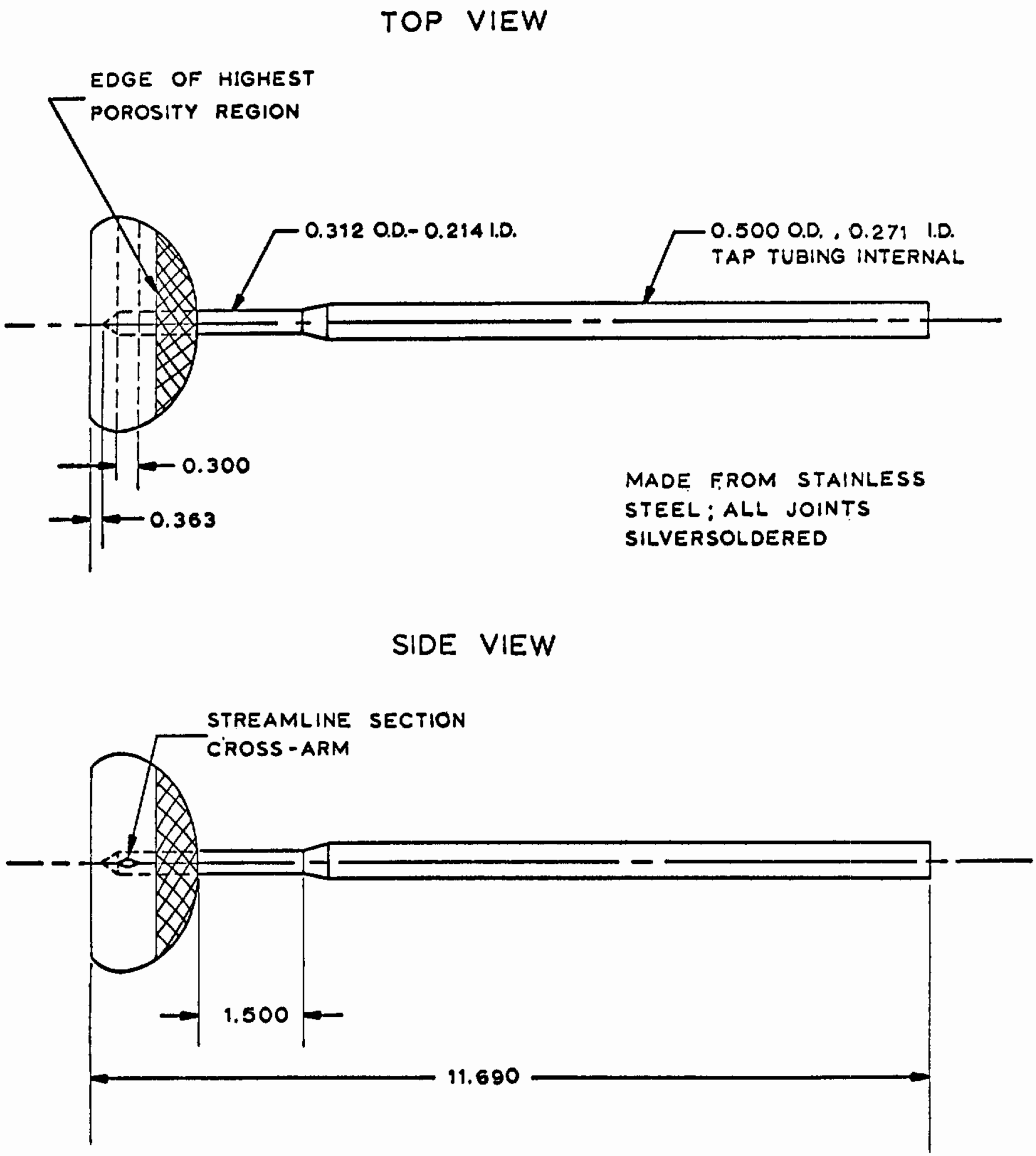

Fig 6 . Sting for External Flow Measurements (½ Scale)

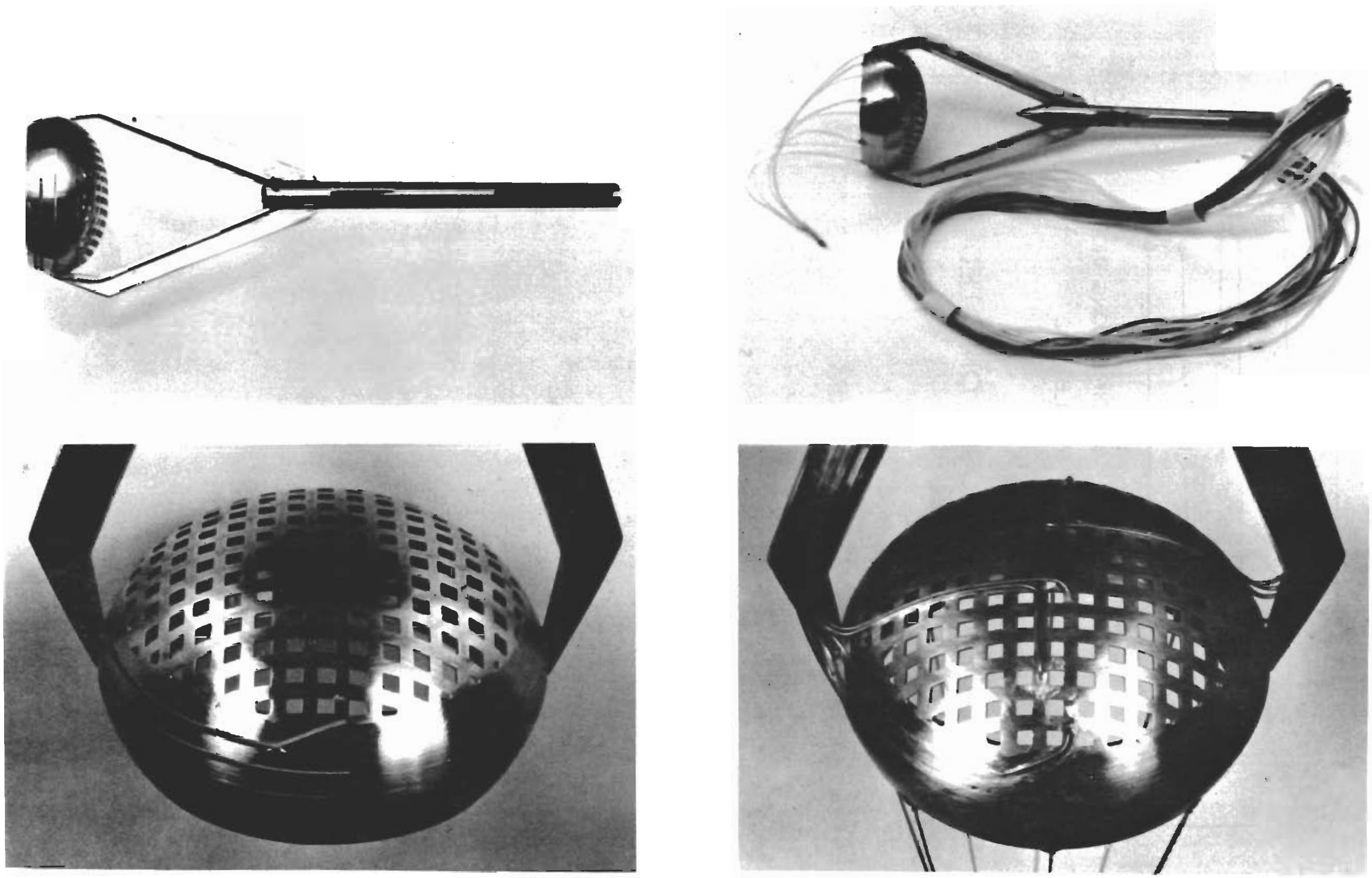

Fig 7 Method of Recessing Pressure Tap Tubes into Canopy Surface.

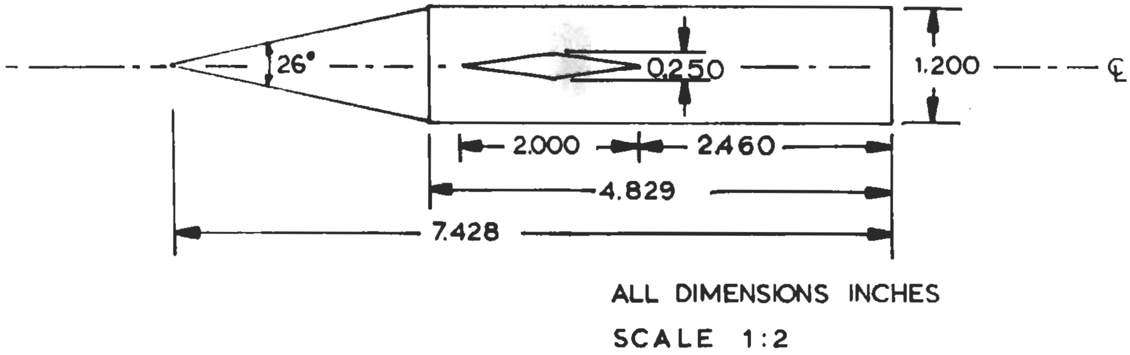

a. SIDE VIEW (WING-TIP MOUNT OMITTED FOR CLARITY)

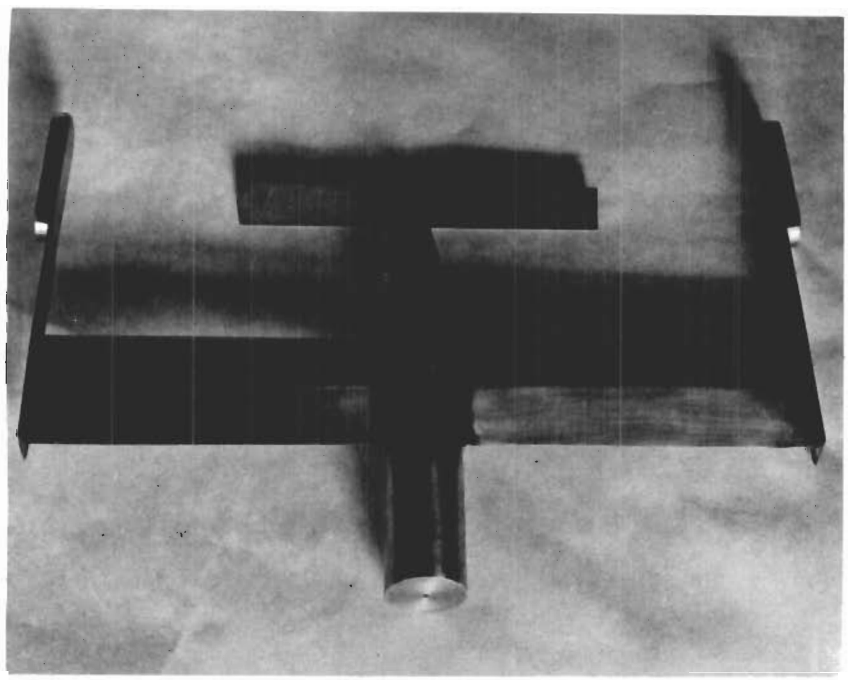

b. TOP VIEW

Fig 8. Side and Top Views of Forebody

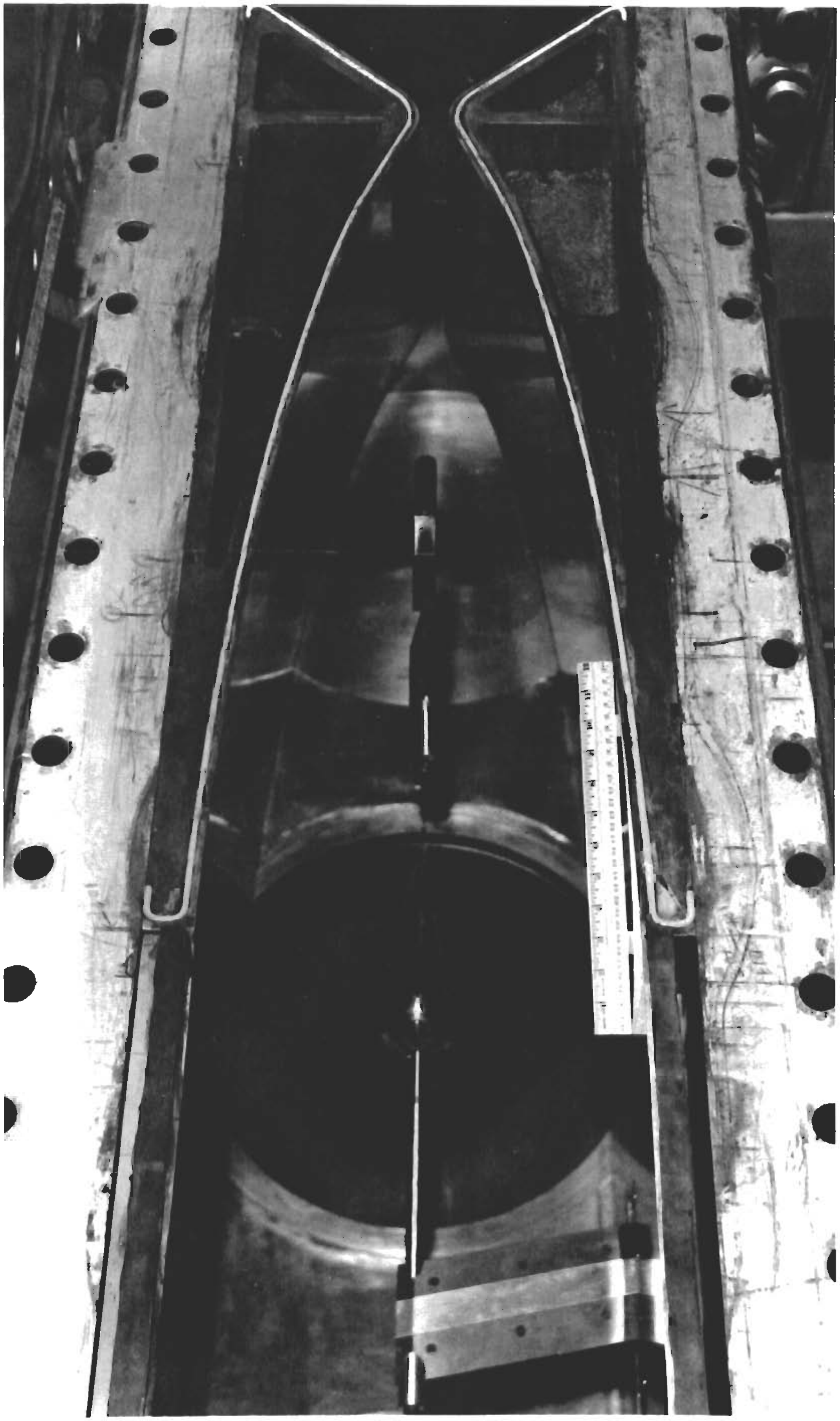

Fig 9 Model Installed in the Wind Tunnel

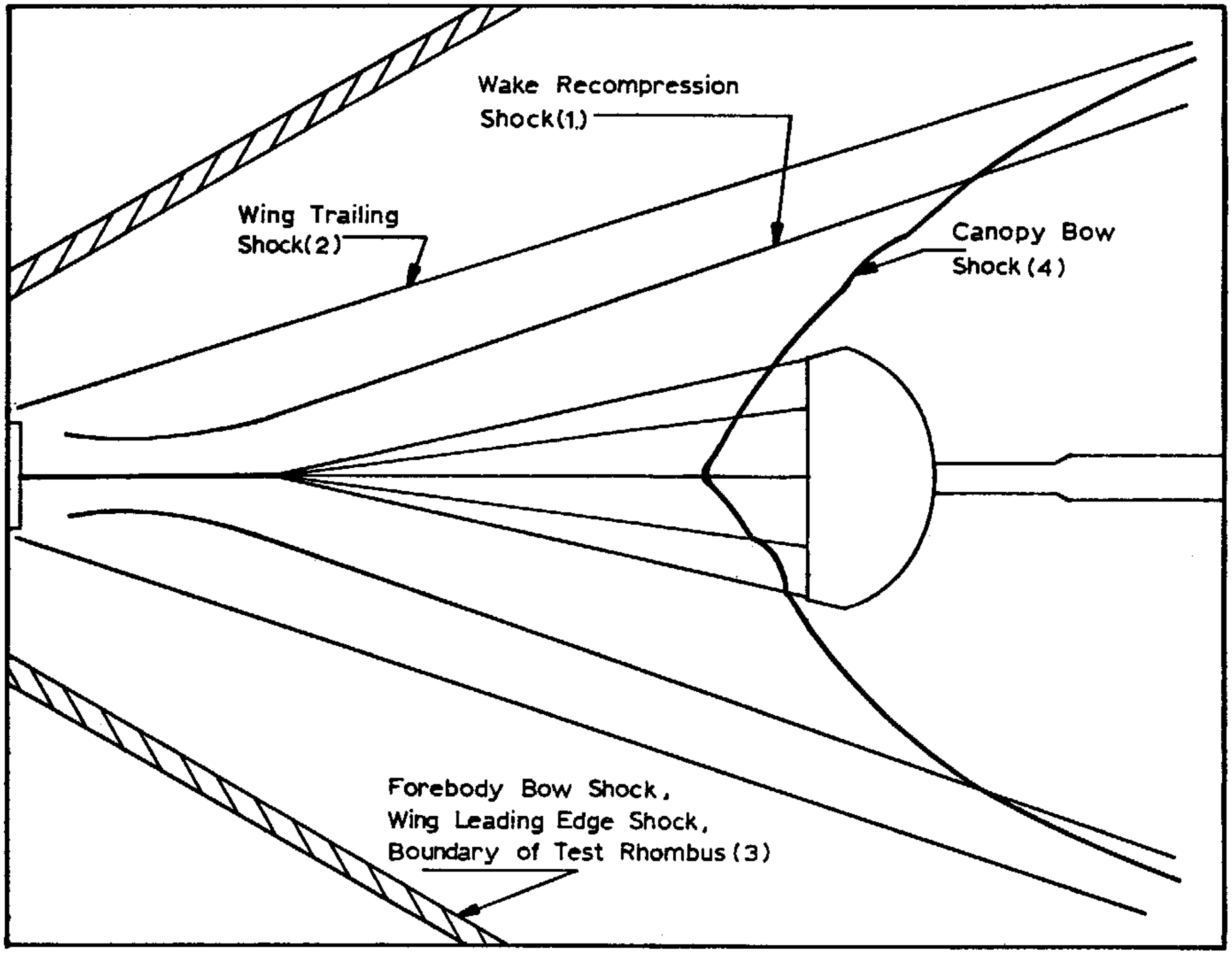

Fig 10. Schematic of a Hyperflo Model in the Forebody Wake

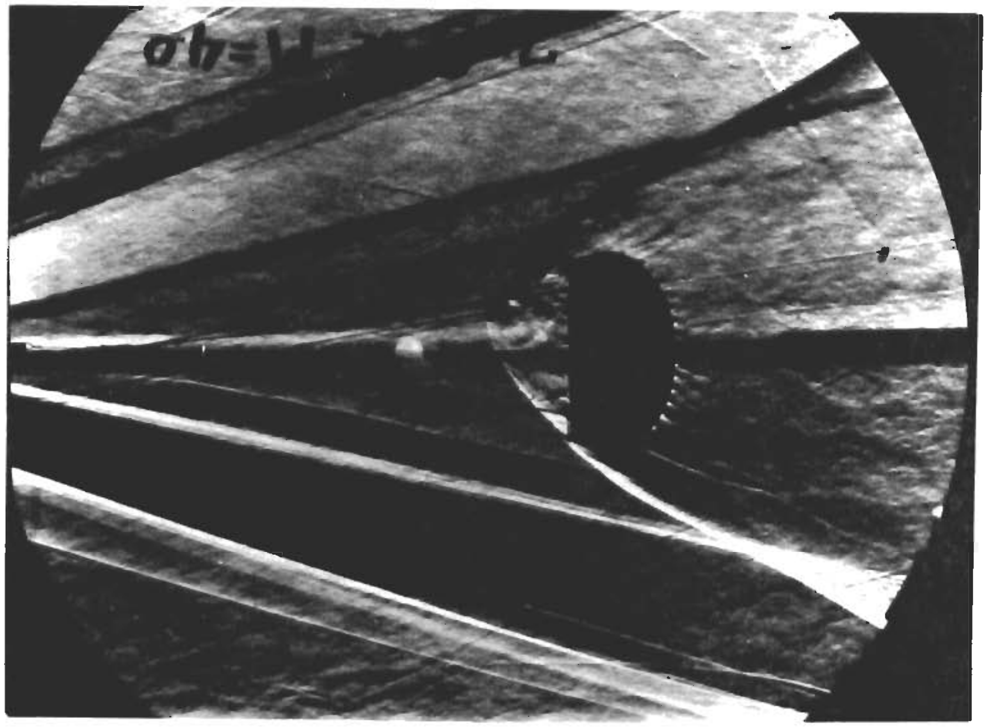

a. NORMAL WAKE 10% GRID MODEL, Re/ft = 2.99 x 10^6

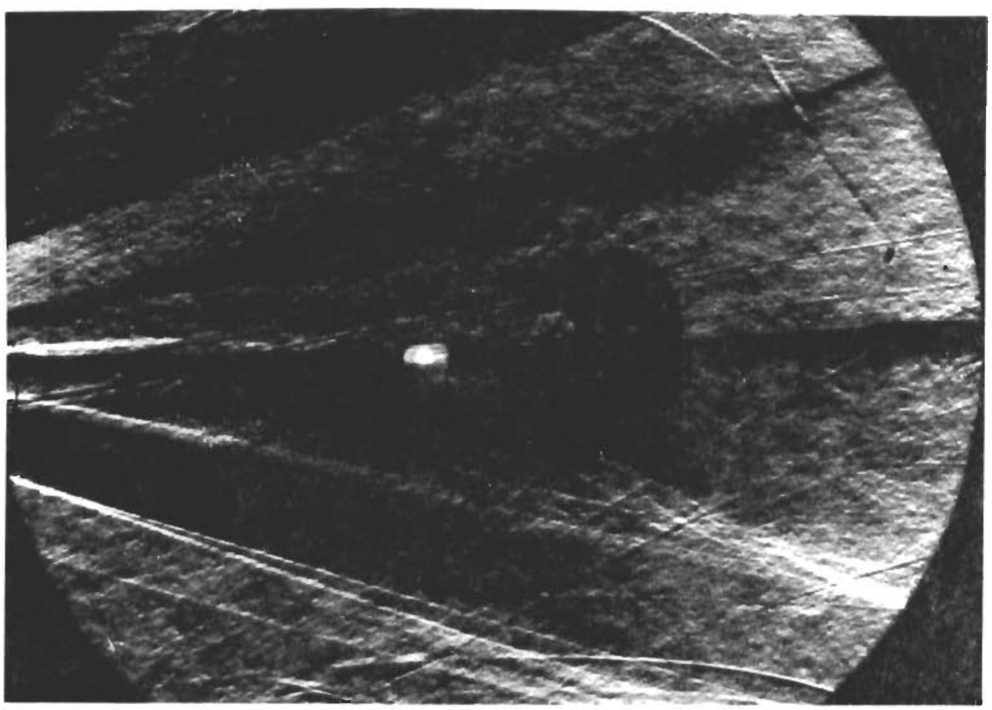

b. BLOWN WAKE 10% GRID MODEL, Re/ft = 0.56 x 10^6

Fig 11. Comparison of Normal and Blown Wakes ($M_\infty \doteq 4.0$, $X/D_B = 7$)

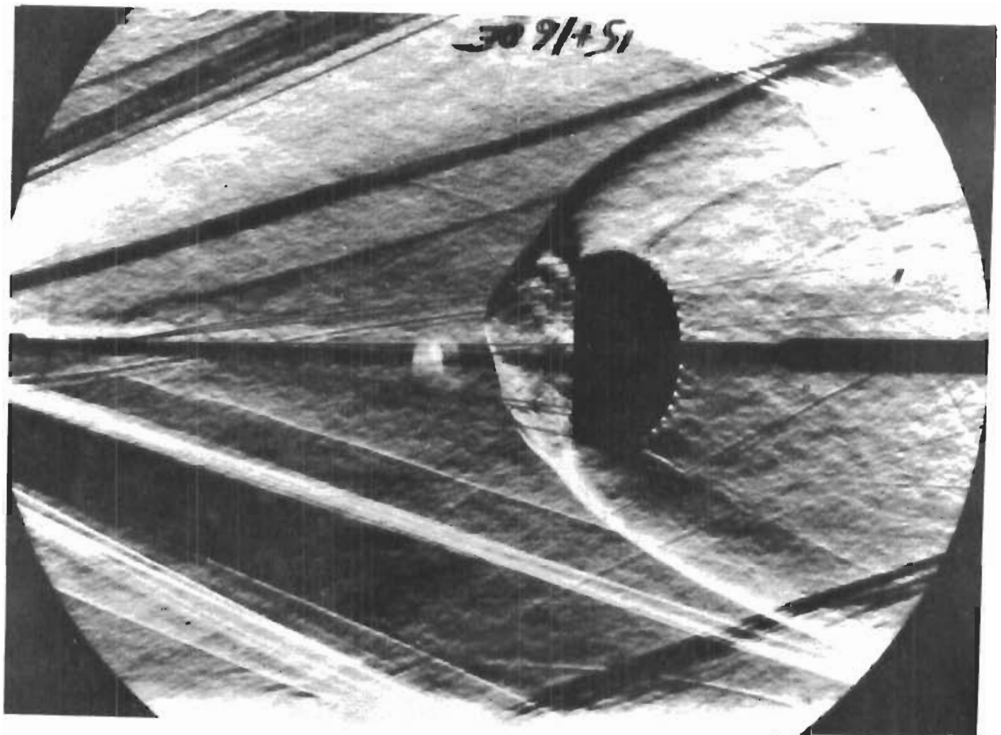

a. 10 % GRID MODEL, $M_\infty = 3.0$, Re/ft = 2.12×10^6

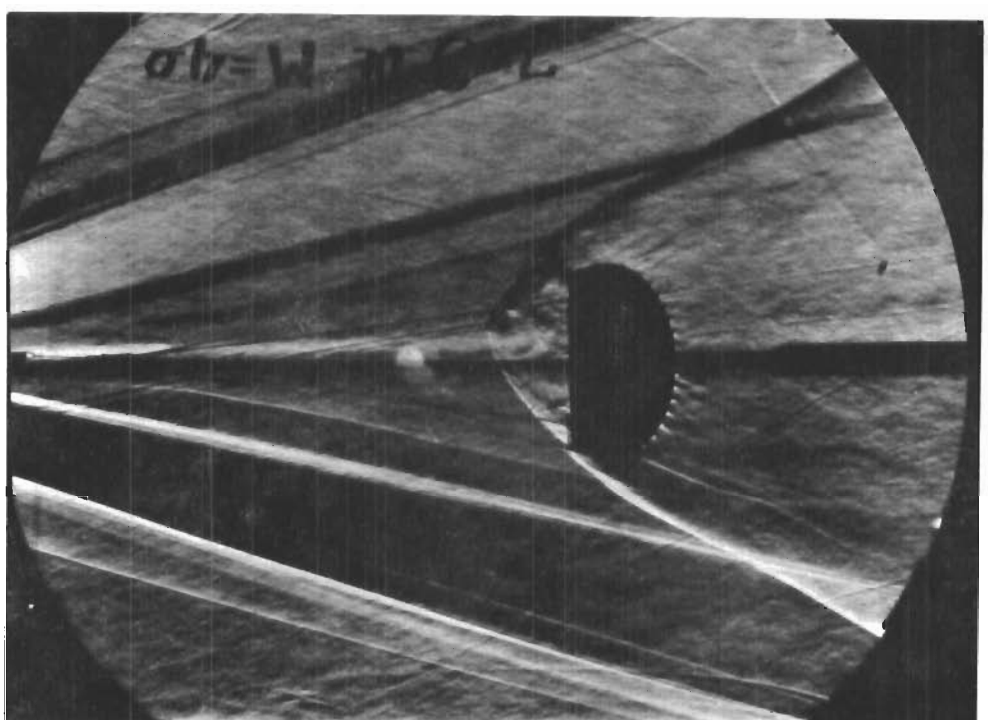

b 10 % GRID MODEL, $M_\infty = 4.0$, Re/ft = 2.99×10^6

Fig 12. Comparison of Mach 3 and Mach 4 ($X/D_B = 7$)

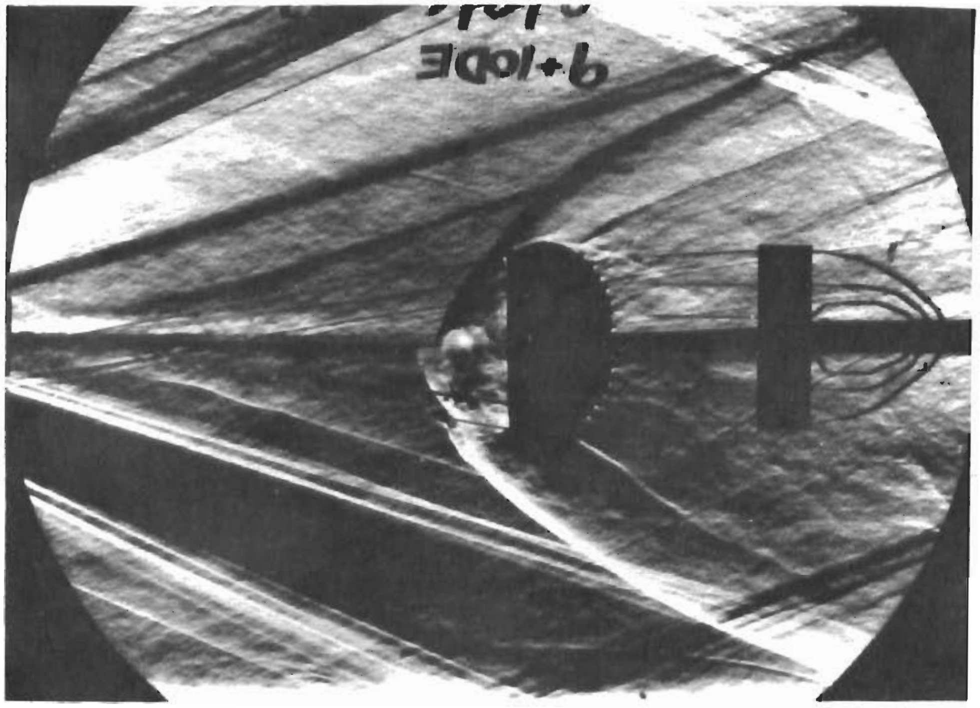

a. 10% GRID MODEL, $Re/ft = 2.12 \times 10^6$

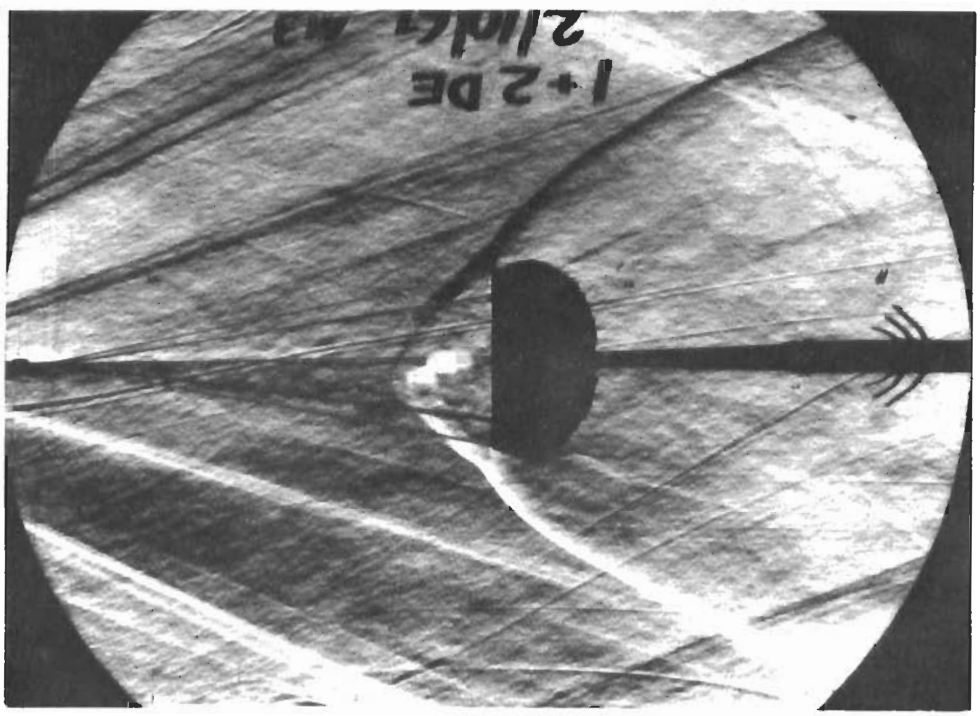

b. 10% GRID MODEL, $Re/ft = 1.10 \times 10^6$

Fig 13. Comparison of Reynolds Numbers ($M_\infty \doteq 3.0$, $X/D_B = 6$)

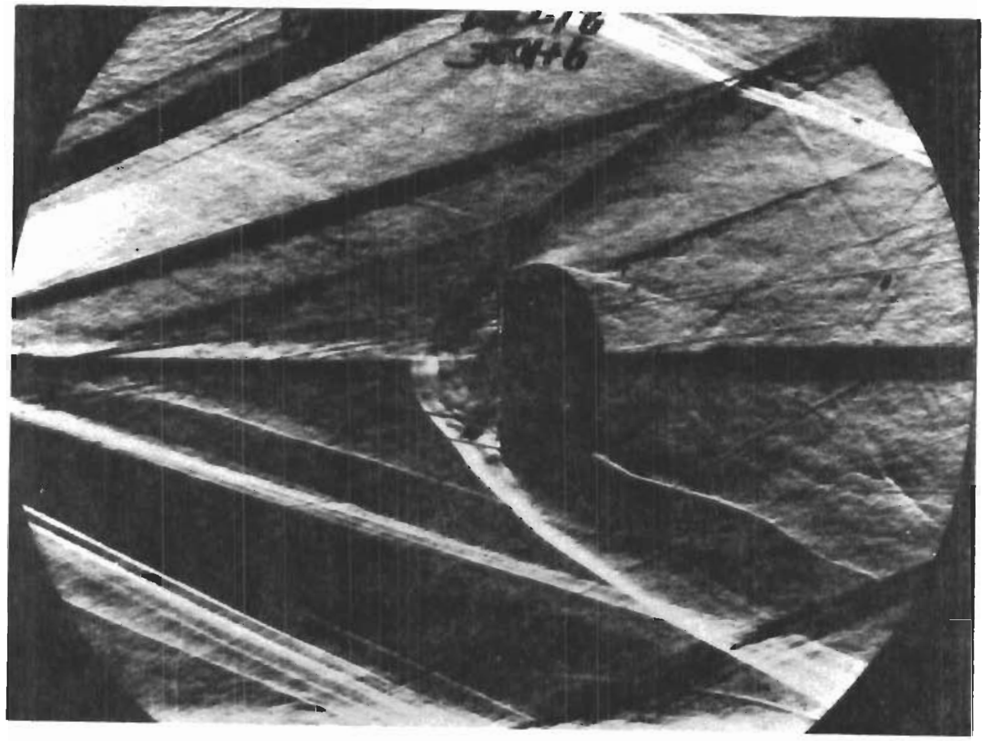

a. 10 % MESH MODEL

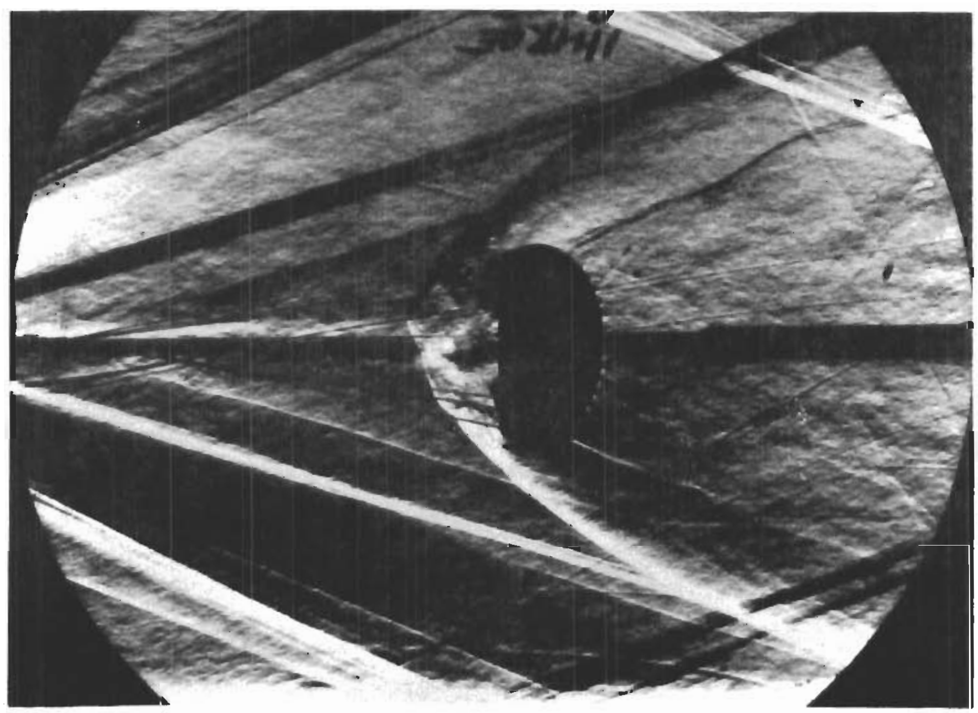

b. 10% GRID MODEL

Fig 14. Comparison of Mesh and Grid Models
($M_\infty \doteq 3.0$, $Re/ft \doteq 2.12 \times 10^6$, $X/D_B = 6$)

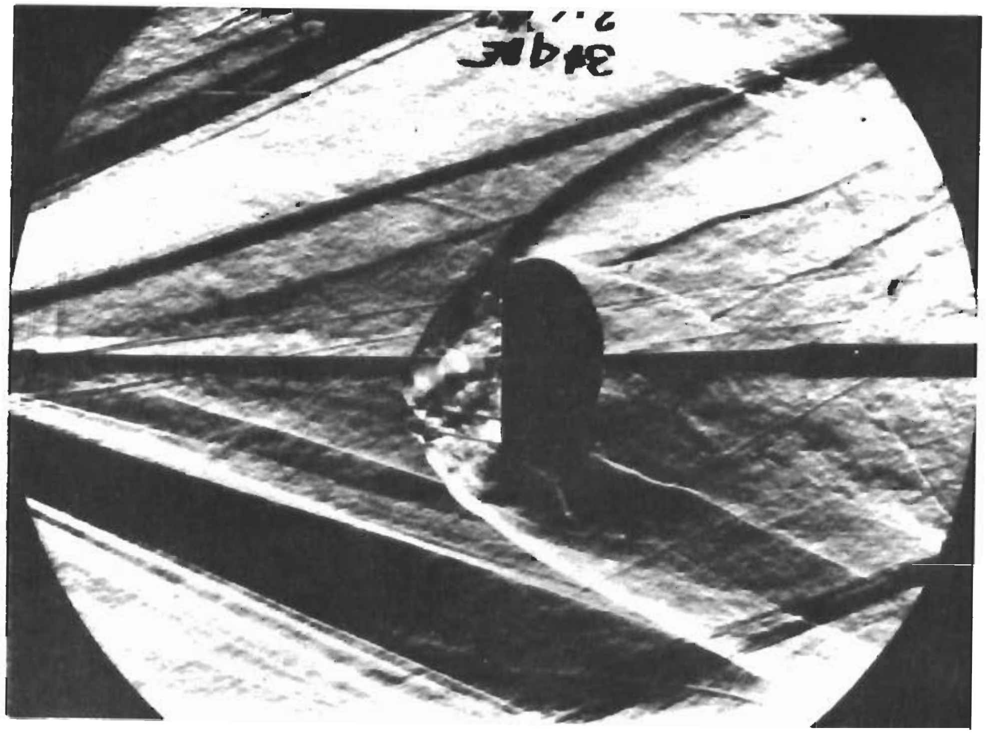

a. 10% MESH MODEL WITHOUT PRESSURE TAPS

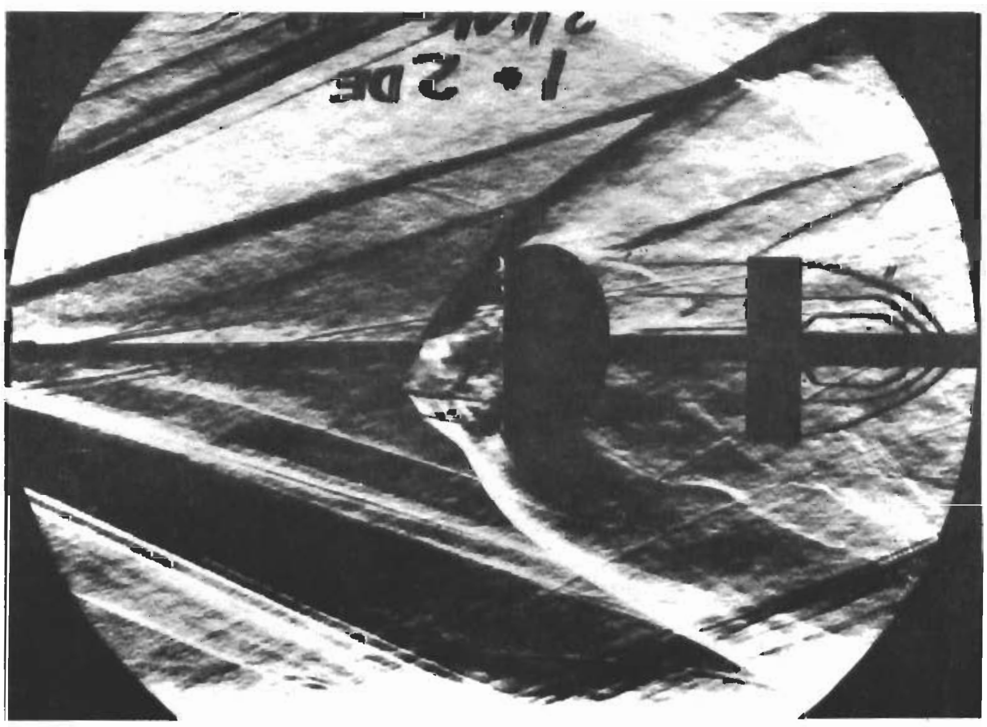

b. 10% MESH MODEL WITH PRESSURE TAPS

Fig 15. Comparison of Models With and Without Pressure Taps ($M_{\infty} \doteq 3.0$ $Re/ft \doteq 2.12 \times 10^6$, $X/D_B = 6$)

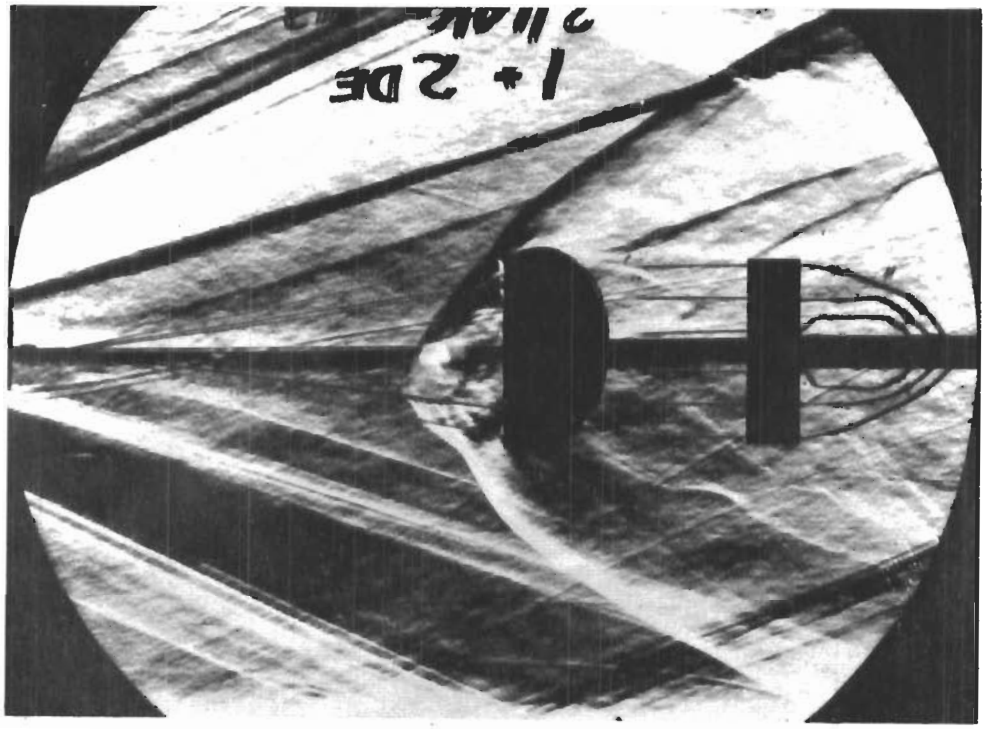

a. 10 % MESH MODEL WITH INTERNAL PRESSURE TAPS

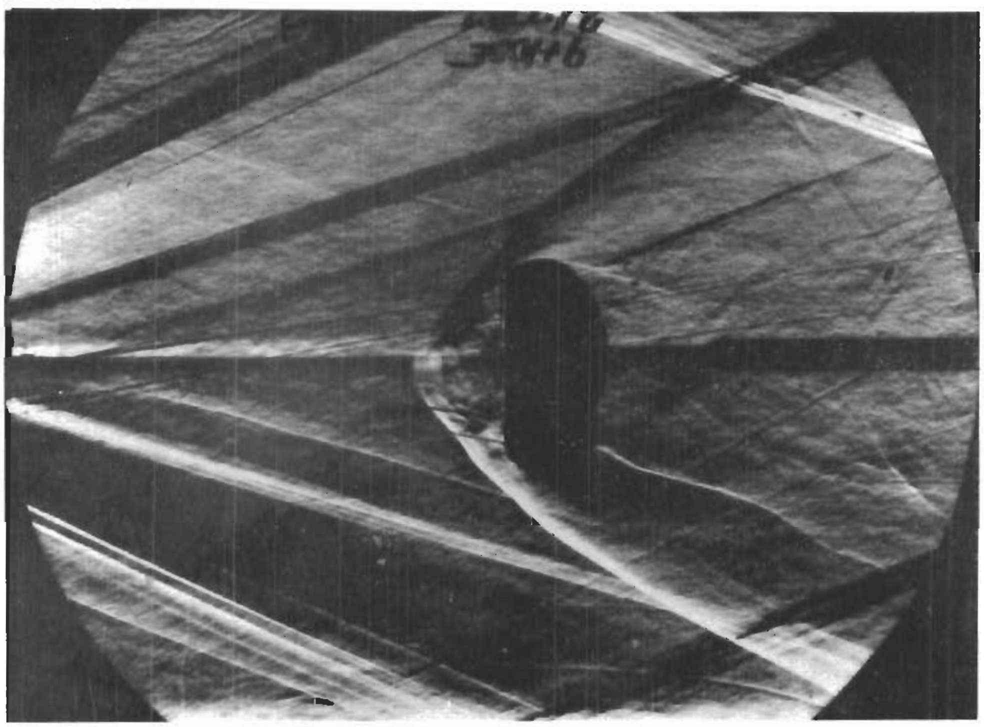

b. 10 % MESH MODEL WITH EXTERNAL PRESSURE TAPS

Fig 16. Comparison of Internal and External Pressure Tap Models ($M_\infty \doteq 3.0$, $Re/ft \doteq 2.12 \times 10^6$, $X/D_B = 6$)

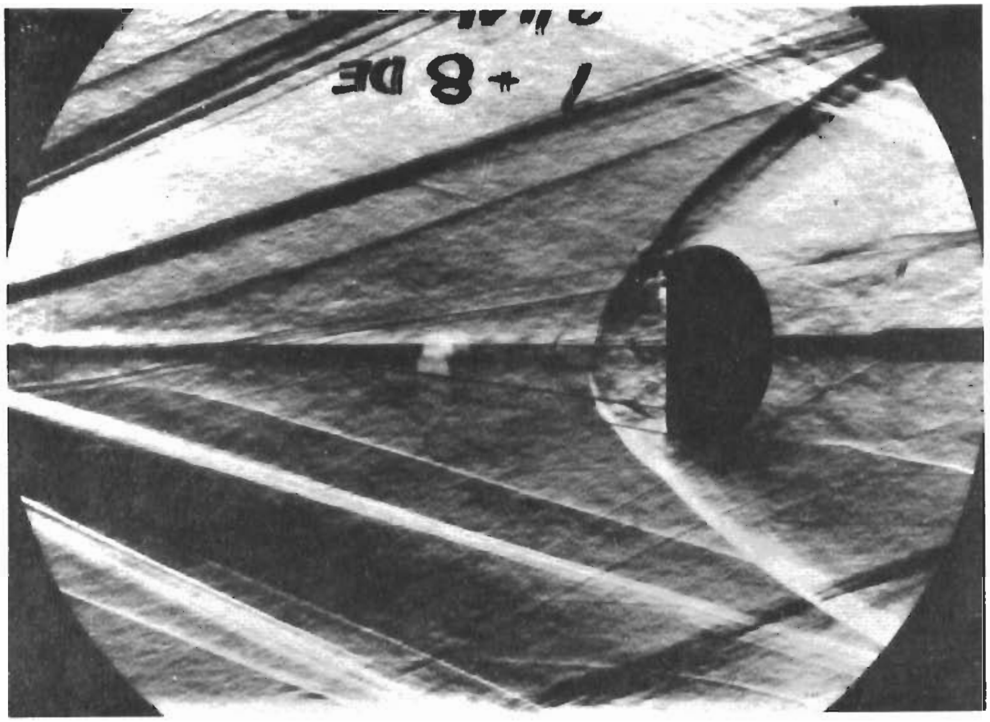

a 5% MESH MODEL

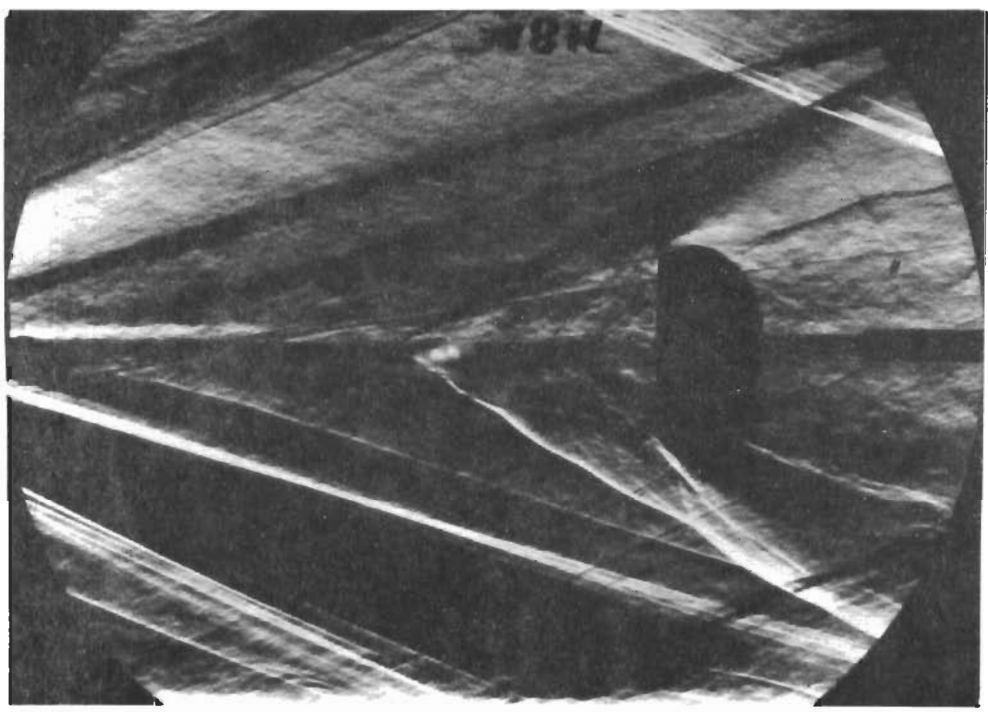

b 15% MESH MODEL

Fig 17. Comparison of 5% and 15% Models
($M_\infty \doteq 3.0$, $Re/ft \doteq 2.12 \times 10^6$, $X/D_B = 8$

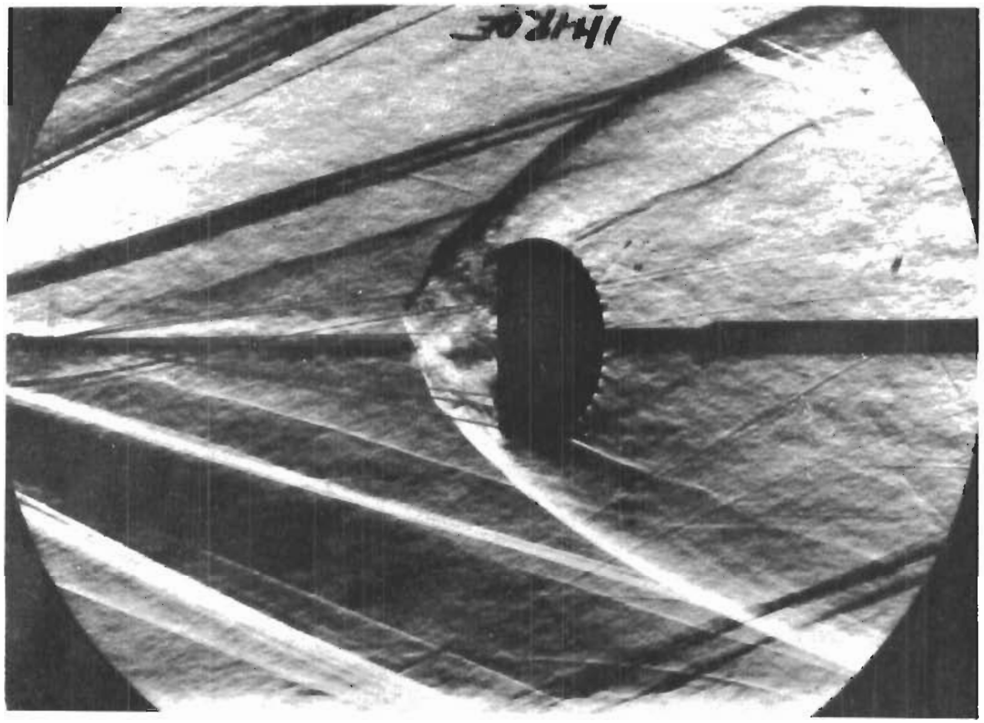

a. 10 °/o GRID MODEL, $X/D_B = 6$

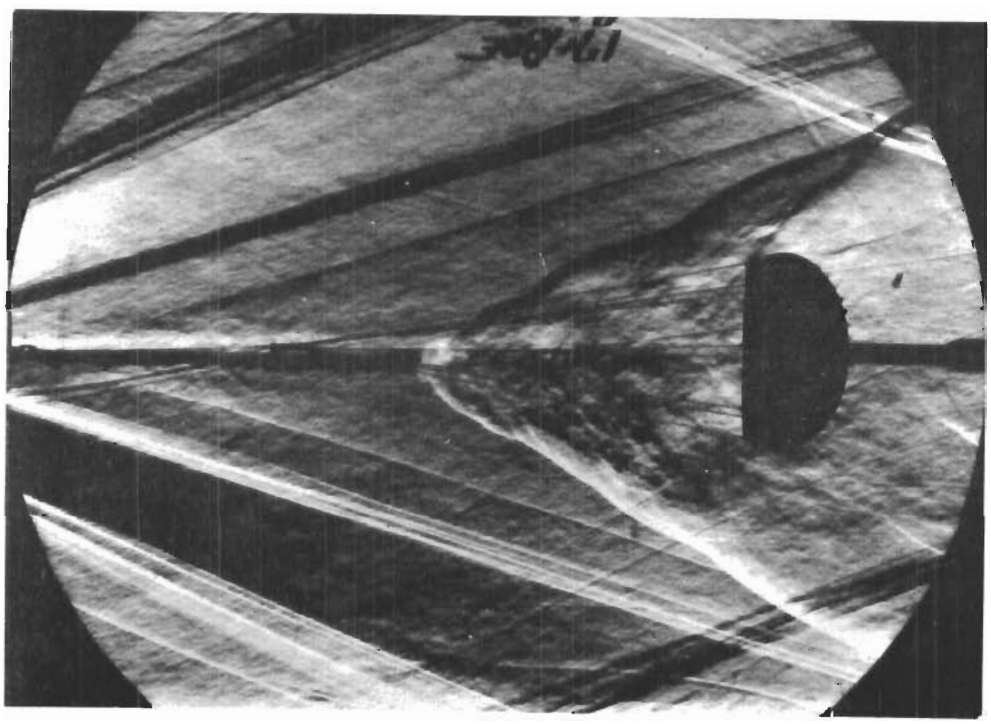

b. 10 °/o GRID MODEL, $X/D_B = 9$

Fig 18. Comparison of $X/D_B = 6$ and $X/D_B = 9$
($M_\infty \doteq 3.0$, $Re/ft \doteq 2.12 \times 10^6$)

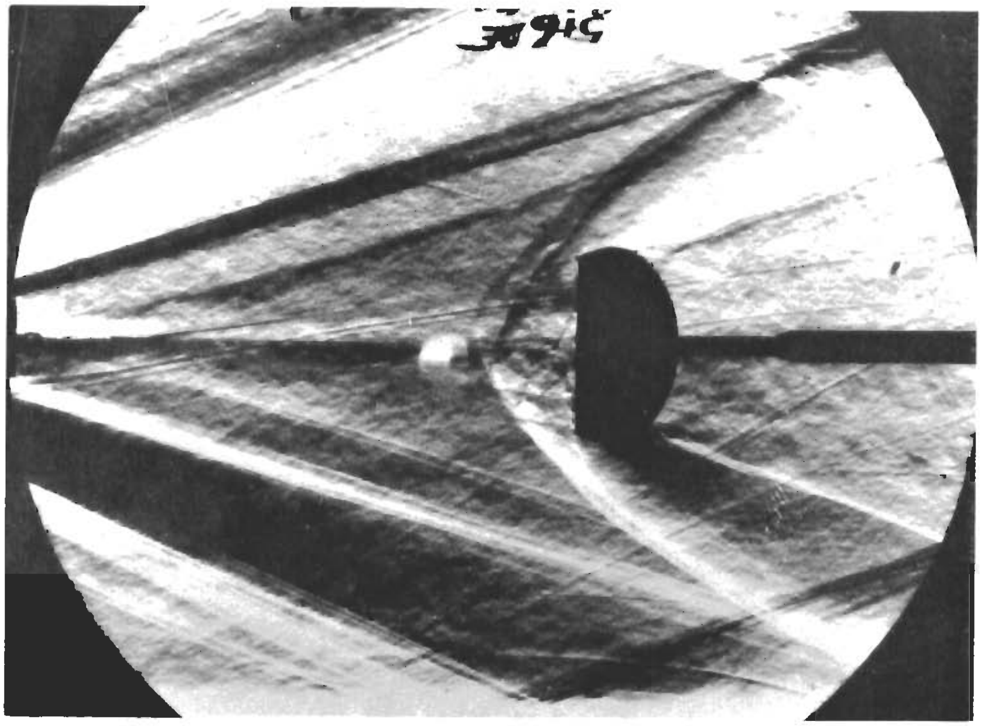

a. 10 °/o MESH MODEL, $X/D_B = 7$

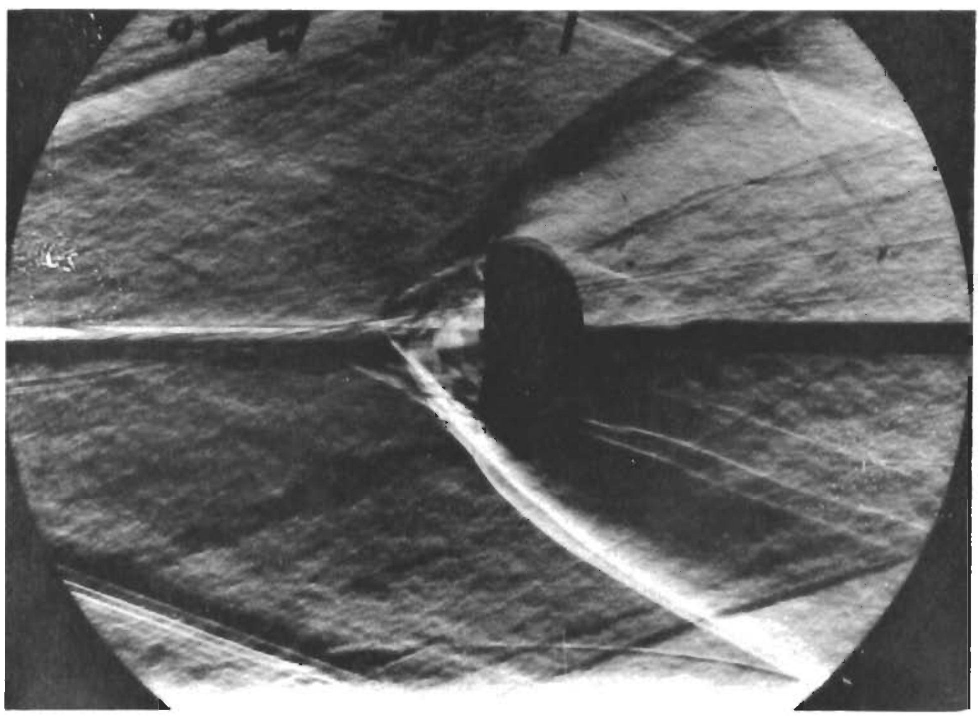

b. 10 °/o MESH MODEL, $X/D_B = \infty$

Fig 19. Comparison of Wake and Freestream Flow, Double Exposure Schlieren Photographs ($M_\infty \doteq 3.0$, $Re/ft \doteq 2.12 \times 10^6$)

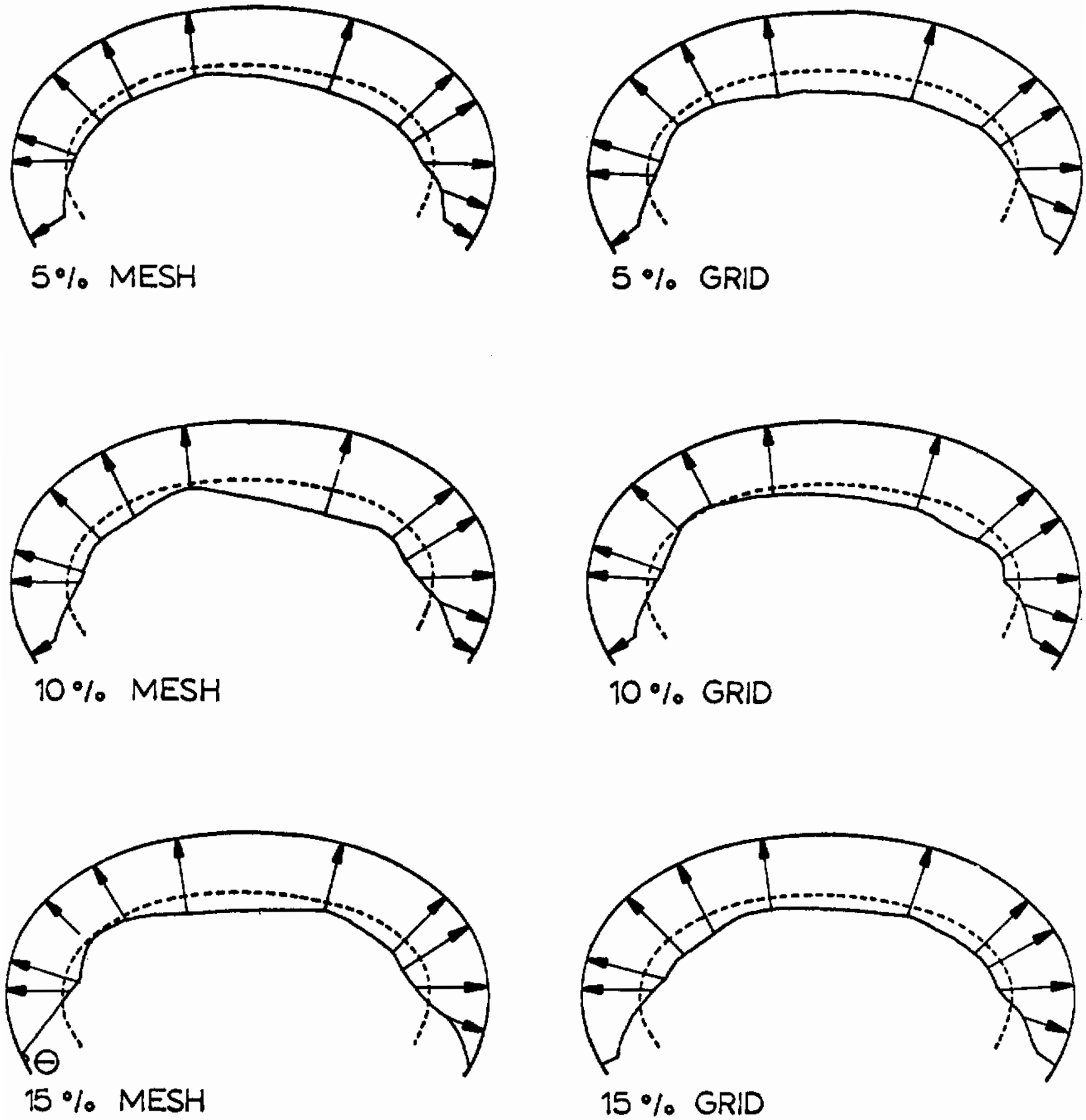

NOTES: DASHED LINE SHOWS MAGNITUDE OF UNIT C_p VECTOR

TAP 1 ON LOWER LEFT OF CANOPY

Fig 20. Schematic of Net Pressure Coefficient at $X/D_B = 6$ ($M_\infty \doteq 3.0$, Re/ft $\doteq 2.12 \times 10^6$)

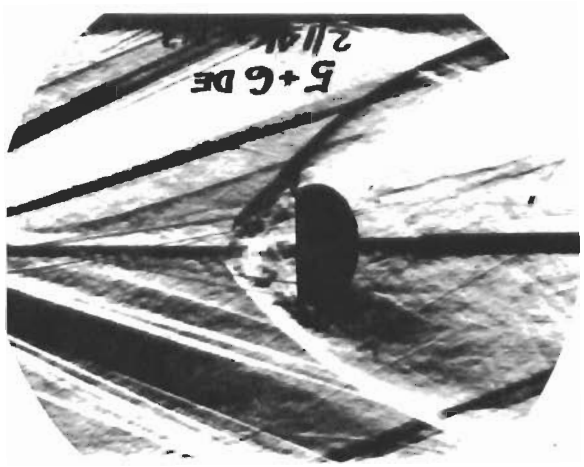

a. 5% MESH

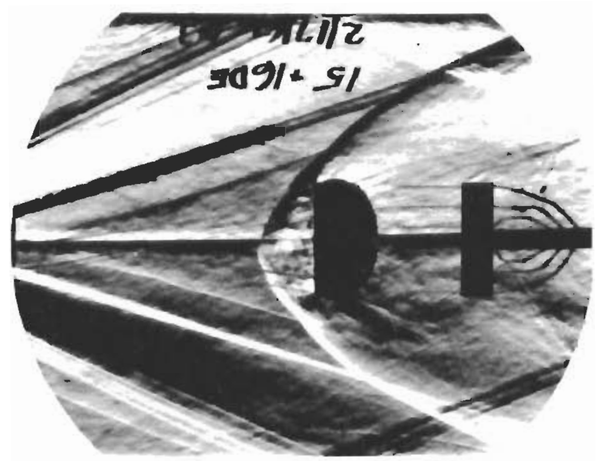

b. 5% GRID

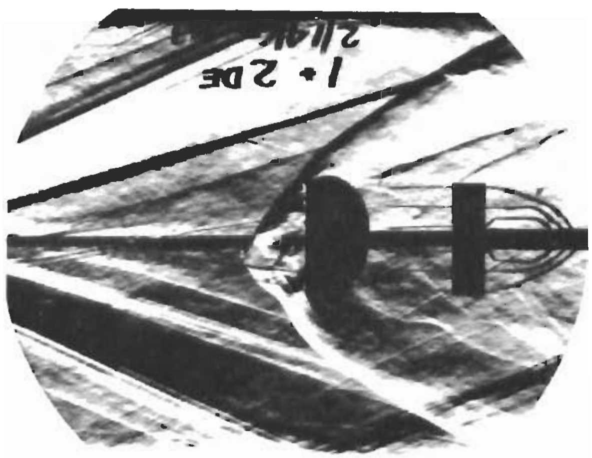

c. 10% MESH

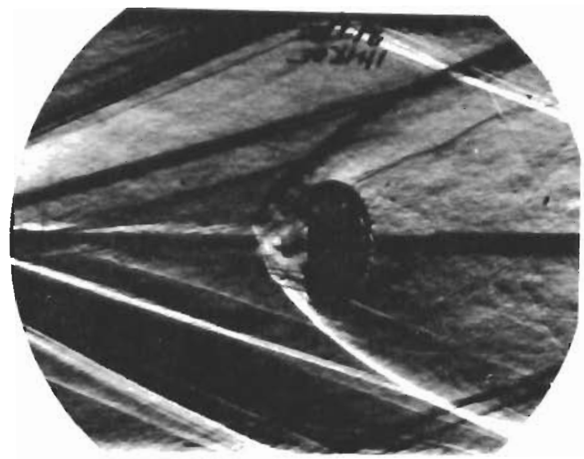

d. 10% GRID

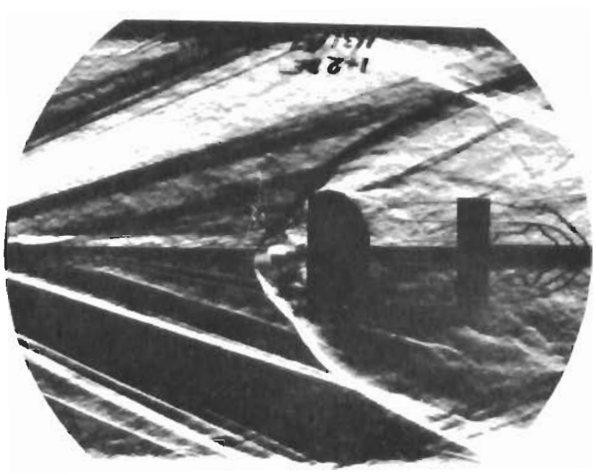

e. 15% MESH

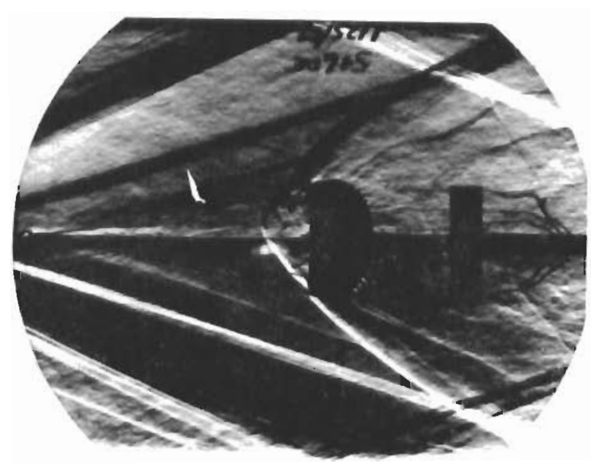

f. 15% GRID

Fig **21** Schlieren Photographs at $X/D_B = 6$
($M_\infty \doteq 3.0$, $Re/ft \doteq 2.12 \times 10^6$)

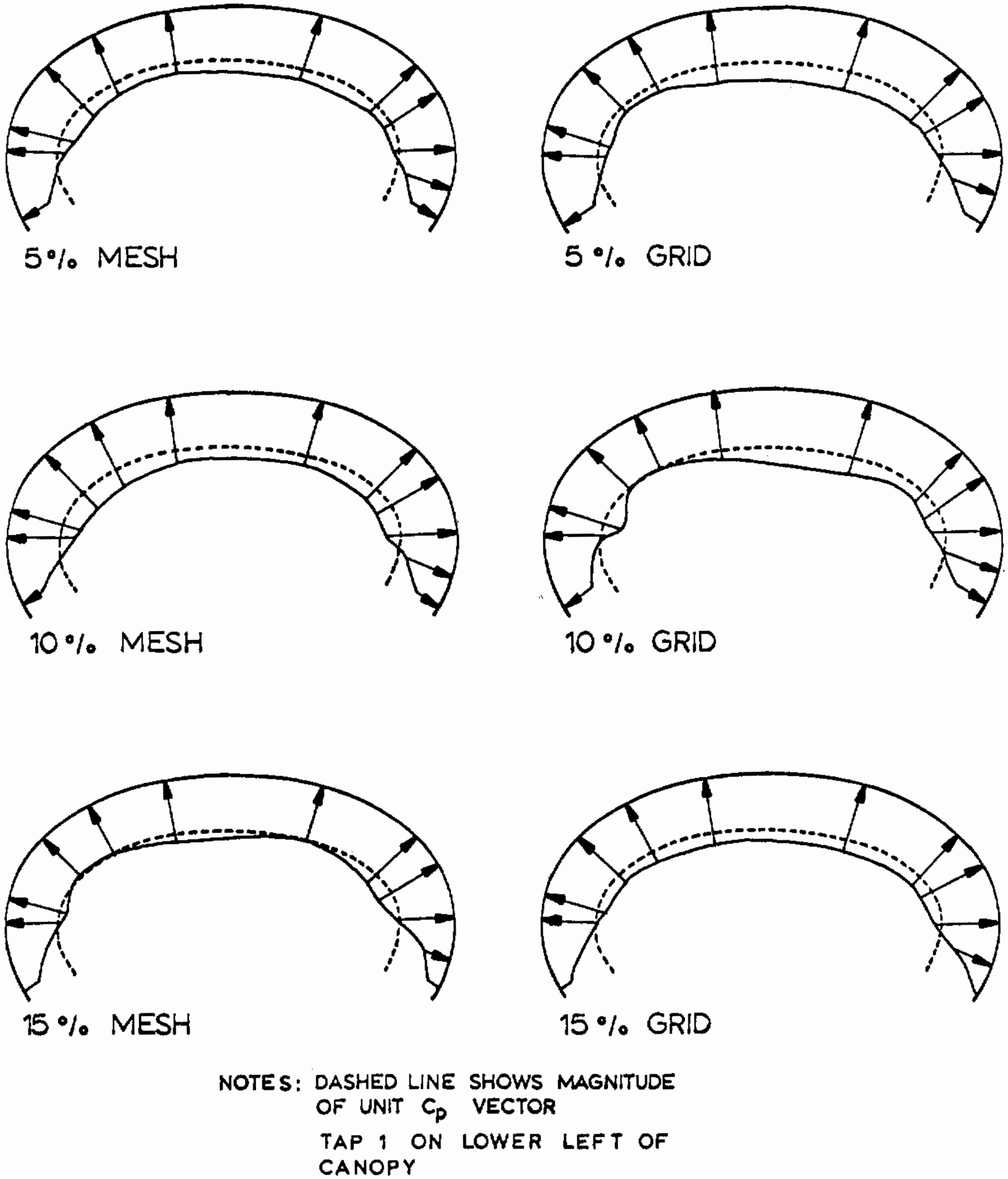

Fig 22. Schematic of Net Pressure Coefficient at $X/D_B = 7$ ($M_\infty \doteq 3.0$, Re/ft $\doteq 2.12 \times 10^6$)

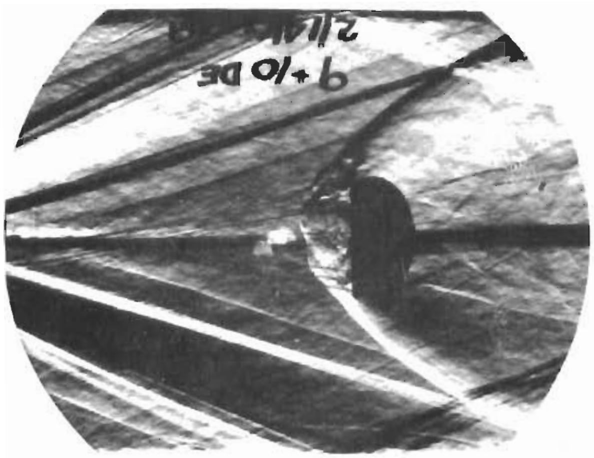

a. 5% MESH

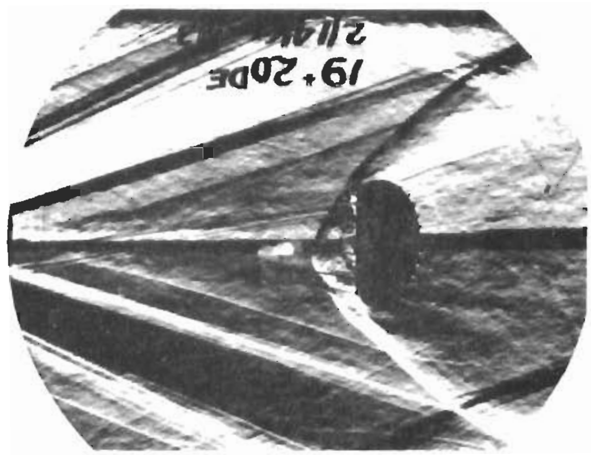

b. 5% GRID

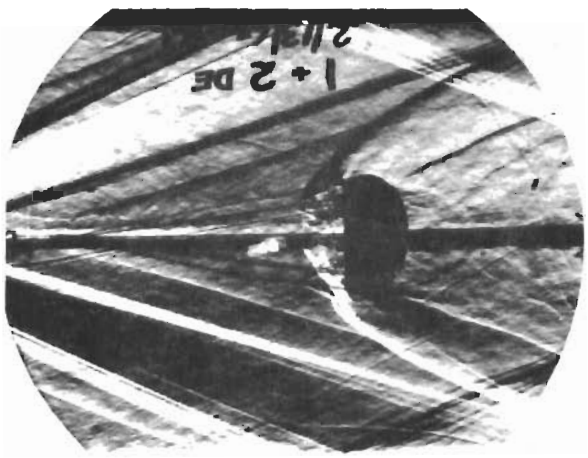

c. 10% MESH

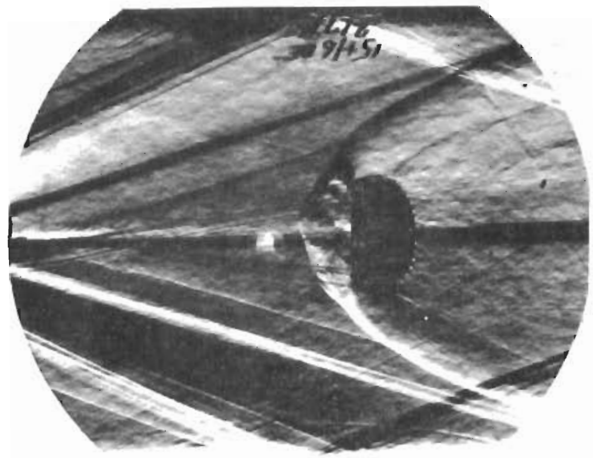

d. 10% GRID

e. 15% MESH

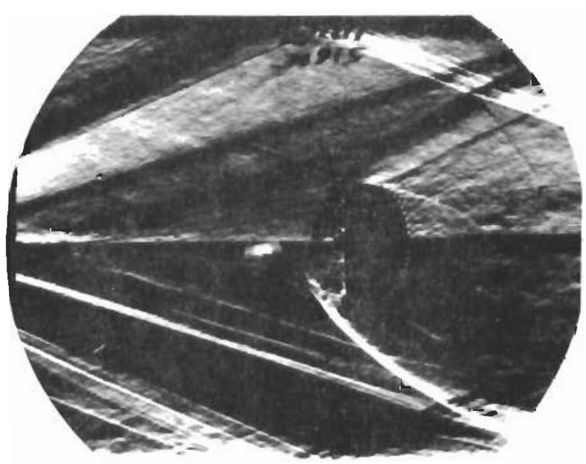

f. 15% GRID

Fig 23 Schlieren Photographs at $X/D_B = 7$
($M_\infty \doteq 3.0$, $Re/ft \doteq 2.12 \times 10^6$)

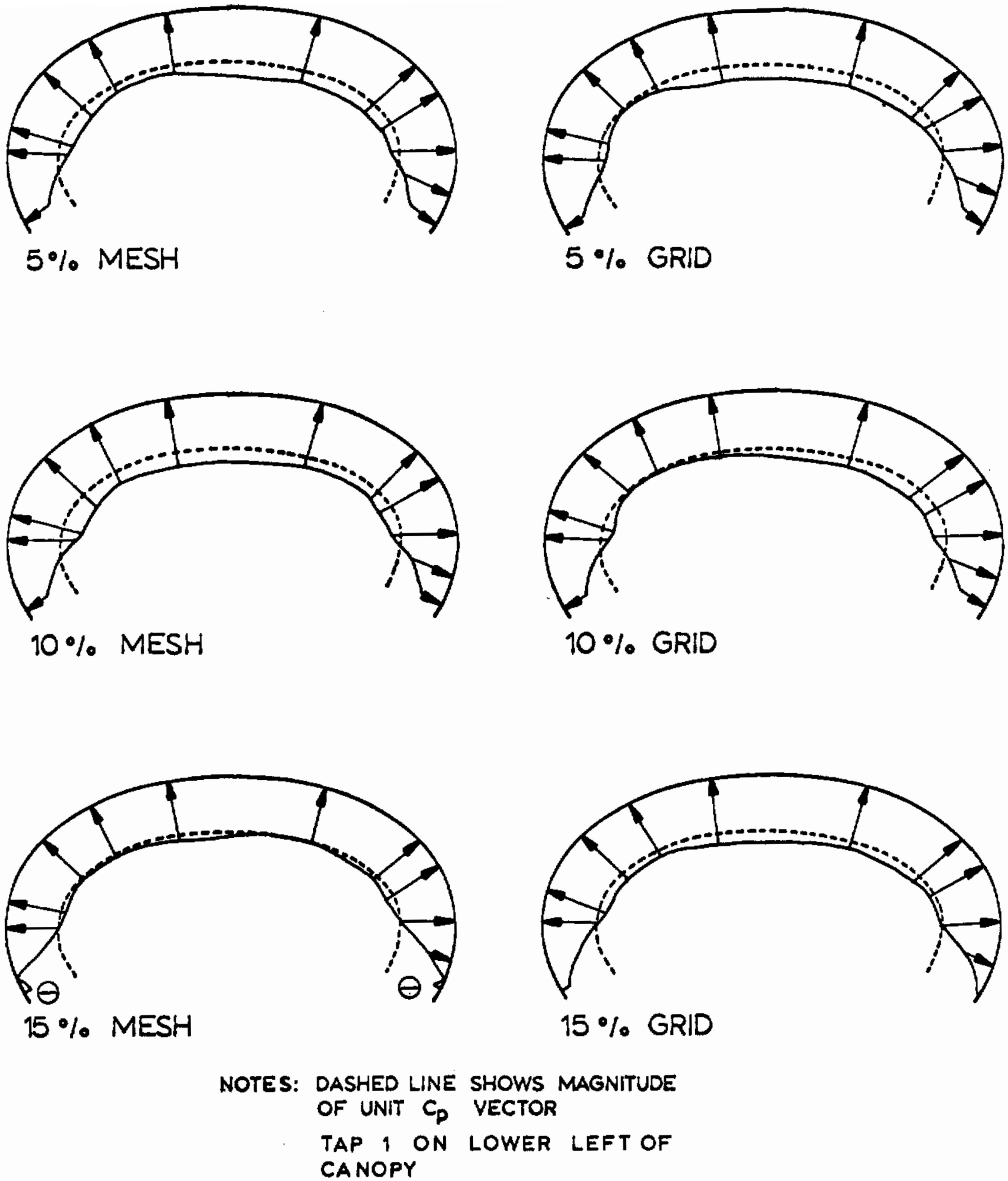

Fig 24. Schematic of Net Pressure Coefficient at $X/D_B = 8$ ($M_\infty \doteq 3.0$, $Re/ft \doteq 2.12 \times 10^6$)

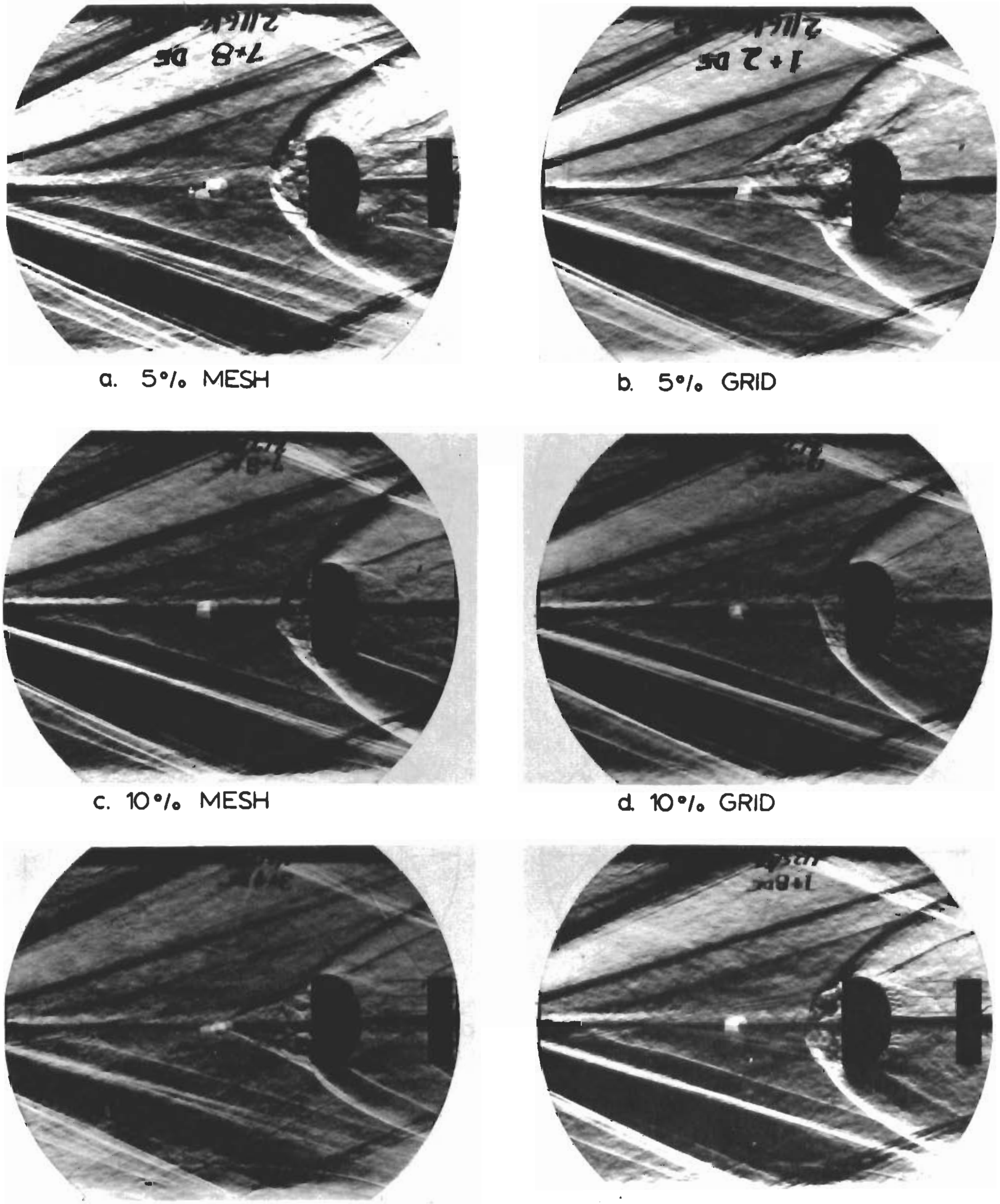

a. 5% MESH

b. 5% GRID

c. 10% MESH

d. 10% GRID

e. 15% MESH

f. 15% GRID

Fig 25 Schlieren Photographs at $X/D_B = 8$
($M_\infty \doteq 3.0$, $Re/ft \doteq 2.12 \times 10^6$)

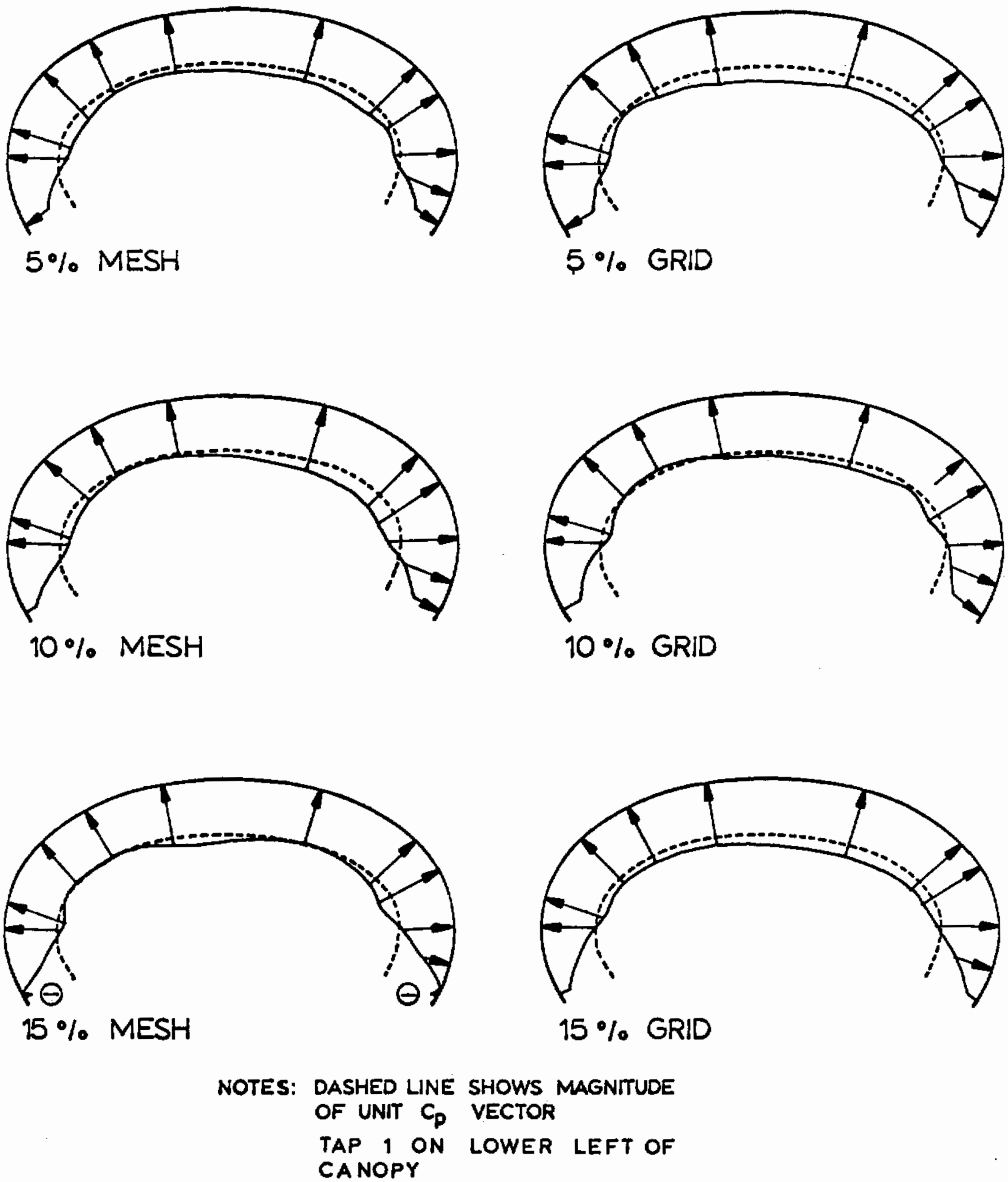

Fig 26. Schematic of Net Pressure Coefficient at $X/D_B = 9$ ($M_\infty \doteq 3.0$, $Re/ft \doteq 2.12 \times 10^6$)

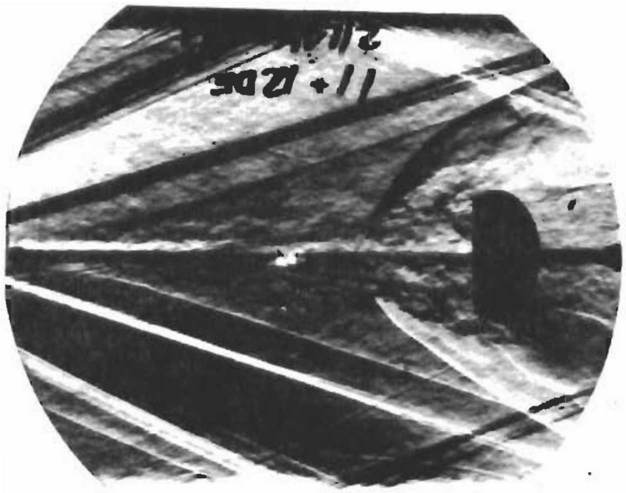

a. 5% MESH

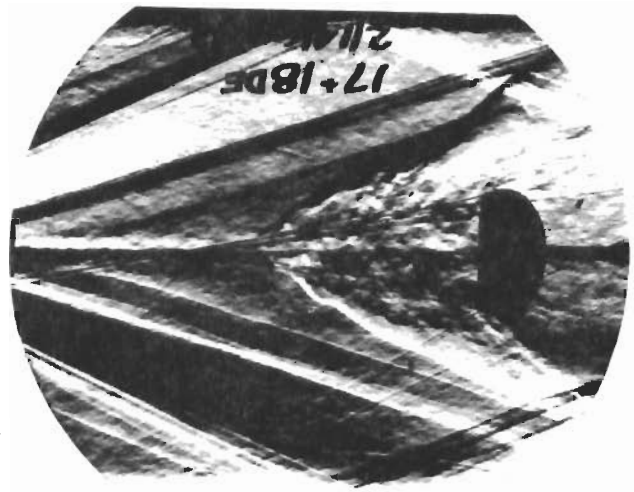

b. 5% GRID

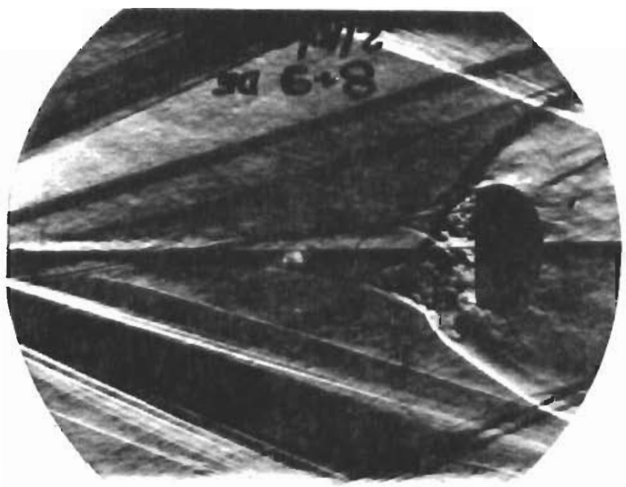

c. 10% MESH

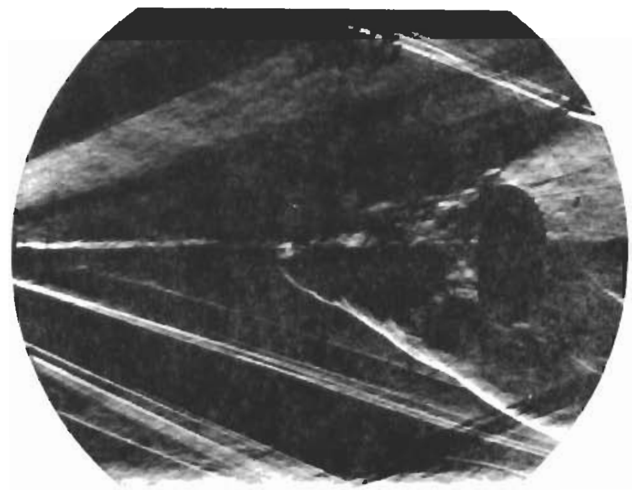

d. 10% GRID

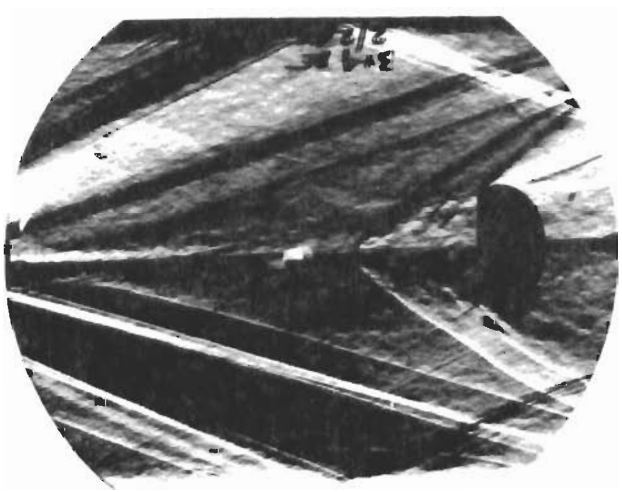

e. 15% MESH

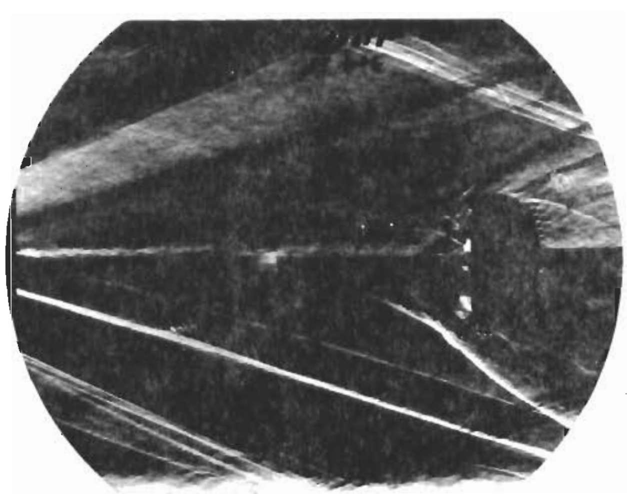

f. 15% GRID

Fig 27 Schlieren Photographs at $X/D_B = 9$
($M_\infty \doteq 3.0$, $Re/ft \doteq 2.12 \times 10^6$)

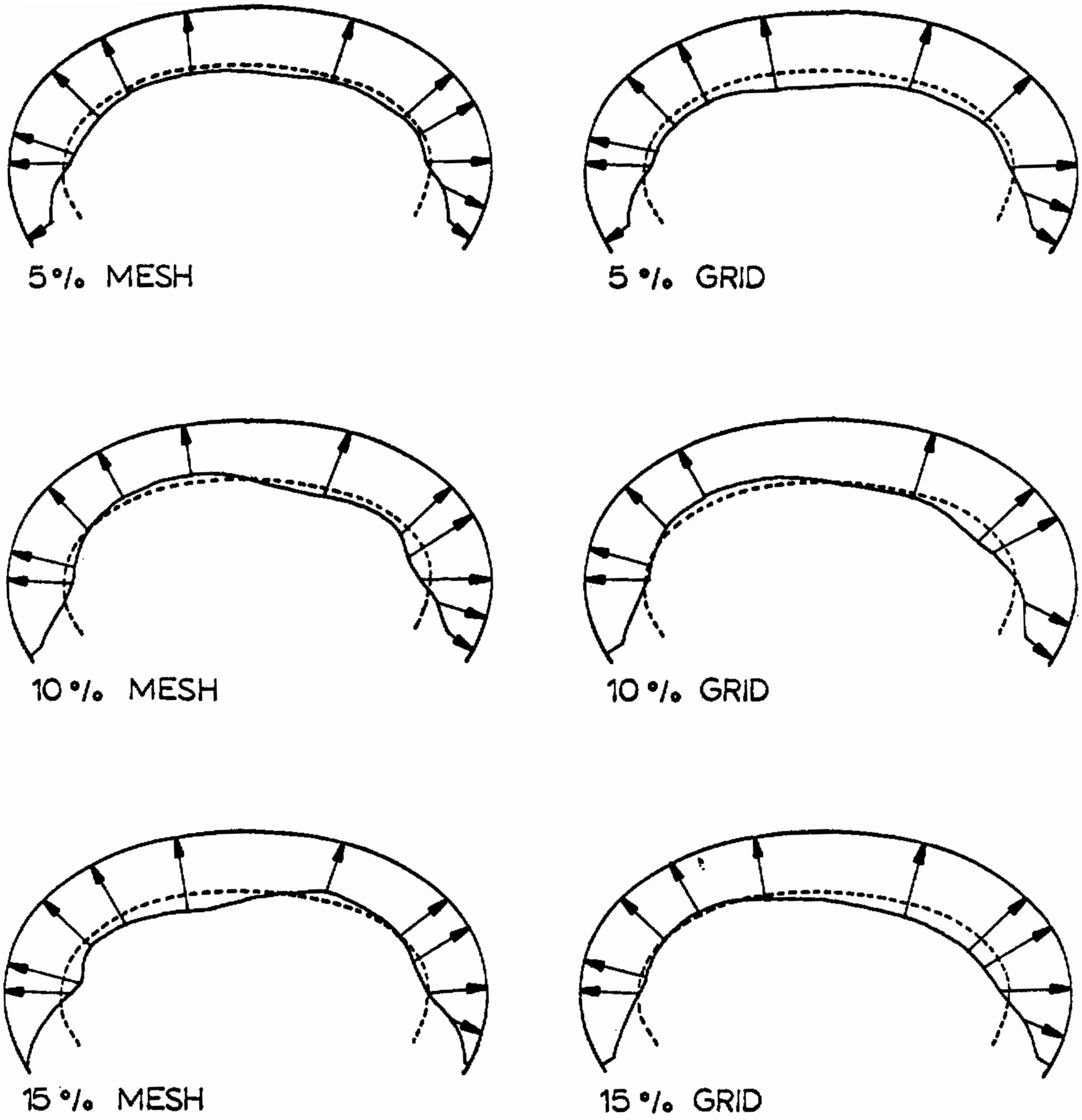

NOTES: DASHED LINE SHOWS MAGNITUDE OF UNIT C_p VECTOR

TAP 1 ON LOWER LEFT OF CANOPY

Fig 28. Schematic of Net Pressure Coefficient at $X/D_B = 11$ ($M_\infty \doteq 3.0$, $Re/ft \doteq 2.12 \times 10^6$)

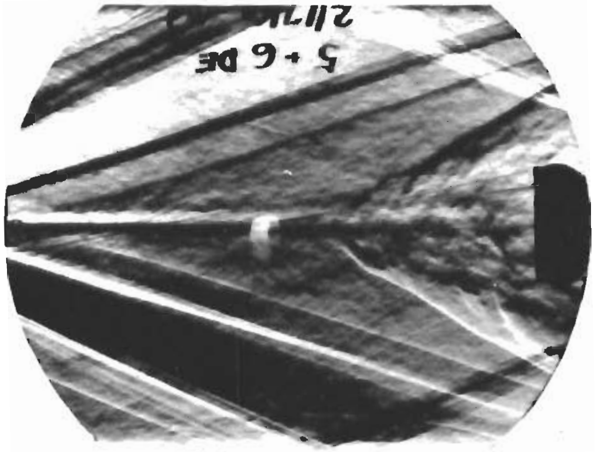

a. 5 % MESH

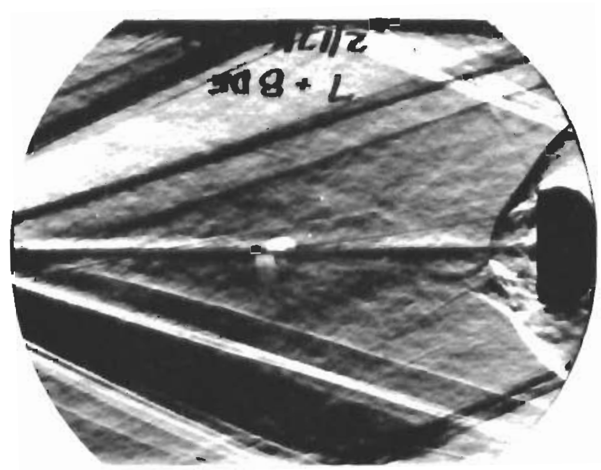

b. 5 % GRID

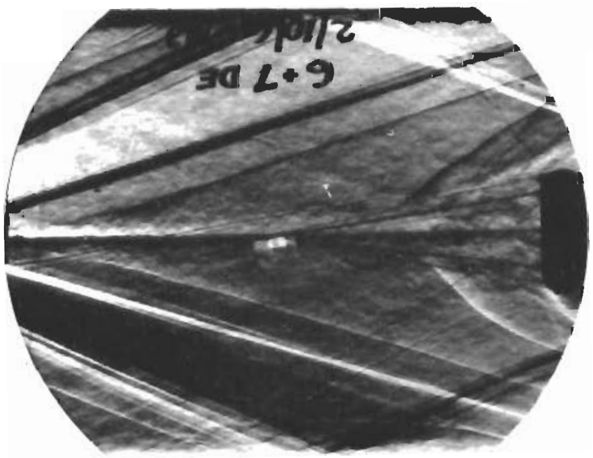

c. 10 % MESH

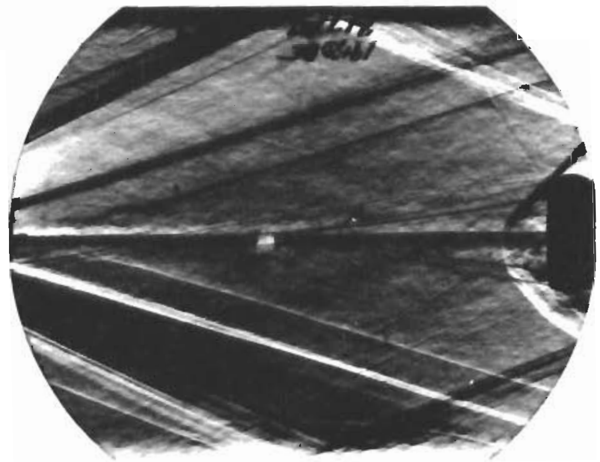

d. 10 % GRID

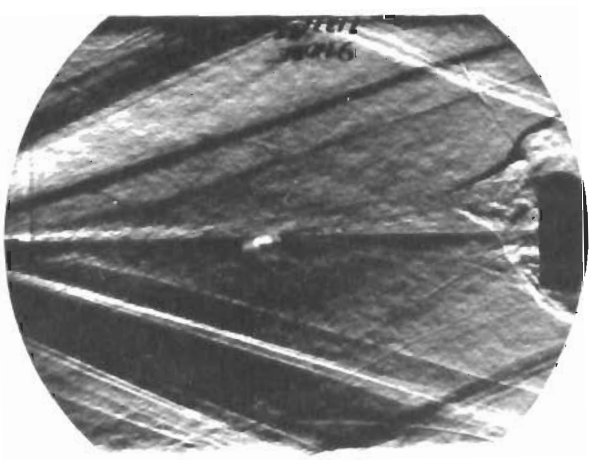

e. 15 % MESH

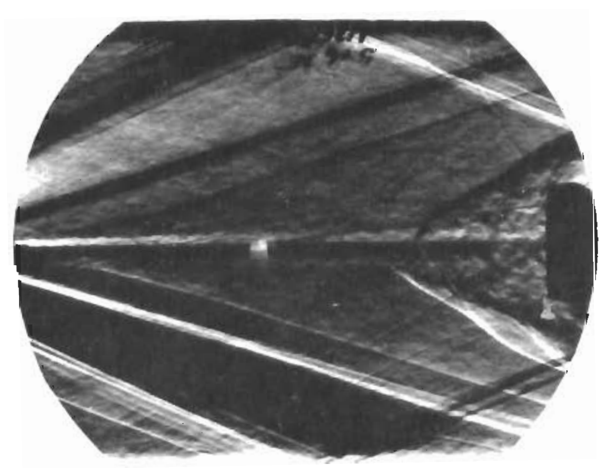

f. 15 % GRID

Fig 29 Schlieren Photographs at $X/D_B = 11$
($M_\infty \doteq 3.0$, $Re/ft \doteq 2.12 \times 10^6$)

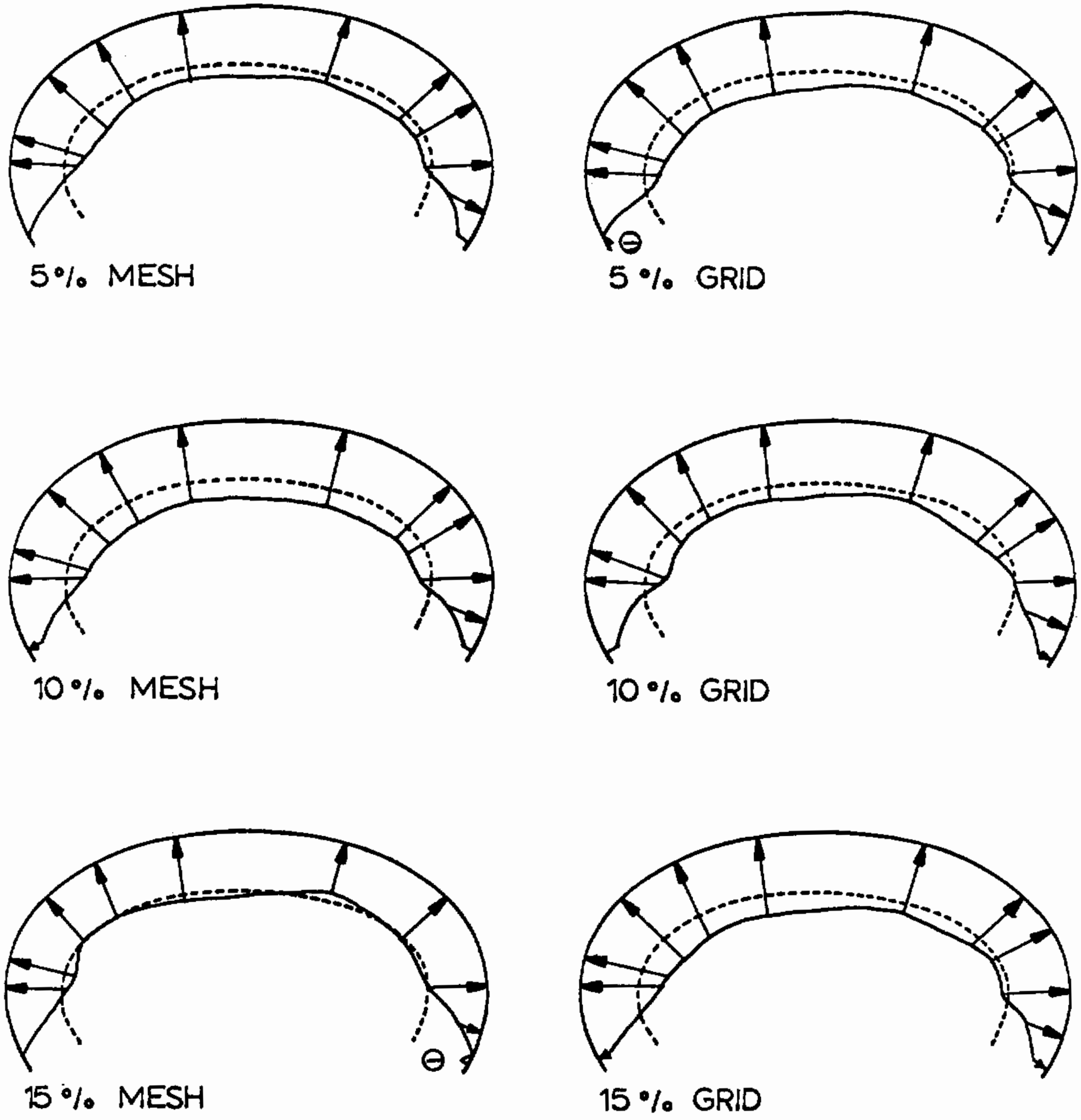

NOTES: DASHED LINE SHOWS MAGNITUDE OF UNIT C_p VECTOR

TAP 1 ON LOWER LEFT OF CANOPY

Fig 30. Schematic of Net Pressure Coefficient at $X/D_B = \infty$ ($M_\infty \doteq 3.0$, $Re/ft \doteq 2.12 \times 10^6$)

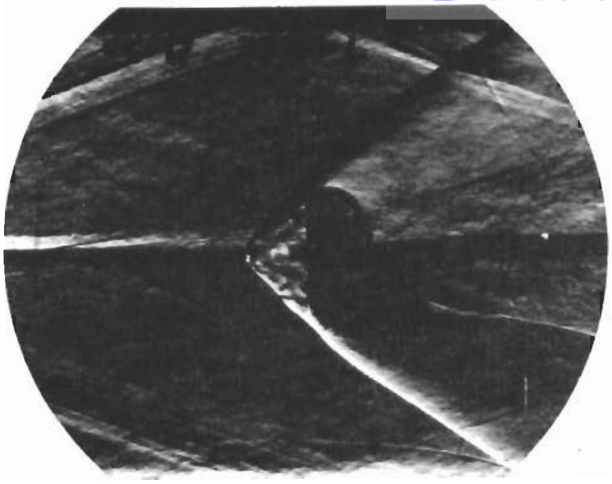

a. 5 % MESH

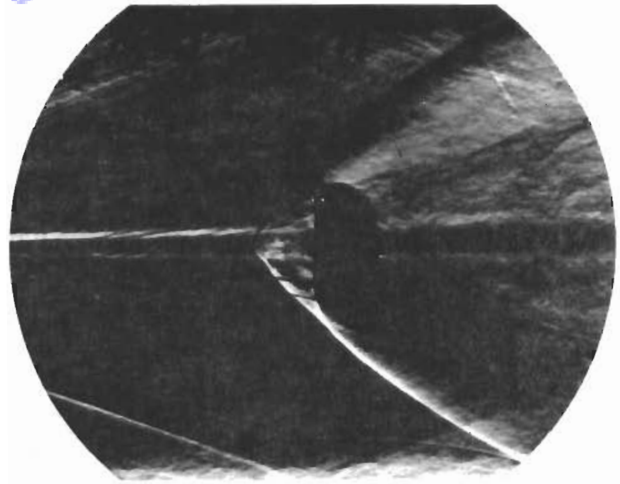

b. 5 % GRID

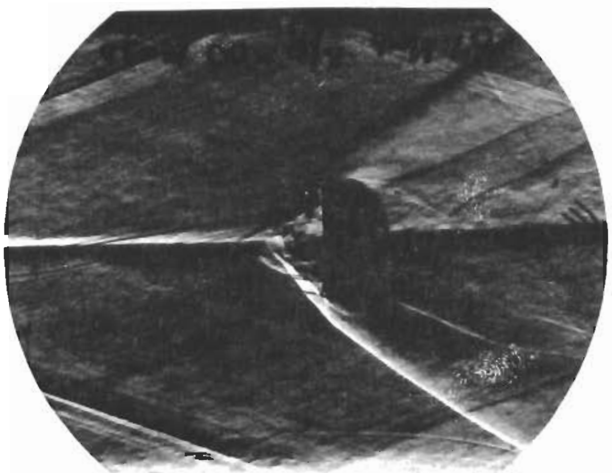

c. 10 % MESH

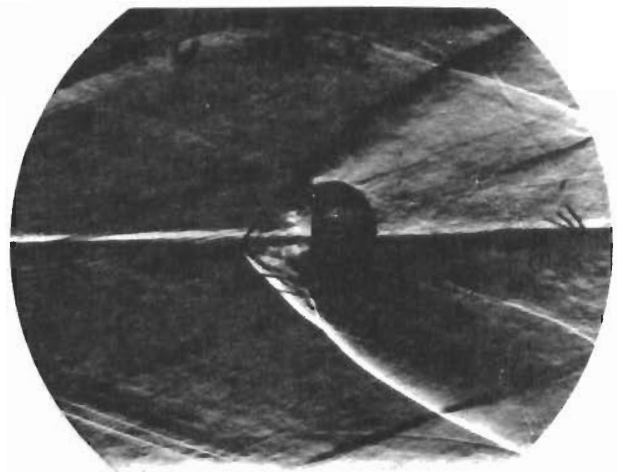

d. 10 % GRID

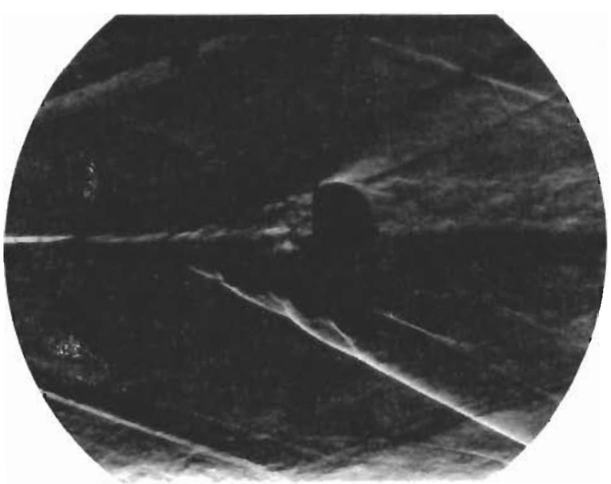

e. 15 % MESH

f. 15 % GRID

Fig 31 Schlieren Photographs at $X/D_B = \infty$
($M_\infty \doteq 3.0$, $Re/ft \doteq 2.12 \times 10^6$)

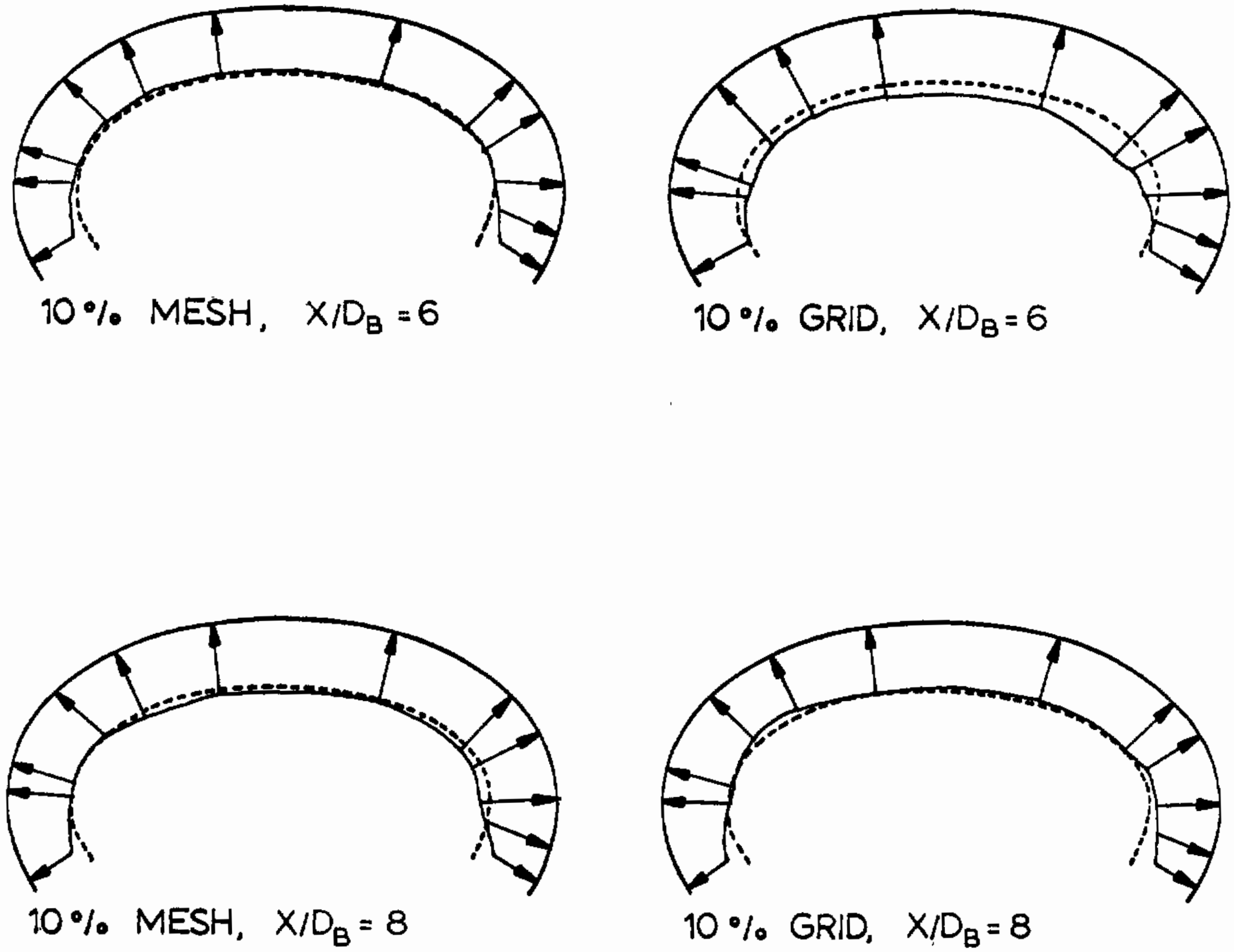

NOTES: DASHED LINE SHOWS MAGNITUDE OF UNIT C_p VECTOR

TAP 1 ON LOWER LEFT OF CANOPY

Fig 32. Schematic of Internal Pressure Coefficients for 10% Mesh and 10% Grid Models at $X/D_B = 6$ and 8 ($M_\infty \doteq 3.0$, $Re/ft \doteq 1.10 \times 10^6$)

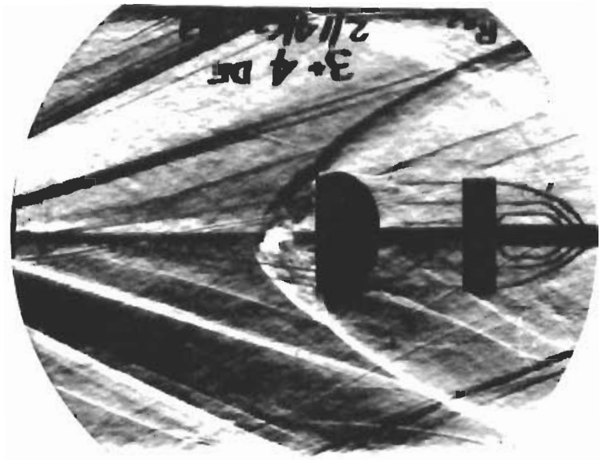

a. 10 % MESH, $X/D_B = 6$

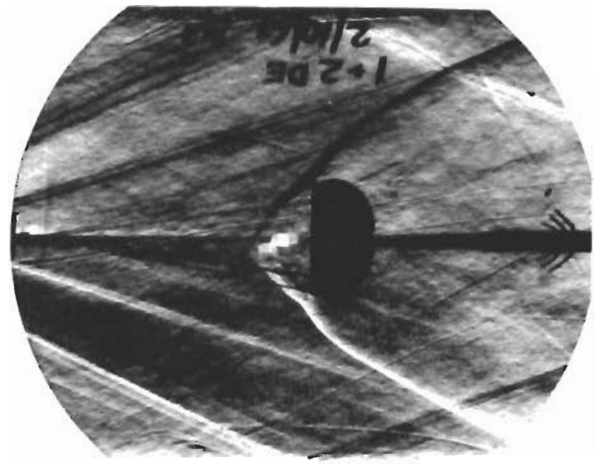

b. 10 % GRID, $X/D_B = 6$

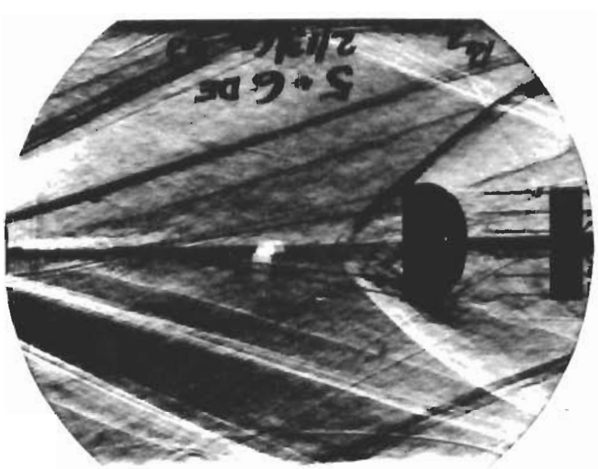

c. 10 % MESH, $X/D_B = 8$

d. 10 % GRID, $X/D_B = 8$

Fig 33 Schlieren Photographs of 10% Mesh and 10 % Grid Models at $X/D_B = 6$ & 8 ($M_\infty \doteq 3.0$, $Re/ft \doteq 1.10 \times 10^6$)

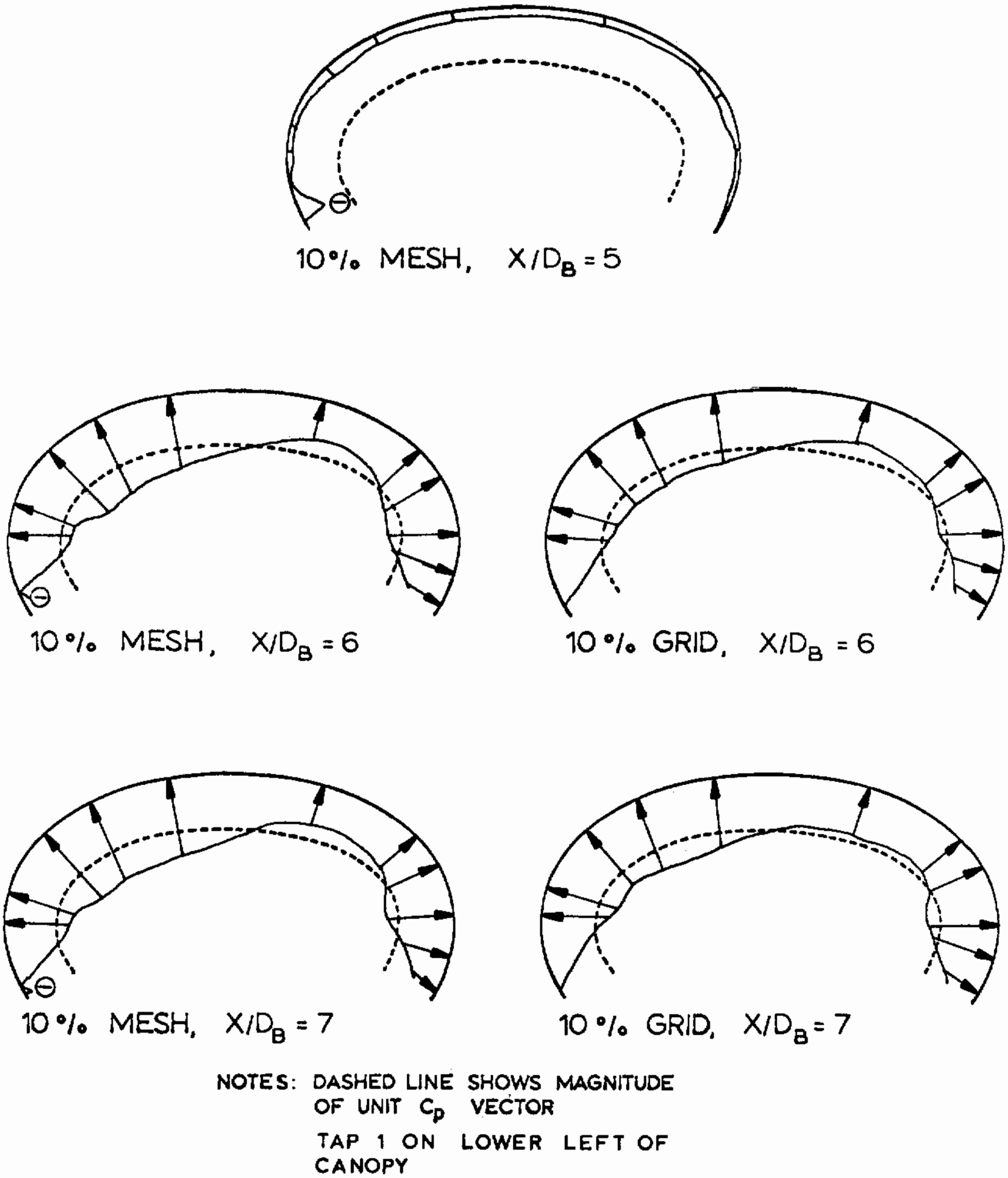

Fig 34. Schematic of Net Pressure Coefficients for 10% Mesh and 10% Grid Models at X/D_B = 5, 6, and 7 ($M_\infty \doteq 4.0$, Re/ft $\doteq 2.99 \times 10^6$)

a. 10 % MESH, $X/D_B = 5$

b. 10 % MESH, $X/D_B = 6$

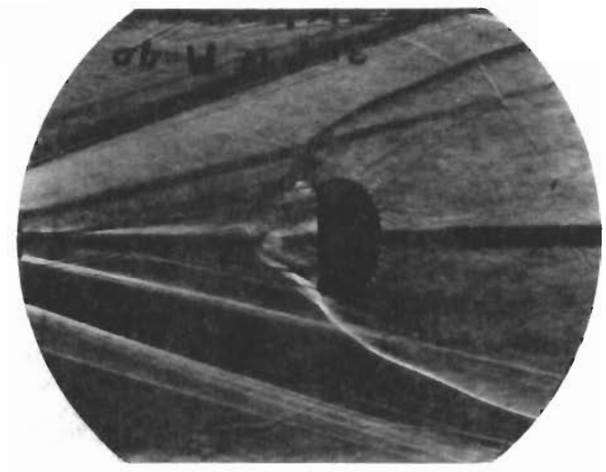

c. 10 % GRID, $X/D_B = 6$

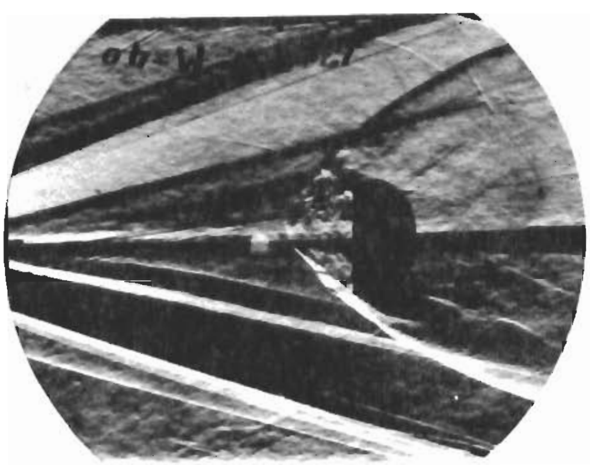

d. 10 % MESH, $X/D_B = 7$

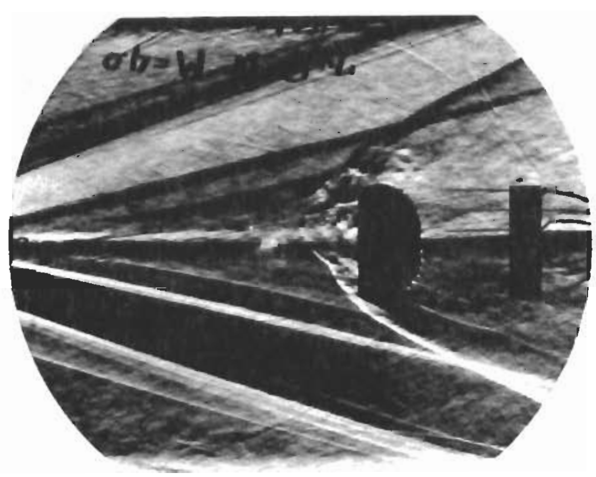

e. 10 % GRID, $X/D_B = 7$

Fig 35 Schlieren Photographs of 10 % Mesh and 10 % Grid Models at $X/D_B = 5$, 6 & 7 ($M_\infty \doteq 4.0$, $Re/ft \doteq 2.99 \times 10^6$)

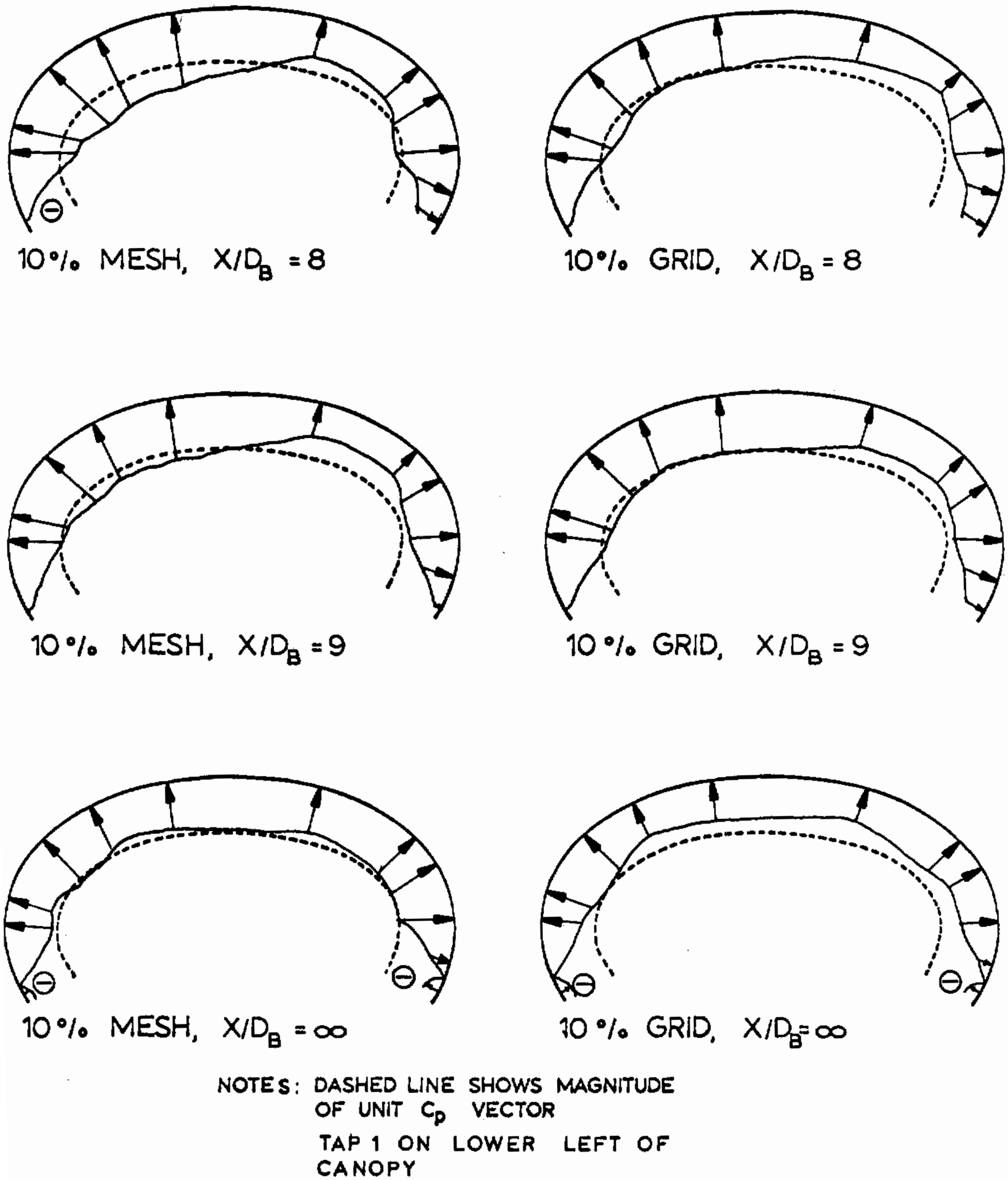

Fig 36. Schematic of Net Pressure Coefficients for 10% Mesh and 10% Grid Models at X/D$_B$ = 8, 9, and ∞ ($M_\infty \doteq 4.0$, Re/ft $\doteq 2.99 \times 10^6$)

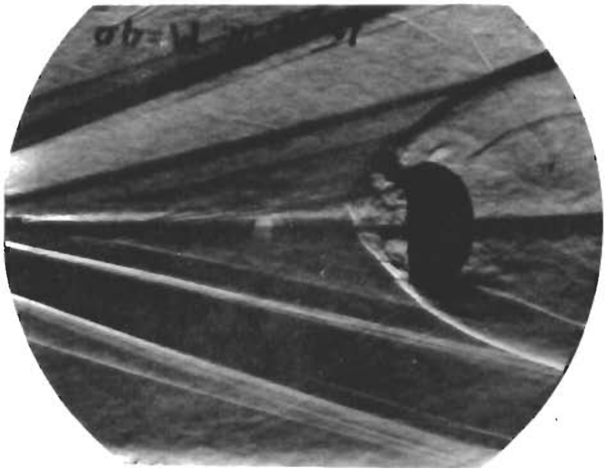

a. 10% MESH, $X/D_B = 8$

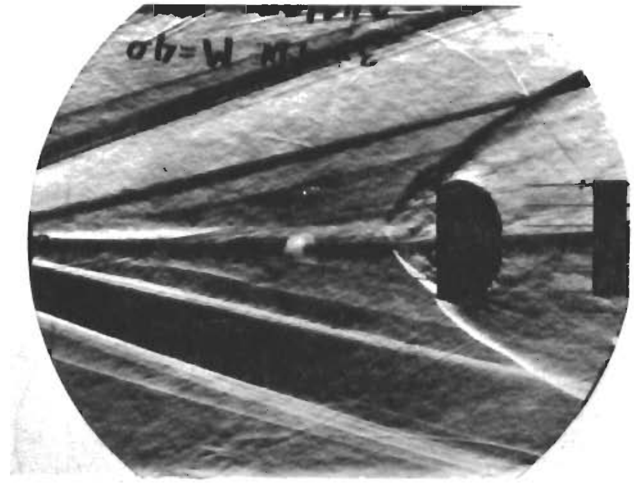

b. 10% GRID, $X/D_B = 8$

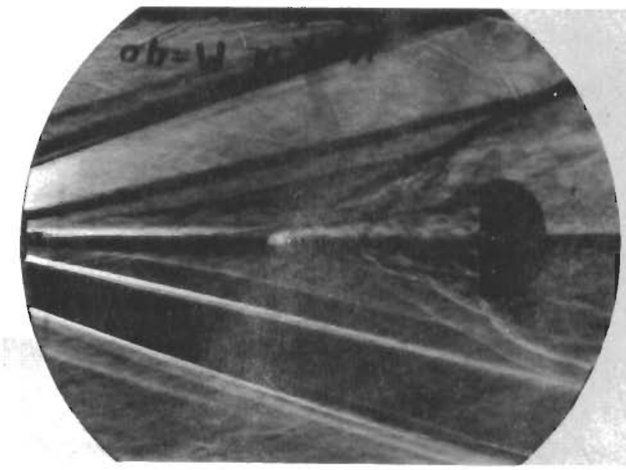

c. 10% MESH, $X/D_B = 9$

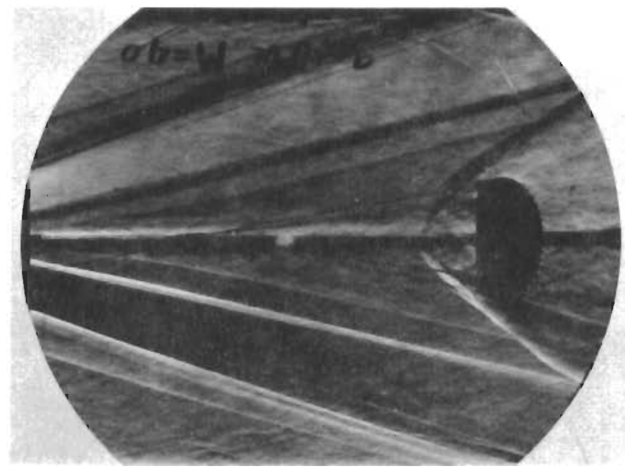

d. 10% GRID, $X/D_B = 9$

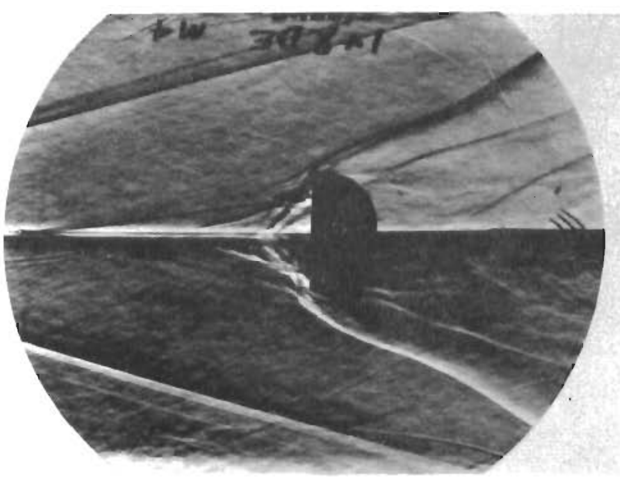

e. 10% MESH, $X/D_B = \infty$

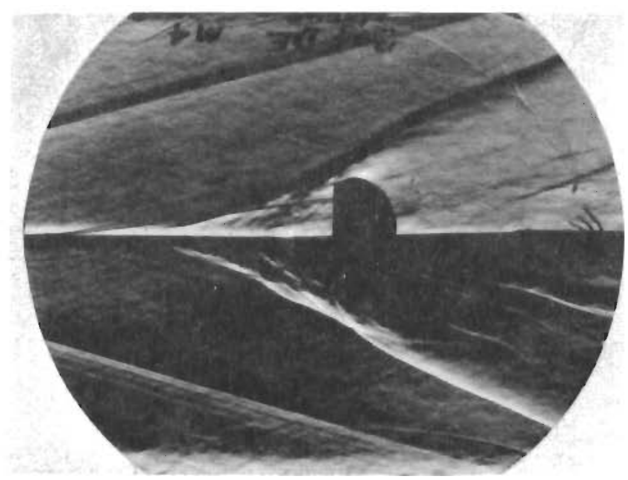

f. 10% GRID, $X/D_B = \infty$

Fig 37 Schlieren Photographs of 10% Mesh and 10% Grid Models at $X/D_B = 8, 9$ & ∞ ($M_\infty \doteq 4.0$, $Re/ft \doteq 2.99 \times 10^6$)

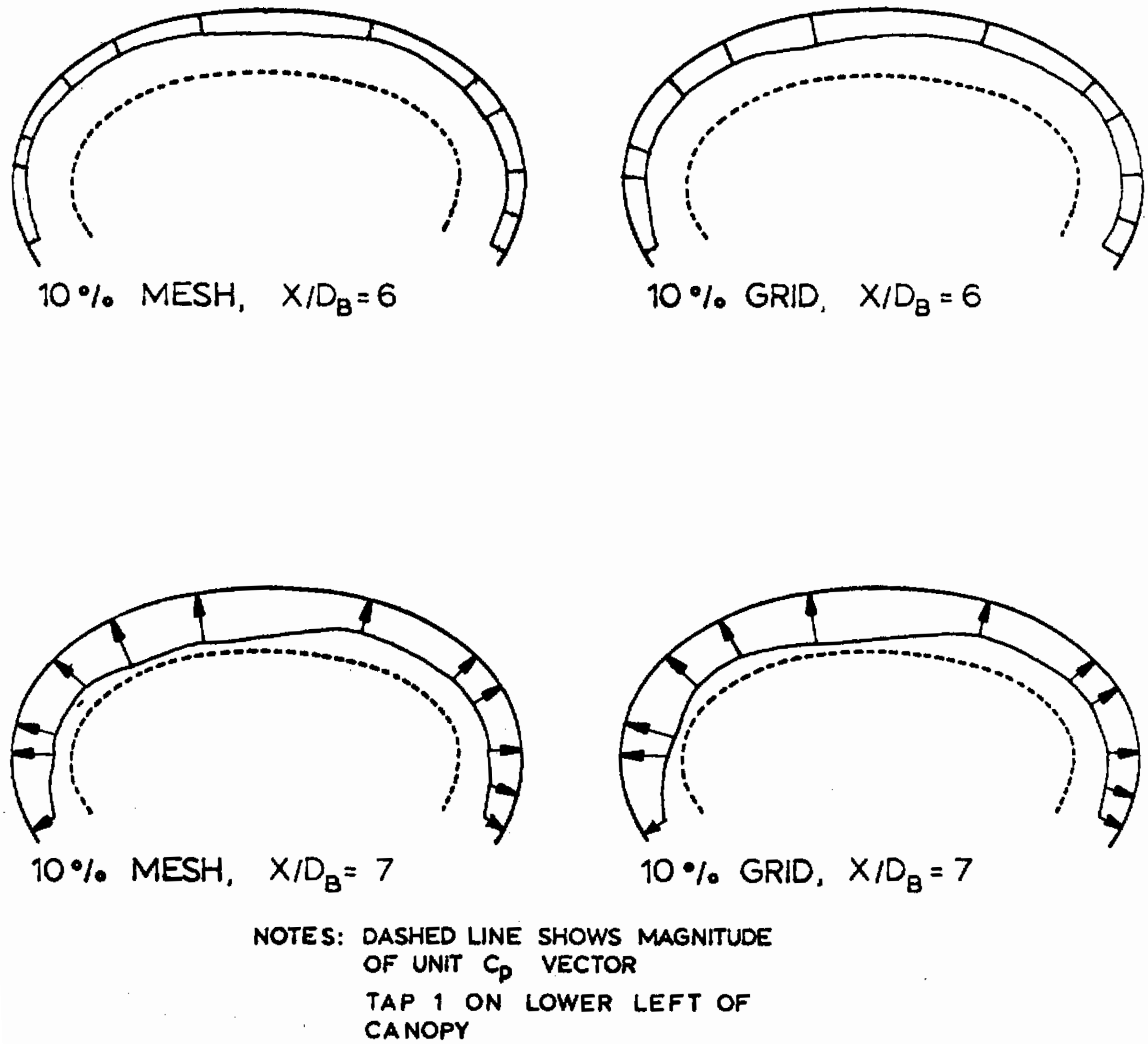

Fig 38. Schematic of Internal Pressure Coefficients for 10% Mesh and 10% Grid Models at X/D_B = 6 and 7 ($M_\infty \doteq 4.0$, Re/ft $\doteq 1.36 \times 10^6$)

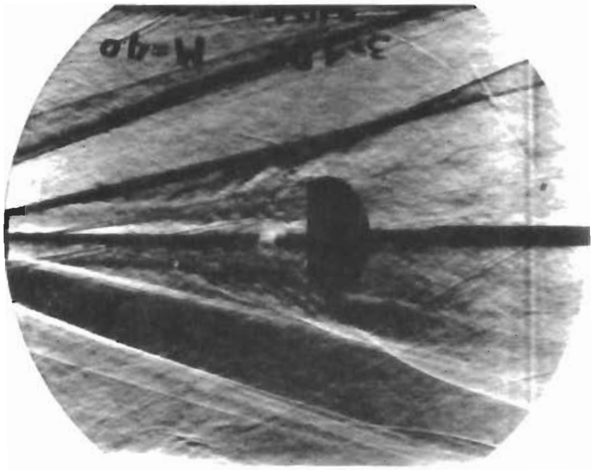

a. 10 °/o MESH, $X/D_B = 6$

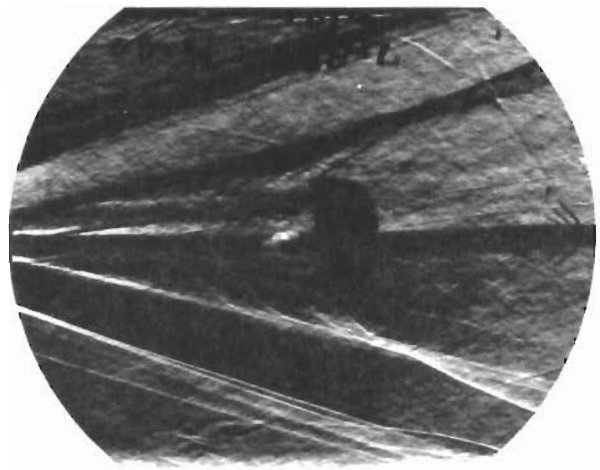

b. 10 °/o GRID, $X/D_B = 6$

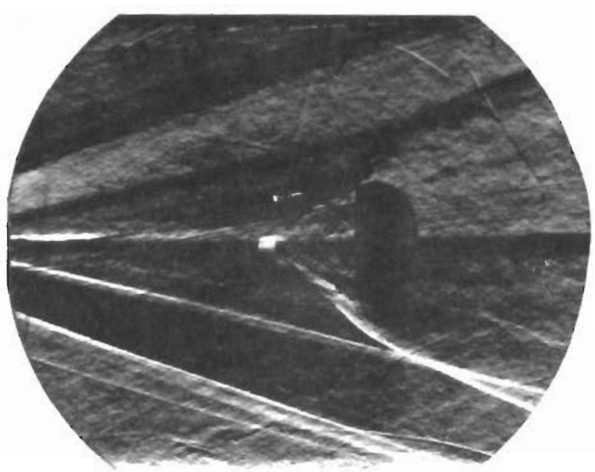

c. 10 °/o MESH, $X/D_B = 7$

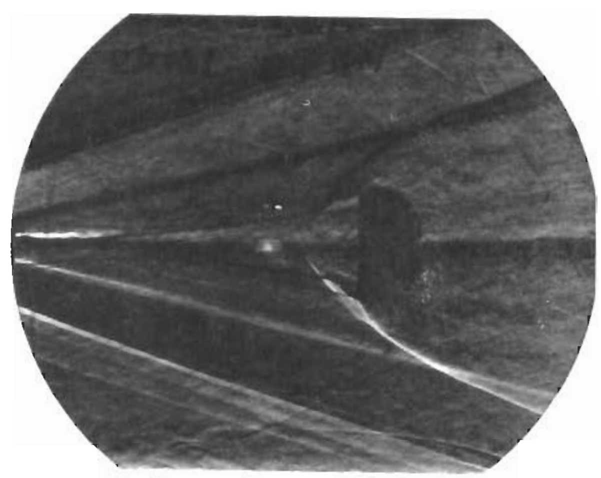

d. 10 °/o GRID, $X/D_B = 7$

Fig 39 Schlieren Photographs of 10 % Mesh and 10 % Grid Models at $X/D_B = 6$ & 7 ($M_\infty \doteq 4.0$, $Re/ft \doteq 1.36 \times 10^6$)

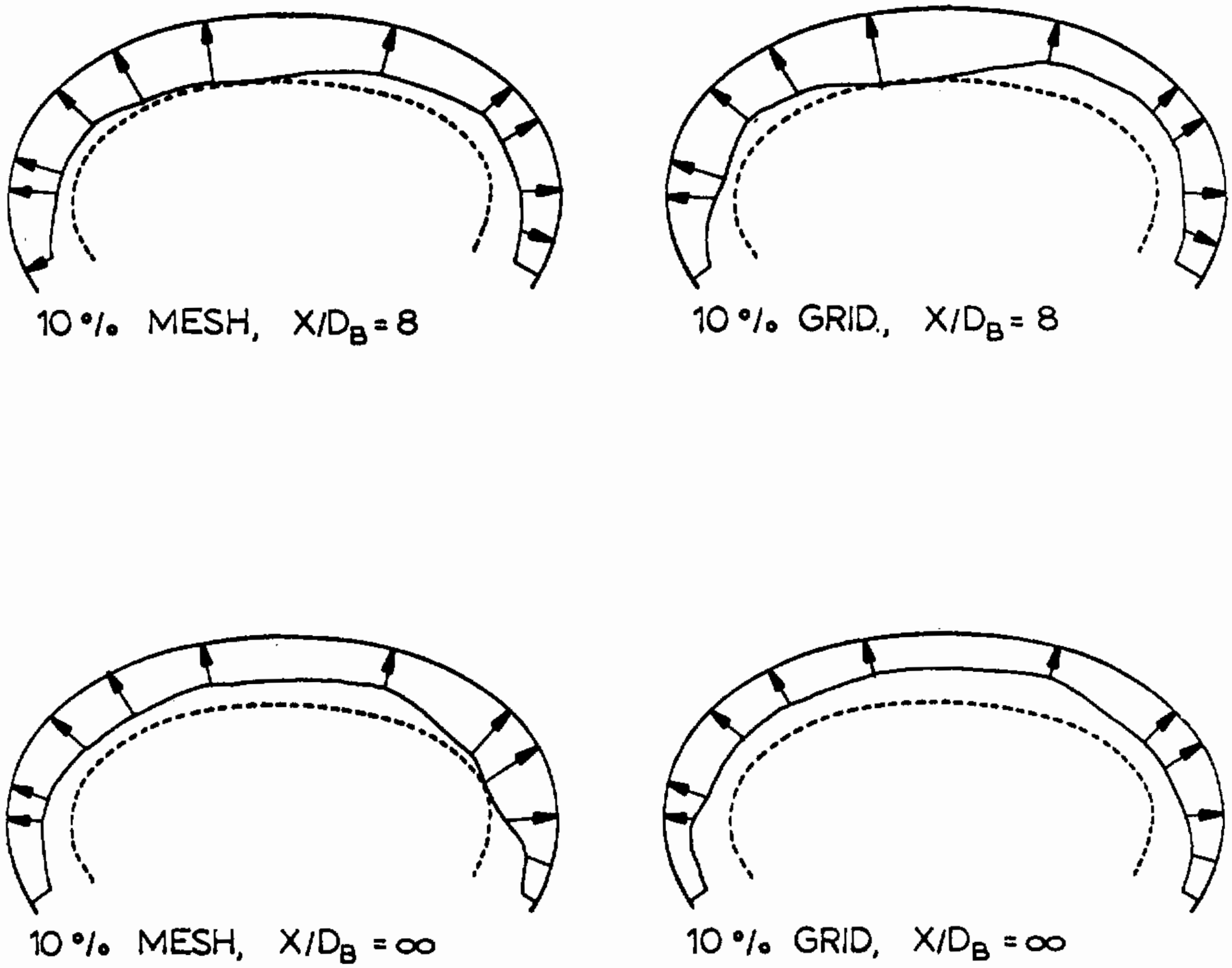

NOTES: DASHED LINE SHOWS MAGNITUDE OF UNIT C_p VECTOR

TAP 1 ON LOWER LEFT OF CANOPY

Fig 40. Schematic of Internal Pressure Coefficients for 10% Mesh and 10% Grid Models at X/D_B = 8 and ∞ ($M_\infty \doteq 4.0$, Re/ft $\doteq 1.36 \times 10^6$)

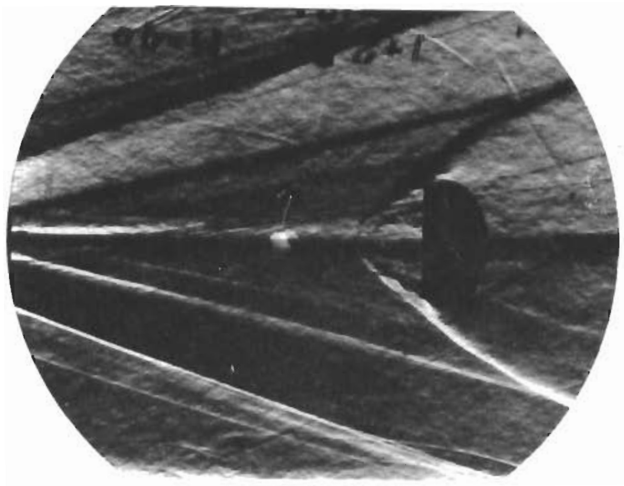

a. 10 % MESH, $X/D_B = 8$

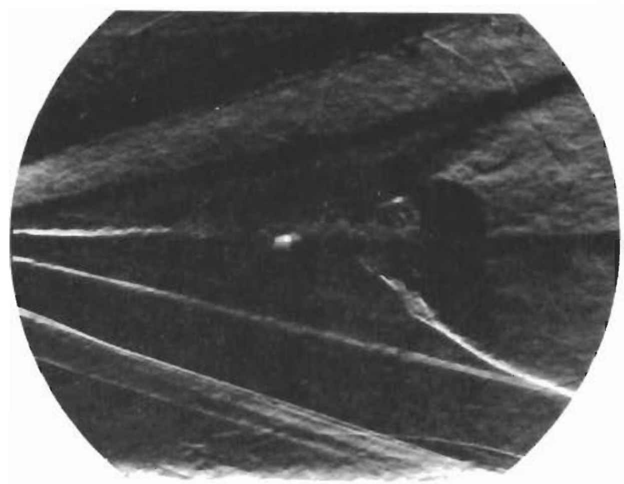

b. 10 % GRID, $X/D_B = 8$

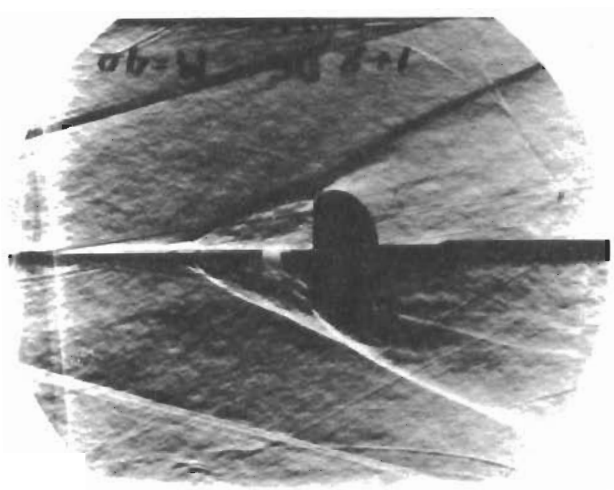

c. 10 % MESH, $X/D_B = \infty$

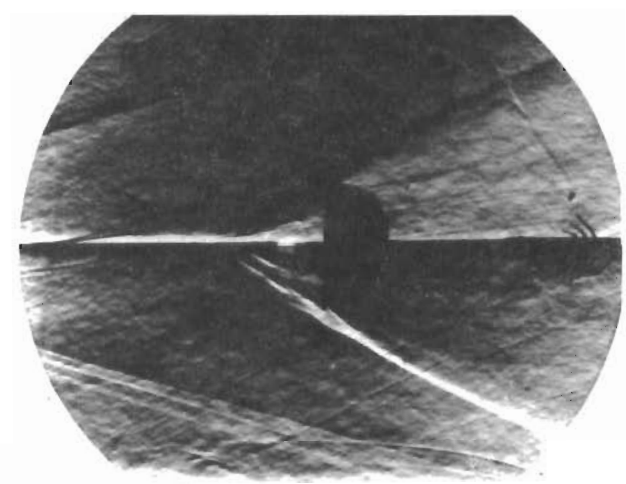

d. 10 % GRID, $X/D_B = \infty$

Fig 41 Schlieren Photographs of 10 % Mesh and 10 % Grid Models at $X/D_B = 8$ & ∞ ($M_\infty \doteq 4.0$, $Re/ft \doteq 1.36 \times 10^6$)

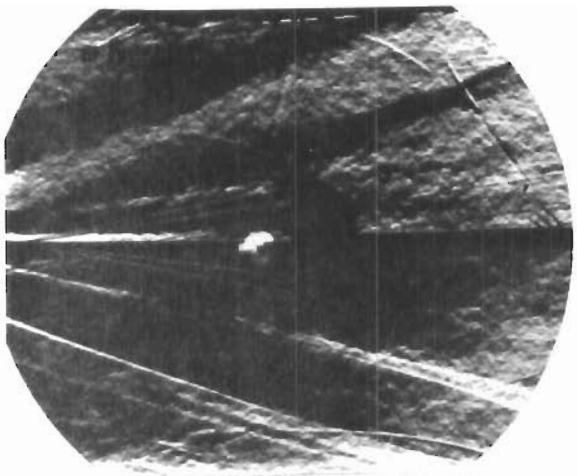

a. 10 % MESH, $X/D_B = 6$

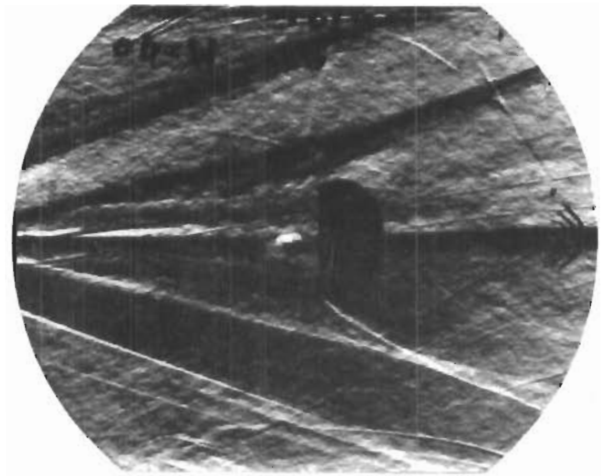

b. 10 % GRID, $X/D_B = 6$

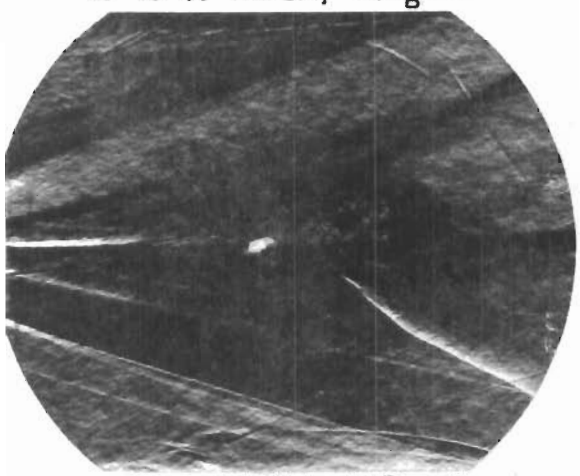

c. 10 % MESH, $X/D_B = 8$

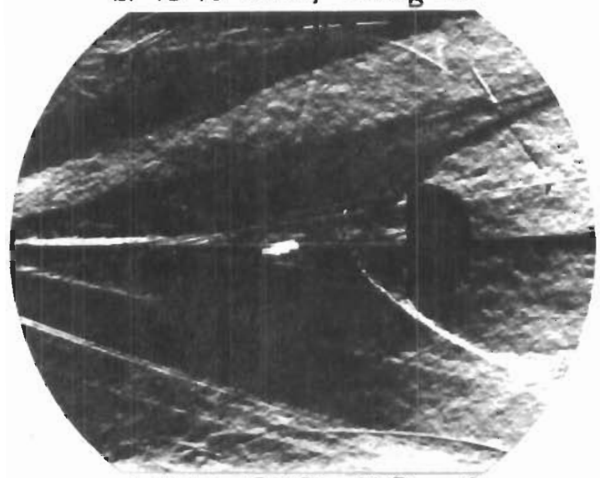

d. 10 % GRID, $X/D_B = 8$

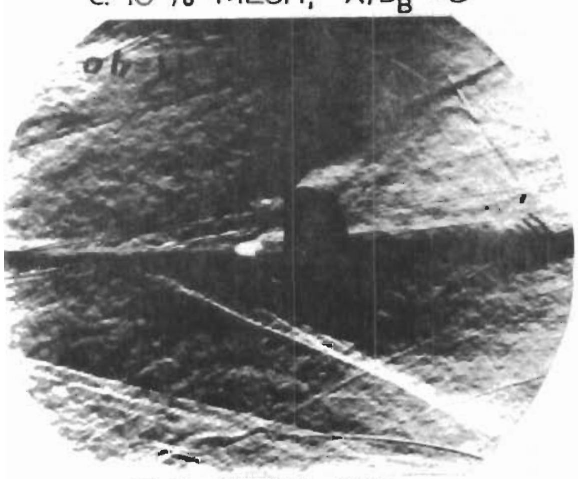

e. 10 % MESH, $X/D_B = \infty$

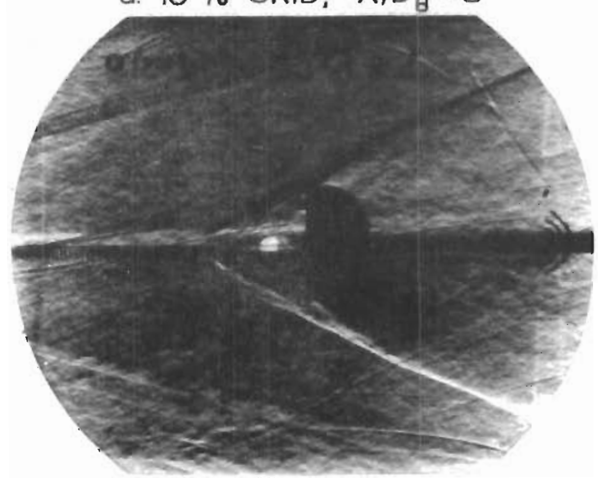

f. 10 % GRID, $X/D_B = \infty$

Fig 42 Schlieren Photographs of 10 % Mesh and 10 % Grid Models at $X/D_B = 6, 8$ & ∞ ($M_\infty \doteq 4.0$, $Re/ft \doteq 0.86 \times 10^6$)

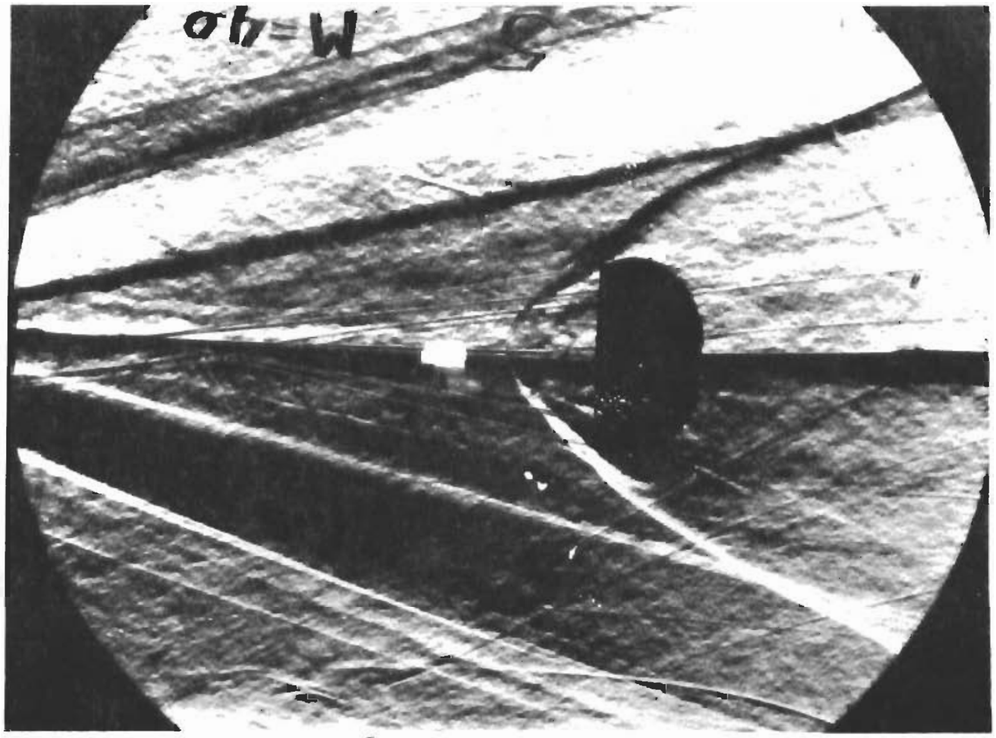

a. Re/ft = 0.86×10^6

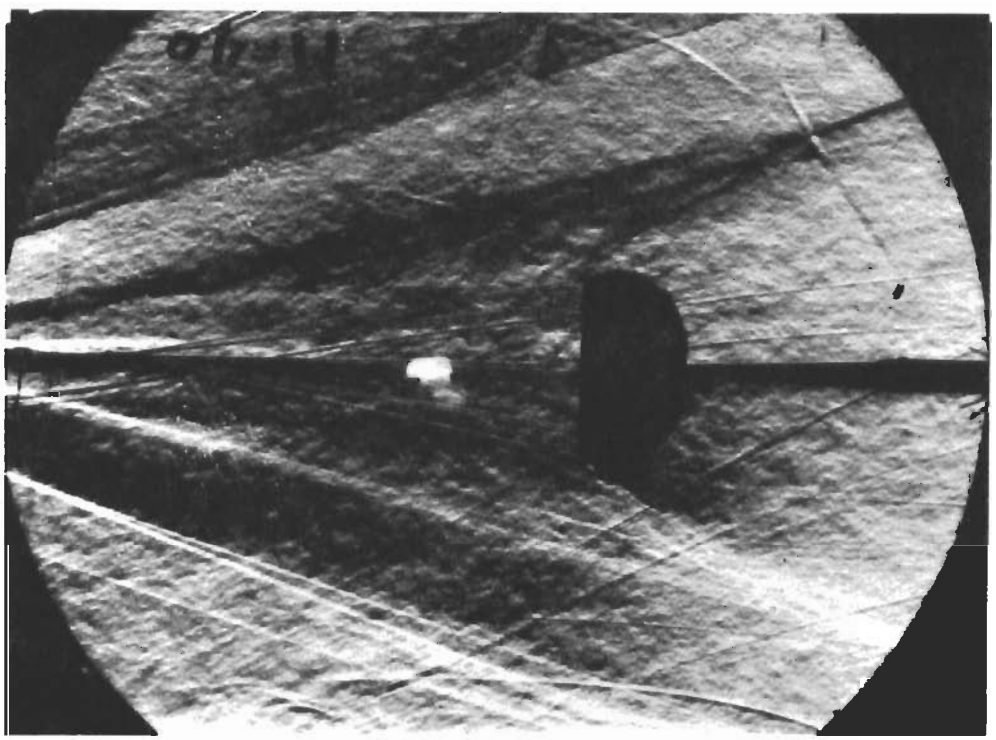

b. Re/ft = 0.56×10^6

Fig 43 Schlieren Photographs of 10% Grid Model at $X/D_B = 7$ ($M_\infty \doteq 4.0$)

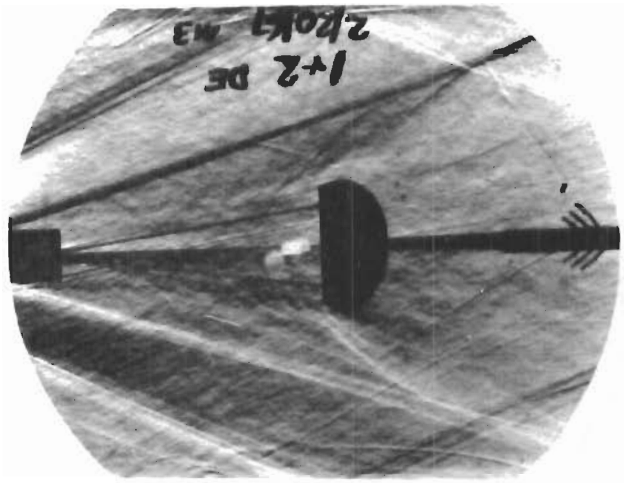

a. 10 % MESH, $X/D_B = 5$
$M_\infty \doteq 3.0$, $Re/ft = 1.10 \times 10^6$

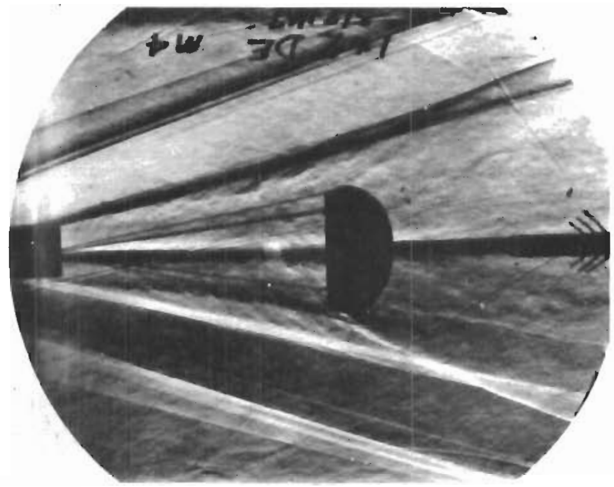

b 10 % MESH, $X/D_B = 5$
$M_\infty \doteq 4.0$, $Re/ft = 2.99 \times 10^6$

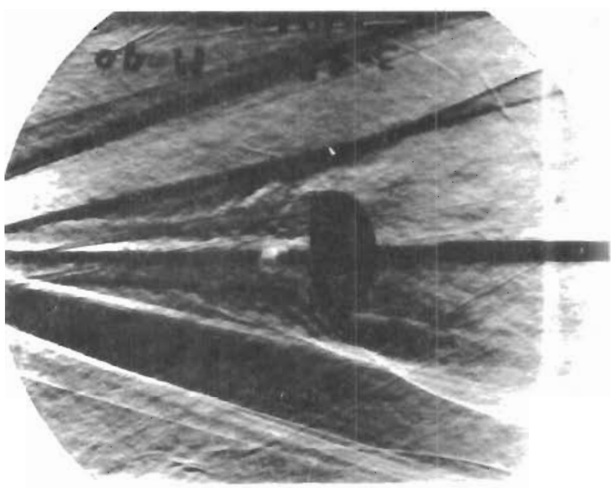

c 10 % MESH, $X/D_B \doteq 6$
$M_\infty \doteq 4.0$, $Re/ft = 1.36 \times 10^6$

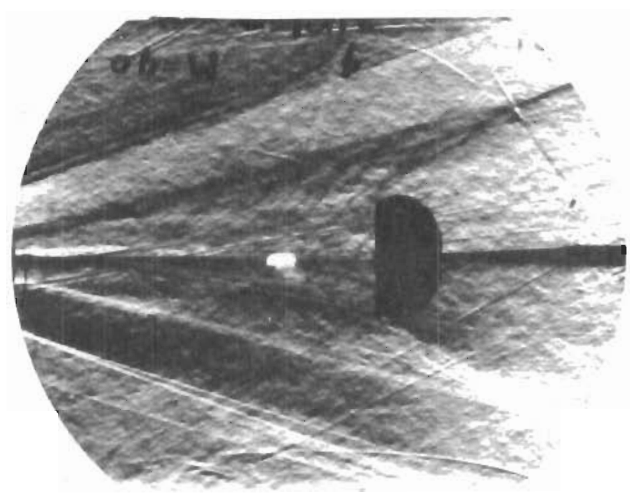

d 10 % MESH, $X/D_B = 7$
$M_\infty \doteq 4.0$, $Re/ft = 0.58 \times 10^6$

Fig 44 Maximum X/D_B, Maximum Re/ft, Blown Wake Condition for 10% Model at Mach 3 and Mach 4

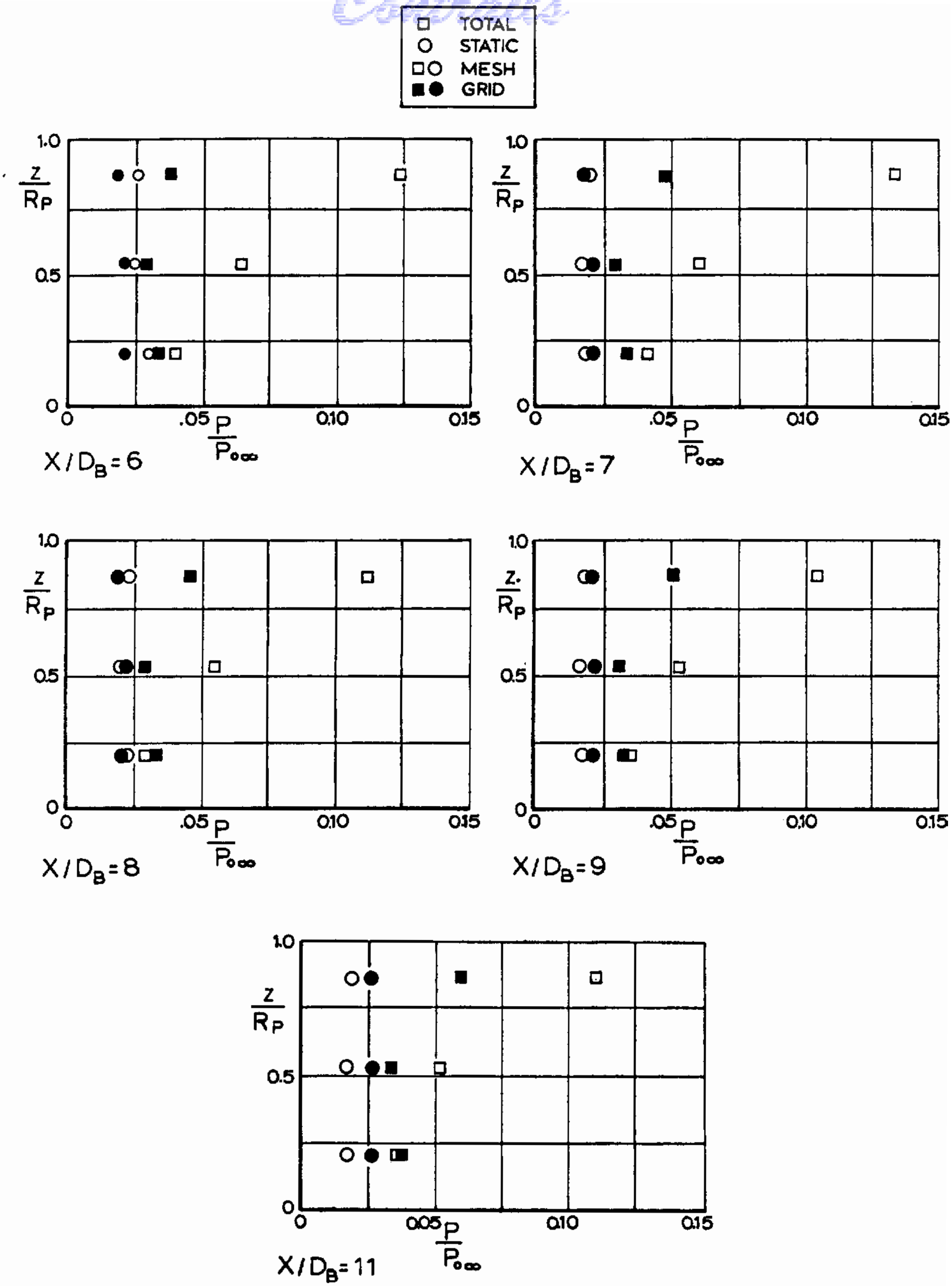

Fig 45. Canopy Near Wake Pressure for 5% Mesh and Grid Models at X/D_B = 6, 7, 8, 9, and 11 ($M_\infty \doteq 3.0$, Re/ft $\doteq$ 2.1[illegible] x 10^6).

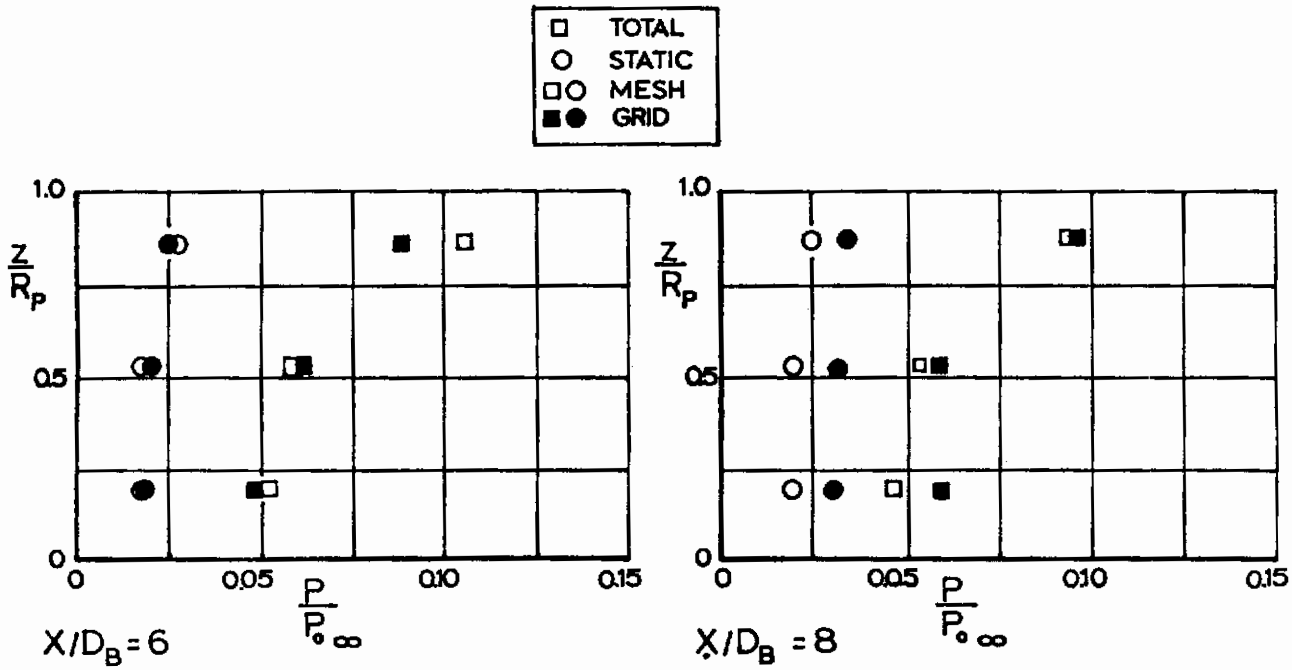

a. 10% MESH AND GRID MODELS (MESH EDGE AT $\frac{Z}{R_P}$=0.753, GRID EDGE AT $\frac{Z}{R_P}$=0.878)

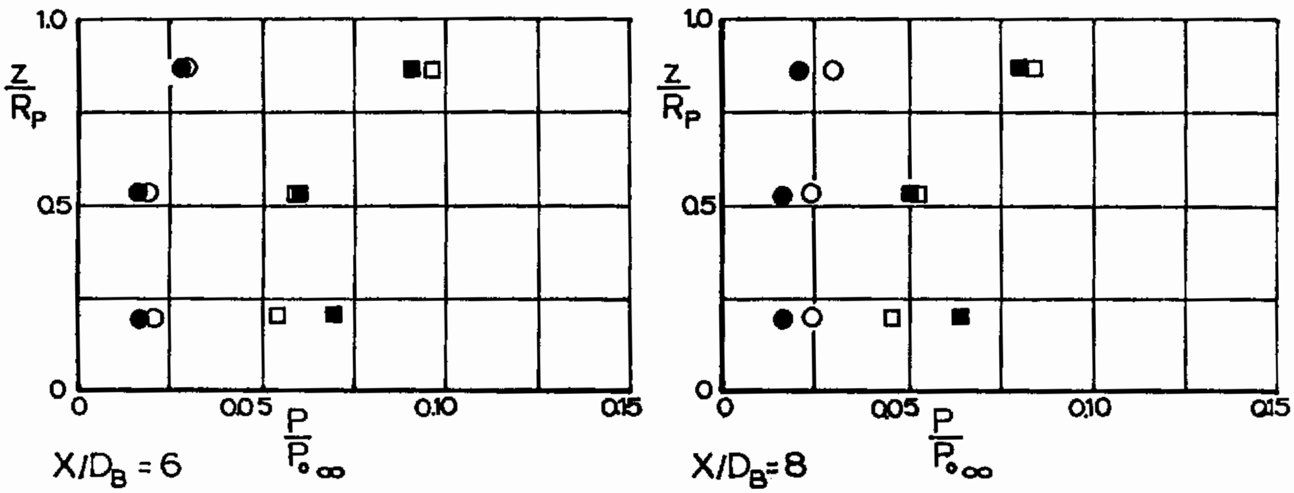

b. 15% MESH AND GRID MODELS (MESH EDGE AT $\frac{Z}{R_P}$=0.878, GRID EDGE AT $\frac{Z}{R_P}$= 0.878)

Fig 46. Canopy Near Wake Pressures for 10% and 15% Mesh and Grid Models at X/D_B = 6 and 8 ($M_\infty \doteq 3.0$, Re/ft $\doteq 2.12 \times 10^6$)

TABLE I

Coordinates of Established Hyperflo Parachute Profile

Y_c/R_p	X_c/R_p
0.000	0.000
0.003	0.063
0.005	0.109
0.008	0.155
0.010	0.181
0.015	0.230
0.025	0.297
0.035	0.350
0.050	0.412
0.065	0.461
0.080	0.501
0.100	0.545
0.125	0.597
0.150	0.643
0.175	0.685
0.200	0.723
0.250	0.788
0.300	0.839
0.350	0.885
0.400	0.921
0.450	0.949
0.500	0.971
0.550	0.987
0.600	0.997
0.650	1.000
0.700	0.993
0.750	0.983
0.800	0.967
0.850	0.949
0.900	0.927
0.950	0.905
0.992	0.885

TABLE II

Exact Tap Locations for the Hyperflo Models

5% MESH

Tap No	Int.	Taps	Ext.	Taps
	X_c/R_p	Y_c/R_p	X_c/R_p	Y_c/R_p
1	.880	.933	.893	.960
2	.980	.600	.993	.667
3	.953	.500	.980	.560
4	.800	.253	.820	.293
5	.600	.127	.600	.140
6	.233	.020	.260	.013
7	-.407	.040	-.387	.047
8	-.807	.253	-.800	.273
9	-.893	.353	-.900	.380
10	-1.000	.607	-1.000	.633
11	-.960	.780	-.967	.807
12	-.907	.927	-.900	.967

5% GRID

Tap No	Int.	Taps	Ext.	Taps
	X_c/R_p	Y_c/R_p	X_c/R_p	Y_c/R_p
1	.880	.927	.887	.960
2	.980	.620	.994	.654
3	.960	.514	.974	.527
4	.787	.247	.787	.260
5	.614	.133	.620	.140
6	.267	.020	.260	.020
7	-.427	.060	-.434	.067
8	-.780	.247	-.787	.260
9	-.900	.394	-.900	.400
10	-.987	.627	-.994	.654
11	-.947	.794	-.954	.827
12	-.887	.927	-.887	.967

10% MESH

Tap No	Int.	Taps	Ext.	Taps
	X_c/R_p	Y_c/R_p	X_c/R_p	Y_c/R_p
1	.907	.927	.887	.954
2	.987	.634	.994	.640
3	.960	.520	.980	.554
4	.814	.280	.800	.287
5	.614	.140	.607	.147
6	.247	.033	.233	.020
7	-.400	.047	-.414	.067
8	-.807	.260	-.800	.293
9	-.900	.374	-.914	.427
10	-.987	.607	-1.000	.667
11	-.954	.794	-.954	.847
12	-.907	.907	-.887	.980

10% GRID

Tap No	Int.	Taps	Ext.	Taps
	X_c/R_p	Y_c/R_p	X_c/R_p	Y_c/R_p
1	.894	.867	.894	.974
2	.987	.614	1.000	.660
3	.967	.520	.974	.514
4	.807	.267	.814	.280
5	.620	.133	.614	.133
6	.260	.027	.253	.013
7	-.420	.053	-.427	.060
8	-.814	.273	-.814	.293
9	-.894	.374	-.920	.427
10	-.987	.627	-.994	.660
11	-.960	.787	-.954	.834
12	-.900	.920	-.887	.967

15% MESH

Tap No	Int.	Taps	Ext.	Taps
	X_c/R_p	Y_c/R_p	X_c/R_p	Y_c/R_p
1	.914	.900	.894	.994
2	.980	.640	1.000	.680
3	.960	.520	.974	.540
4	.807	.293	.814	.280
5	.614	.153	.620	.147
6	.253	.027	.247	.020
7	-.407	.067	-.427	.067
8	-.814	.267	-.820	.300
9	-.914	.394	-.907	.420
10	-1.000	.634	-.994	.680
11	-.980	.774	-.954	.847
12	-.920	.907	-.887	.980

15% GRID

Tap No	Int.	Taps	Ext.	Taps
	X_c/R_p	Y_c/R_p	X_c/R_p	Y_c/R_p
1	.887	.940	.894	.960
2	.987	.647	1.000	.647
3	.960	.515	.974	.514
4	.827	.300	.827	.280
5	.567	.127	.567	.113
6	.273	.040	.273	.020
7	-.367	.047	-.367	.047
8	-.820	.287	-.820	.300
9	-.907	.387	-.907	.414
10	-.987	.634	-.987	.647
11	-.960	.800	-.954	.814
12	-.894	.934	-.880	.967

TABLE III

Test Program

Models	X/D_B	M_∞	Re/ft	Average Stagnation Pressure	Average Stagnation Temperature
ALL	6,7,8,9,11,∞	3	2.12 x 10^6	13.1 psia	70°F
*10% Mesh int	5	3	1.10	6.86 psia	71°F
10% Mesh int	6,8	3	1.10	6.86 psia	71°F
10% Grid int	6,8	3	1.10	6.86 psia	71°F
10% Mesh int and ext	5,6,7,8,9,∞	4	2.99	28.2 psia	42°F
10% Grid int and ext	6,7,8,9,∞	4	2.99	28.2 psia	42°F
10% Mesh int	6,7,8,∞	4	1.36	14.0 psia	71°F
10% Grid int	6,7,8,∞	4	1.36	14.0 psia	71°F
*10% Mesh int	6,7,8,∞	4	0.86	9.06 psia	78°F
*10% Grid int	6,7,8,∞	4	0.86	9.06 psia	78°F
*10% Mesh int	7	4	0.56	5.86 psia	75°F

*No pressure data obtained

TABLE IV

Pressure Coefficients at $X/D_B = 6$
($M_\infty \doteq 3.0$, $Re/ft \doteq 2.12 \times 10^6$)

Tap No	5% mesh		
	int	ext	net
1	.854	.219	.635
2	1.100	.011	1.089
3	1.100	-.045	1.145
4	1.080	-.067	1.147
5	1.056	-.068	1.144
6	.990	-.071	1.061
7	1.169	-.069	1.238
8	1.192	-.066	1.258
9	1.134	-.065	1.199
10	1.134	-.015	1.149
11	1.012	.205	.807
12	.862	.362	.500

Tap No	5% grid		
	int	ext	net
1	.875	.300	.575
2	1.145	.041	1.104
3	1.107	-.028	1.135
4	1.000	-.046	1.046
5	1.044	-.047	1.091
6	1.212	-.050	1.262
7	1.208	-.047	1.255
8	1.171	-.040	1.211
9	1.139	-.034	1.173
10	1.119	.024	1.095
11	.992	.238	.754
12	.783	.438	.345

Tap No	10% mesh		
	int	ext	net
1	.865	.441	.424
2	1.154	.035	1.119
3	1.153	-.027	1.180
4	1.098	-.042	1.140
5	1.017	-.053	1.170
6	.978	-.052	1.030
7	1.334	-.070	1.404
8	1.302	-.039	1.341
9	1.342	-.039	1.381
10	1.280	.040	1.240
11	1.099	.286	.813
12	.849	.396	.453

Tap No	10% grid		
	int	ext	net
1	.969	.445	.524
2	1.144	.091	1.053
3	1.143	-.006	1.149
4	1.008	-.011	1.019
5	.913	-.025	.938
6	1.121	-.023	1.144
7	1.234	-.025	1.259
8	1.277	-.008	1.285
9	1.174	.006	1.168
10	1.257	.070	1.187
11	1.086	.239	.847
12	.826	.283	.543

Tap No	15% mesh		
	int	ext	net
1	.723	.774	-.051
2	1.104	.026	1.078
3	1.101	-.060	1.161
4	.877	-.061	.738
5	.913	-.074	.987
6	1.047	-.081	1.128
7	.974	-.074	1.048
8	1.142	-.061	1.203
9	1.256	-.042	1.298
10	1.188	.044	1.144
11	.980	.345	.635
12	.738	.724	.014

Tap No	15% grid		
	int	ext	net
1	.840	.550	.290
2	1.193	.045	1.148
3	1.266	-.024	1.290
4	1.254	-.024	1.278
5	1.198	-.044	1.242
6	1.221	-.037	1.258
7	1.152	-.044	1.196
8	1.212	-.028	1.240
9	1.244	-.017	1.261
10	1.256	.011	1.245
11	1.016	.277	.739
12	.865	.660	.205

TABLE V

Pressure Coefficients at $X/D_B = 7$
($M_\infty \doteq 3.0$, $Re/ft \doteq 2.12 \times 10^6$)

Tap No	5% mesh		
	int	ext	net
1	.828	.278	.550
2	1.091	.026	1.065
3	1.100	-.038	1.138
4	1.145	-.059	1.204
5	1.094	-.058	1.152
6	1.054	-.062	1.116
7	1.112	-.059	1.171
8	1.114	-.054	1.168
9	1.072	-.053	1.125
10	1.117	.002	1.115
11	1.019	.186	.833
12	.840	.268	.572

Tap No	5% mesh		
	int	ext	net
1	.836	.253	.583
2	1.121	.010	1.111
3	1.083	-.050	1.133
4	.949	-.065	1.014
5	.990	-.067	1.057
6	1.191	-.068	1.259
7	1.192	-.067	1.259
8	1.160	-.063	1.223
9	1.126	-.058	1.184
10	1.108	-.007	1.115
11	.981	.195	.786
12	.780	.375	.405

Tap No	10% mesh		
	int	ext	net
1	.814	.419	.395
2	1.266	.037	1.229
3	1.262	-.025	1.287
4	1.283	-.039	1.322
5	1.162	-.050	1.212
6	1.103	-.047	1.150
7	1.055	-.066	1.121
8	1.124	-.034	1.158
9	1.208	-.033	1.241
10	1.216	-.037	1.253
11	1.074	.273	.801
12	.838	.352	.486

Tap No	10% grid		
	int	ext	net
1	.955	.406	.549
2	1.131	.083	1.048
3	1.225	-.021	1.246
4	.966	-.026	.992
5	.931	-.042	.973
6	1.095	-.038	1.133
7	1.229	-.039	1.268
8	.716	-.023	.739
9	1.189	-.009	1.198
10	1.273	.052	1.221
11	1.097	.202	.895
12	.836	.239	.597

Tap No	15% mesh		
	int	ext	net
1	.556	.851	.295
2	1.036	.044	.992
3	1.070	-.038	1.108
4	.818	-.036	.854
5	.860	-.049	.909
6	.971	-.058	1.029
7	.824	-.049	.873
8	1.035	-.037	1.072
9	1.158	-.018	1.176
10	1.022	.070	.952
11	.811	.380	.431
12	.616	.787	.171

Tap No	15% mesh		
	int*	ext	net
1	.781	.596	.185
2	1.051	.055	.996
3	1.124	-.026	1.150
4	1.126	-.026	1.152
5	1.074	-.048	1.122
6	1.125	-.045	1.170
7	1.135	-.046	1.181
8	1.156	-.032	1.188
9	1.139	-.021	1.160
10	1.159	.008	1.151
11	.969	.288	.681
12	.792	.694	.098

*Average of 3

TABLE VI

Pressure Coefficients at $X/D_B = 8$
($M_\infty \doteq 3.0$, $Re/ft \doteq 2.12 \times 10^6$)

Tap No	5% mesh		
	int	ext	net
1	.760	.284	.476
2	1.087	.011	1.076
3	1.084	-.053	1.137
4	1.044	-.071	1.115
5	.994	-.069	1.063
6	.960	-.072	1.032
7	1.093	-.069	1.162
8	1.144	-.067	1.211
9	1.071	-.066	1.137
10	1.130	-.016	1.146
11	.984	.167	.817
12	.810	.284	.526

Tap No	5% grid		
	int	ext	net
1	.791	.384	.407
2	1.106	.045	1.061
3	1.050	-.007	1.057
4	.917	-.026	.943
5	.958	-.027	.985
6	1.162	-.029	1.191
7	1.153	-.024	1.177
8	1.139	-.020	1.159
9	1.115	-.011	1.126
10	1.104	.027	1.077
11	.965	.202	.763
12	.746	.317	.429

Tap No	10% mesh		
	int	ext	net
1	.813	.412	.401
2	1.182	.027	1.155
3	1.240	-.028	1.268
4	1.181	-.041	1.222
5	1.077	-.052	1.129
6	1.086	-.050	1.136
7	1.069	-.068	1.137
8	1.089	-.038	1.127
9	1.165	-.038	1.203
10	1.168	.033	1.135
11	1.033	.281	.752
12	.844	.428	.416

Tap No	10% grid		
	int	ext	net
1	.895	.443	.452
2	1.122	.079	1.043
3	1.114	-.022	1.136
4	.978	-.026	1.004
5	.920	-.042	.962
6	1.062	-.038	1.100
7	1.132	-.039	1.171
8	1.200	-.024	1.224
9	1.155	-.010	1.165
10	1.217	.051	1.166
11	1.051	.201	.850
12	.819	.265	.554

Tap No	15% mesh		
	int	ext	net
1	.569	.698	-.124
2	.996	.014	.982
3	1.014	-.058	1.072
4	.803	-.064	.867
5	.862	-.074	.936
6	.987	-.077	1.064
7	.812	-.076	.888
8	.951	-.066	1.017
9	1.059	-.047	1.106
10	.990	.030	.960
11	.779	.344	.435
12	.591	.760	-.169

Tap No	15% grid		
	int	ext	net
1	.693	.577	.116
2	.948	.047	.901
3	1.029	-.017	1.046
4	1.027	-.017	1.044
5	.967	-.036	1.003
6	1.027	-.029	1.056
7	1.063	-.037	1.100
8	1.107	-.019	1.126
9	1.061	-.006	1.067
10	1.085	.019	1.066
11	.903	.332	.571
12	.721	.644	.077

TABLE VII

Pressure Coefficients at $X/D_B = 9$
($M_\infty \doteq 3.0$, $Re/ft \doteq 2.12 \times 10^6$)

Tap No	5% mesh		
	int	ext	net
1	.734	.231	.503
2	1.055	.010	1.045
3	1.041	-.045	1.086
4	1.019	-.065	1.084
5	.960	-.064	1.024
6	.927	-.066	.993
7	1.039	-.064	1.103
8	1.121	-.060	1.181
9	1.033	-.060	1.093
10	1.119	-.011	1.130
11	.959	.163	.796
12	.783	.298	.485

Tap No	5% grid		
	int	ext	net
1	.753	.208	.545
2	1.084	-.002	1.086
3	1.041	-.049	1.090
4	.937	-.060	.997
5	.964	-.061	1.025
6	1.147	-.062	1.209
7	1.104	-.062	1.166
8	1.088	-.060	1.148
9	1.078	-.056	1.134
10	1.085	-.011	1.096
11	.945	.186	.759
12	.735	.437	.298

Tap No	10% mesh		
	int	ext	net
1	.663	.453	.210
2	1.093	.039	1.054
3	1.044	-.014	1.058
4	.986	-.024	1.010
5	.850	-.035	.885
6	.845	-.033	.878
7	1.111	-.051	1.162
8	1.174	-.022	1.196
9	1.262	-.022	1.284
10	1.206	.030	1.176
11	.990	.200	.790
12	.782	.295	.487

Tap No	10% grid		
	int	ext	net
1	.850	.491	.359
2	1.090	.080	1.010
3	1.065	-.020	1.085
4	.904	-.024	.928
5	.854	-.040	.894
6	.985	-.034	1.019
7	1.088	-.037	1.125
8	.675	-.018	.693
9	1.149	-.005	1.154
10	1.166	.259	.907
11	.994	.148	.846
12	.789	.175	.614

Tap No	15% mesh		
	int	ext	net
1	.546	.680	-.134
2	1.003	.022	.981
3	1.061	-.050	1.111
4	.839	-.052	.891
5	.870	-.065	.935
6	.964	-.070	1.034
7	.815	-.063	.878
8	.997	-.055	1.052
9	1.120	-.033	1.153
10	1.001	.045	.956
11	.786	.320	.466
12	.614	.709	-.095

Tap No	15% grid		
	int	ext	net
1	.694	.542	.152
2	.947	.033	.914
3	.995	-.032	1.027
4	.987	-.032	1.019
5	.921	-.050	.971
6	1.002	-.052	1.054
7	1.125	-.049	1.174
8	1.180	-.035	1.115
9	1.131	-.024	1.155
10	1.133	.000	1.133
11	.911	.255	.656
12	.727	.563	.164

TABLE VIII

Pressure Coefficients at $X/D_B = 11$
($M_\infty \doteq 3.0$, $Re/ft \doteq 2.12 \times 10^6$)

Tap No	5% mesh		
	int	ext	net
1	.703	.237	.466
2	.986	.003	.983
3	.981	-.048	1.029
4	1.007	-.066	1.073
5	.945	-.066	1.011
6	.928	-.069	.997
7	.988	-.068	1.056
8	1.036	-.062	1.098
9	.950	-.061	1.011
10	1.046	-.020	1.066
11	.895	.135	.760
12	.734	.243	.491

Tap No	5% grid		
	int	ext	net
1	.757	.282	.475
2	1.083	.005	1.078
3	1.052	-.042	1.094
4	1.025	-.054	1.079
5	1.019	-.054	1.073
6	1.134	-.054	1.188
7	1.081	-.054	1.135
8	1.038	-.052	1.090
9	1.051	-.047	1.098
10	1.101	-.008	1.109
11	.982	.157	.825
12	.735	.309	.426

Tap No	10% mesh		
	int	ext	net
1	.639	.416	.223
2	1.060	.046	1.014
3	1.000	.001	.999
4	.928	-.011	.939
5	.778	-.021	.799
6	.789	-.017	.806
7	1.086	-.039	1.125
8	1.158	-.007	1.165
9	1.235	-.007	1.242
10	1.190	.036	1.154
11	.964	.177	.787
12	.749	.262	.487

Tap No	10% grid		
	int	ext	net
1	.816	.440	.376
2	1.023	.071	.952
3	.987	-.023	1.010
4	.833	-.026	.859
5	.802	-.040	.842
6	.950	BAD	
7	1.065	-.034	1.099
8	1.245	-.019	1.264
9	1.108	-.007	1.115
10	1.136	BAD	
11	.963	.132	.831
12	.747	.158	.589

Tap No	15% mesh		
	int	ext	net
1	.628	.627	.001
2	1.129	.017	1.112
3	1.203	-.050	1.253
4	.996	-.051	1.047
5	1.023	-.061	1.084
6	1.069	-.066	1.135
7	.751	-.054	.805
8	.850	-.052	.902
9	1.006	-.031	1.037
10	1.009	.038	.971
11	.864	.310	.554
12	.630	.621	.009

Tap No	15% grid		
	int	ext	net
1	.672	.405	.267
2	.926	.028	.898
3	.935	-.021	.956
4	.910	-.023	.933
5	.823	-.040	.863
6	.952	-.045	.997
7	1.175	-.037	1.208
8	1.217	-.022	1.239
9	1.173	-.017	1.190
10	1.162	.003	1.159
11	.892	.209	.683
12	.695	.468	.227

TABLE IX

Pressure Coefficients at $X/D_B = \infty$
($M_\infty \doteq 3.0$, Re/ft $\doteq 2.12 \times 10^6$)

Tap No	5% mesh		
	int	ext	net
1	.700	.511	.189
2	1.100	-.001	1.101
3	1.128	-.078	1.206
4	1.190	-.094	1.284
5	.993	-.095	1.088
6	1.008	-.097	1.105
7	.953	-.097	1.050
8	.998	-.091	1.089
9	.972	-.090	1.062
10	1.085	-.041	1.126
11	.939	.210	.729
12	.786	.542	.244

Tap No	5% grid		
	int	ext	net
1	.625	.711	-.086
2	1.214	.020	1.194
3	1.182	-.068	1.250
4	1.182	-.081	1.263
5	1.041	-.083	1.124
6	1.096	-.083	1.179
7	.994	-.083	1.077
8	.987	-.079	1.066
9	1.013	-.073	1.086
10	1.101	-.004	1.105
11	.939	.271	.668
12	.719	.579	.140

Tap No	10% mesh		
	int	ext	net
1	.789	.482	.307
2	1.262	.034	1.228
3	1.227	-.025	1.252
4	1.254	-.041	1.295
5	1.168	-.049	1.217
6	1.116	-.049	1.165
7	1.097	-.073	1.170
8	1.176	-.038	1.214
9	1.249	-.037	1.286
10	1.263	.037	1.226
11	1.048	.340	.708
12	.804	.652	.152

Tap No	10% grid		
	int	ext	net
1	.756	.482	.274
2	1.227	.064	1.163
3	1.277	-.049	1.326
4	1.194	-.056	1.250
5	1.115	-.070	1.185
6	1.083	-.063	1.146
7	1.020	-.077	1.097
8	1.216	-.059	1.275
9	1.097	-.047	1.144
10	1.262	.229	1.033
11	1.017	.288	.729
12	.770	.536	.234

Tap No	15% mesh		
	int	ext	net
1	.632	.667	-.035
2	1.040	.039	1.001
3	1.075	-.034	1.109
4	.830	-.032	.862
5	.870	-.045	.915
6	.963	-.059	1.022
7	.716	-.049	.765
8	.884	-.036	.920
9	1.072	-.014	1.086
10	.969	.059	.910
11	.814	.363	.451
12	.585	.740	-.155

Tap No	15% grid		
	int	ext	net
1	.770	.566	.204
2	1.202	-.015	1.217
3	1.335	-.041	1.376
4	1.343	-.043	1.386
5	1.250	-.058	1.308
6	1.170	-.058	1.228
7	1.042	-.057	1.099
8	1.104	-.046	1.150
9	1.063	.028	1.035
10	1.153	.015	1.138
11	.902	.270	.632
12	.865	.576	.289

TABLE X

Internal Pressure Coefficients for 10% Mesh and 10% Grid Models at X/D_B = 6 and 8
($M_\infty \doteq 3.0$, Re/ft $\doteq 1.10 \times 10^6$)

Tap No	10% Mesh X/D_B = 6
1	.754
2	.954
3	.961
4	.946
5	.935
6	.919
7	1.101
8	1.075
9	1.101
10	1.031
11	.884
12	.712

Tap No	10% Grid X/D_B = 6
1	.953
2	1.180
3	1.200
4	1.128
5	1.125
6	1.212
7	1.235
8	1.321
9	1.194
10	1.246
11	1.103
12	.915

Tap No	10% Mesh X/D_B = 8
1	.745
2	.961
3	.949
4	.951
5	.924
6	.980
7	1.056
8	1.065
9	1.124
10	1.138
11	.925
12	.754

Tap No	10% Grid X/D_B = 8
1	.725
2	.954
3	.989
4	.926
5	.923
6	.997
7	.975
8	1.011
9	.932
10	.988
11	.866
12	.691

TABLE XI

Pressure Coefficients for 10% Mesh and 10% Grid Models at X/D_B = 5, 6, and 7 ($M_\infty \doteq 4.0$, Re/ft $\doteq 2.99 \times 10^6$)

Tap No	10% Mesh, X/D_B = 5		
	int	ext	net
1	.103	.548	-.445
2	.133	.046	.087
3	.151	.140	.011
4	.211	.028	.183
5	.213	.024	.189
6	.182	.026	.156
7	.134	.004	.130
8	.125	.028	.097
9	.132	.030	.102
10	.137	.092	.045
11	.137	.092	.045
12	.123	.075	.048

Tap No	10% Mesh, X/D_B = 6		
	int	ext	net
1	.598	.705	-.107
2	1.160	.042	1.118
3	1.137	.014	1.123
4	1.501	.004	1.497
5	1.450	.000	1.450
6	1.283	.002	1.281
7	.671	-.014	.685
8	.884	.003	.881
9	1.072	.006	1.066
10	1.215	.043	1.172
11	1.060	.010	1.050
12	.779	.138	.641

Tap No	10% Grid, X/D_B = 6		
	int	ext	net
1	.534	.487	.047
2	1.100	.038	1.062
3	1.182	.007	1.175
4	1.273	.003	1.270
5	1.276	-.003	1.279
6	1.191	.000	1.191
7	.718	.002	.716
8	.802	.002	.800
9	.976	.010	.966
10	1.114	.038	1.076
11	1.020	.145	.875
12	.782	.120	.662

Tap No	10% Mesh, X/D_B = 7		
	int	ext	net
1	.691	.770	-.079
2	1.277	.068	1.209
3	1.250	.041	1.209
4	1.557	.032	1.525
5	1.479	.027	1.452
6	1.414	.029	1.385
7	.714	.011	.703
8	.860	.028	.832
9	1.054	.033	1.021
10	1.225	.084	1.141
11	1.009	.141	.851
12	.720	.204	.516

Tap No	10% Grid, X/D_B = 7		
	int	ext	net
1	.543	.535	.008
2	1.246	.063	1.183
3	1.323	.016	1.307
4	1.239	.012	1.227
5	1.245	.004	1.241
6	1.208	.006	1.202
7	.815	.008	.807
8	.785	.008	.777
9	1.027	.020	1.007
10	1.229	.062	1.167
11	1.093	.003	1.090
12	.794	.149	.645

TABLE XII

Pressure Coefficients for 10% Mesh and 10% Grid Models at X/D_B = 8, 9 and ∞ ($M_\infty \doteq 4.0$, Re/ft $\doteq 2.99 \times 10^6$)

Tap No	10% Mesh, X/D_B = 8		
	int	ext	net
1	.648	.685	-.037
2	1.225	.048	1.177
3	1.208	.020	1.188
4	1.448	.011	1.437
5	1.318	.005	1.313
6	1.282	.006	1.276
7	.680	-.010	.690
8	.822	.007	.815
9	1.006	.011	.995
10	1.163	.060	1.103
11	.976	.268	.708
12	.694	.190	.504

Tap No	10% Grid, X/D_B = 8		
	int	ext	net
1	.532	.500	.032
2	1.025	.058	.967
3	1.106	.013	1.093
4	1.082	.010	1.072
5	.995	.002	.993
6	.995	.004	.991
7	.720	.006	.714
8	.651	.006	.545
9	.814	.018	.796
10	.966	.058	.908
11	.888	.226	.662
12	.652	.144	.508

Tap No	10% Mesh, X/D_B = 9		
	int	ext	net
1	.518	.638	-.120
2	.973	.040	.933
3	1.002	.015	.987
4	1.186	.006	1.180
5	1.103	.004	1.099
6	1.057	.004	1.053
7	.576	-.008	.584
8	.622	.007	.615
9	.782	.010	.772
10	.912	.050	.862
11	.778	.230	.548
12	.541	.264	.277

Tap No	10% Grid, X/D_B = 9		
	int	ext	net
1	.561	.496	.065
2	1.071	.060	1.011
3	1.135	.017	1.118
4	1.142	.014	1.128
5	1.032	.003	1.029
6	1.078	.006	1.072
7	.774	.006	.768
8	.693	.007	.686
9	.810	.021	.789
10	.964	.063	.901
11	.862	.230	.632
12	.526	.155	.371

Tap No	10% Mesh, $X/D_B = \infty$		
	int	ext	net
1	.473	.516	-.043
2	.852	.037	.815
3	.855	.016	.839
4	.977	.004	.973
5	.863	.004	.859
6	.826	.005	.821
7	.794	-.009	.803
8	.930	.007	.923
9	1.014	.010	1.004
10	.917	.044	.873
11	.602	.219	.383
12	.424	.715	-.291

Tap No	10% Grid, $X/D_B = \infty$		
	int	ext	net
1	.301	.477	-.176
2	.725	.049	.676
3	.843	.006	.837
4	.809	.001	.808
5	.634	.001	.633
6	.661	.001	.660
7	.597	.002	.595
8	.803	.001	.802
9	.714	.015	.699
10	.758	.044	.714
11	.457	.221	.236
12	.280	.496	-.216

TABLE XIII

Internal Pressure Coefficients for 10% Mesh and 10% Grid Models at X/D_B = 6, 7, 8, and ∞
($M_\infty \doteq 4.0$, Re/ft $\doteq 1.36 \times 10^6$)

Tap No	10% Mesh $X/D_B = 6$
1	.205
2	.242
3	.247
4	.255
5	.233
6	.245
7	.250
8	.245
9	.250
10	.238
11	.225
12	.216

Tap No	10% Grid $X/D_B = 6$
1	.238
2	.389
3	.425
4	.358
5	.369
6	.451
7	.346
8	.317
9	.310
10	.312
11	.324
12	.284

Tap No	10% Mesh $X/D_B = 7$
1	.396
2	.642
3	.605
4	.673
5	.768
6	.779
7	.593
8	.534
9	.559
10	.557
11	.460
12	.369

Tap No	10% Grid $X/D_B = 7$
1	.371
2	.729
3	.810
4	.624
5	.653
6	.810
7	.581
8	.543
9	.519
10	.543
11	.519
12	.457

Tap No	10% Mesh $X/D_B = 8$
1	.428
2	.684
3	.636
4	.724
5	.845
6	.913
7	.674
8	.587
9	.622
10	.618
11	.514
12	.417

Tap No	10% Grid $X/D_B = 8$
1	.364
2	.725
3	.806
4	.632
5	.685
6	.918
7	.641
8	.589
9	.549
10	.592
11	.534
12	.441

Tap No	10% Mesh $X/D_B = \infty$
1	.314
2	.541
3	.586
4	.679
5	.635
6	.642
7	.590
8	.787
9	.902
10	.766
11	.370
12	.276

Tap No	10% Grid $X/D_B = \infty$
1	.268
2	.450
3	.563
4	.567
5	.511
6	.535
7	.460
8	.623
9	.652
10	.584
11	.326
12	.221

APPENDIX I

In this test program, the mass flow through a grid-roofed Hyperflo parachute model has been equated to that through a mesh-roofed model. Because the geometric porosity of a mesh-like material is difficult to measure, data from a previous study of textile Hyperflo parachutes (Ref 2) have been used. The lower edge of the porous region for all grid-type canopies has been fixed at the same point as the lower mesh-edge of the mesh-covered canopies of maximum geometric porosity.

CALCULATION OF CANOPY PARAMETERS

A. General Methods

1. Mesh-roofed models

If the upper portion of a parachute canopy consists of n porous gores of total area A_m separated by n non-porous support ribbons of width B_R, the total area from the roof center to the lower mesh edge is

$$A_1 = A_m + nB_R\ell_3 + A_2 ,$$

where ℓ_3 is the arc length along a support ribbon from the edge of the solid central polygon of area A_2 to the lower mesh edge (Fig 47). Since the uppermost region of the canopy roof is not strongly curved, the area of the central polygon may be approximated by its planar equivalent:

$$A_2 \simeq \frac{nB_R^2}{4} \cot \frac{\pi}{n} .$$

Using $\ell_1 = \ell_2 + \ell_3$ (Fig 47), where $\ell_2 \simeq \frac{B_R}{2} \cot \frac{\pi}{n}$, the total area from roof center to lower mesh edge is:

$$A_1 \simeq A_m - \frac{nB_R^2}{4} \cot \frac{\pi}{n} + nB_R\ell_1 . \qquad (1)$$

If A_m, which is a function of the desired geometric porosity of the canopy is known, then Eqn 1 gives A_1 as a straight line when plotted versus ℓ_1.

By treating the surface of any parachute model which is a body of revolution as the result of a sequence of conical segments, the surface area of any portion of the model may be found by a simple numerical integration, while

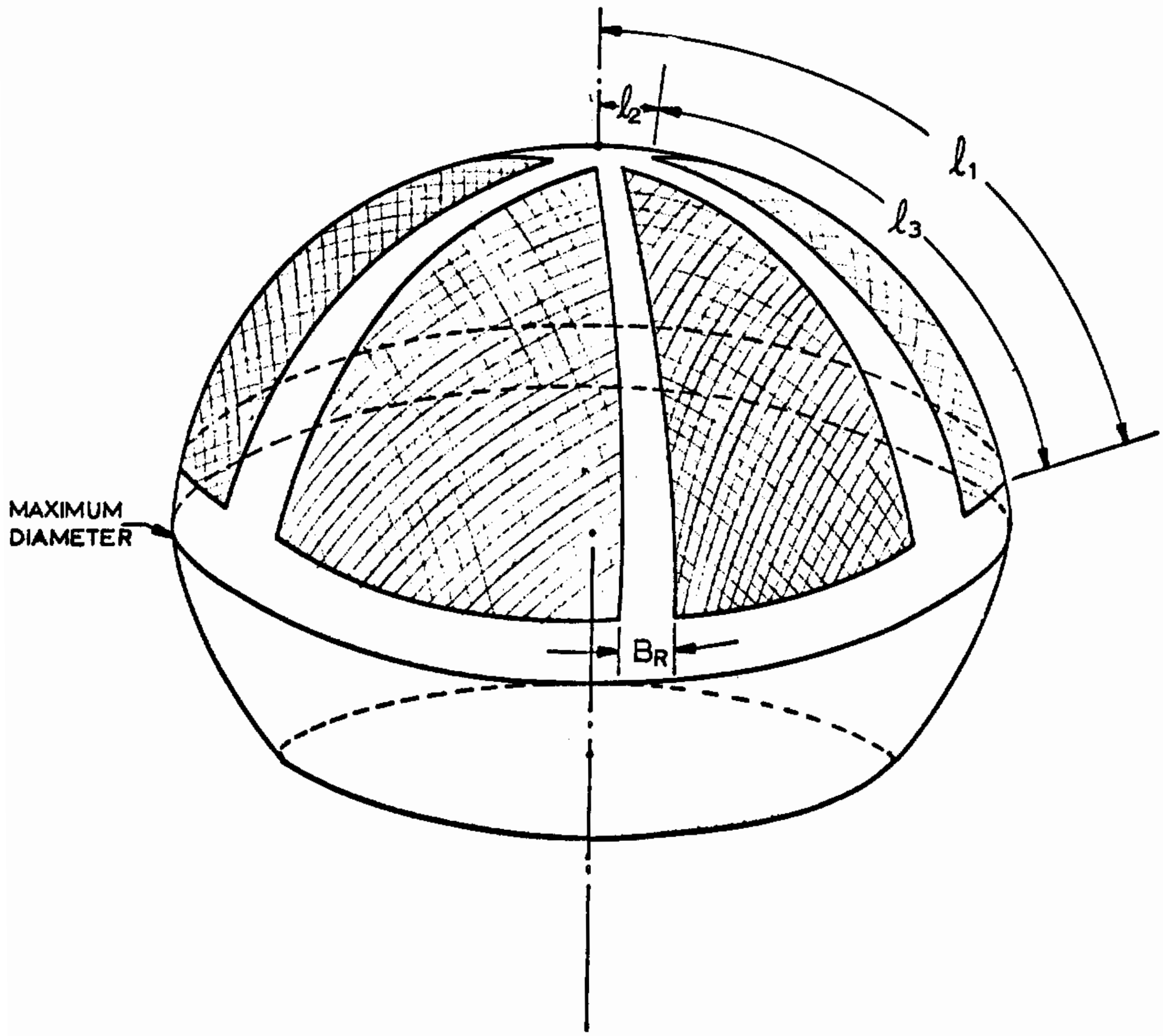

Fig 47. Scheme of Mesh-roofed Hyperflo Canopy Model

the arc length along the surface may be measured directly from the design profile. Hence, the total surface area S_o may be found, and the area A_1 from the roof center to any point on the canopy may be tabulated as a function of ℓ_1, the arc length along the canopy.

Intersections of the tabulated plot of A_1 versus ℓ_1 for the design profile and the lines given by Eqn 1 provide the desired total porous area A_m.

2. Grid-roofed models

If a circle of radius r_G is covered with evenly spaced solid ribbons of width B_R a distance ℓ_R apart, with n_R ribbons to the left or right of center (Fig 48), the area of the jth such ribbon may be approximated by

$$A_j \simeq 2r_G B_R \sin\theta_j = 2r_G B_R \sqrt{1 - \cos^2\theta_j} \quad .$$

From Fig 48

$$\frac{r_G}{n_R} = \ell_R + B_R \qquad (2)$$

and

$$r_G \cos\theta_j = (j - \tfrac{1}{2})(\ell_R + B_R) \quad .$$

Hence

$$A_j \simeq 2r_G B_R \sqrt{1 - \left(\frac{2j - 1}{2n_R}\right)^2} \quad .$$

The total area covered by such ribbons when placed to form a grid is then

$$A_R \simeq 4\left[2r_G B_R \sum_{j=1}^{n_R} \sqrt{1 - \left(\frac{2j - 1}{2n_R}\right)^2}\right] - A_{overlap} \quad .$$

The overlap area in each quadrant may be estimated by multiplying the overlap area within a square of edge r_G by the ratio of quadrant area to the square's area, so that

$$A_{overlap} = 4\left[n_R^2 B_R^2 \cdot \frac{\frac{\pi r_G^2}{4}}{r_G^2}\right] = n_R^2 B_R^2 \pi \quad .$$

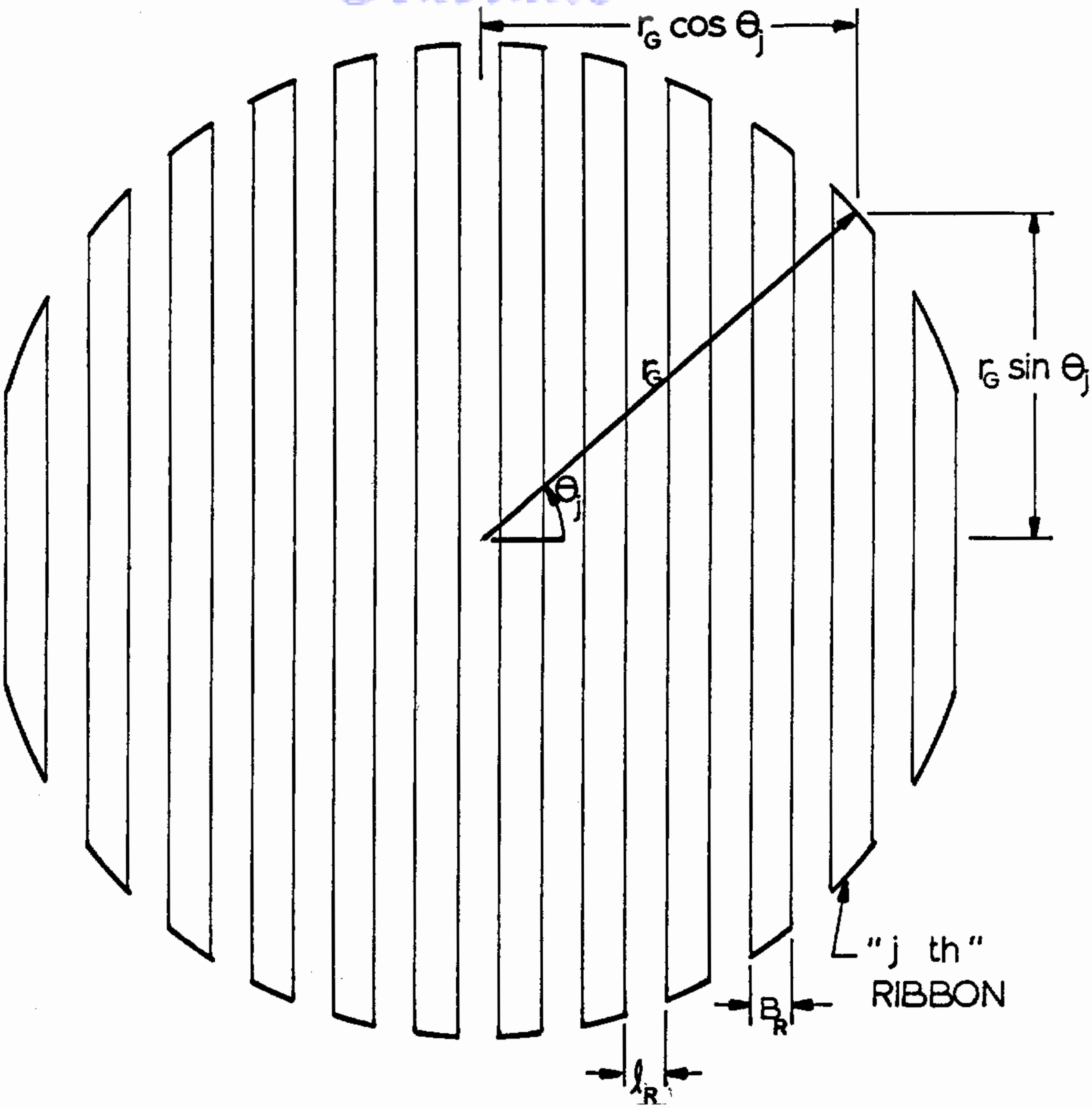

$$r_G = \frac{\ell_R}{2} + (n_R - 1)\ell_R + n_R B_R + \frac{\ell_R}{2} = n_R(\ell_R + B_R)$$

$$r_G \cos\theta_j = \frac{\ell_R}{2} + (j - 1)\ell_R + (j - 1)B_R + \frac{B_R}{2} = (j - \tfrac{1}{2})(\ell_R + B_R)$$

n_R = total number of ribbons to right or left of center;
here, $n_R = 6$.

Fig 48. Geometric Relations on Circle Covered by Solid Ribbons of Width B_R and Spacing ℓ_R

Therefore

$$A_R \simeq 8r_G B_R \sum_{j=1}^{n_R} \sqrt{1 - \left(\frac{2j-1}{2n_R}\right)^2} - \pi n_R^2 B_R^2 \quad . \qquad (3)$$

Since the geometric porosity of the grid thus created is

$$\lambda_{rg} = \frac{\pi r_G^2 - A_R}{\pi r_G^2}$$

use of Eqns 2 and 3 gives:

$$\left[2\pi r_G^2 - \lambda_{rg}\pi r_G^2\right] \simeq \left[2\pi r_G \ell_R n_R - \pi \ell_R^2 n_R^2\right]$$

$$+ \left[\frac{8r_G^2}{n_R} - 8r_G \ell_R\right] \sum_{j=1}^{n_R} \sqrt{1 - \left(\frac{2j-1}{2n_R}\right)^2} \qquad (4)$$

Both sides of this equation may be plotted as functions of n_R; given r_G, ℓ_R and λ_{rg}, the point of intersection gives n_R, the number of ribbons to the left or right of center required for the given λ_{rg}. Equation 2 then gives the necessary ribbon width B_R.

B. Equating Mass Flow

The ideal mass flow through an open area A_λ is given by $\dot{m}_i = \rho v A$. Since the flow coefficient K is defined as the ratio of actual mass flow to ideal mass flow, then $\dot{m}_a = \rho v K A$. If the flow through the orifices of both a ribbon grid and a porous mesh is assumed supercritical, then the condition for equal mass flow through parachute canopies composed of these materials is

$$(KA_\lambda)_{rg} = (KA_\lambda)_m \quad ,$$

or, in terms of the areas and geometric porosities of the respective materials,

$$A_{rg}(K\lambda)_{rg} = A_m(K\lambda)_m \quad .$$

Since A_{rg} has been chosen equal to $A_{1_{max}}$, the canopy surface area above the lower mesh edge for the most porous mesh-roofed model, then

$$\lambda_{rg} = \left[\frac{1}{A_{1_{max}}} \frac{(K\lambda)_m}{K_{rg}} \right] A_m \qquad (5)$$

When A_m is known, Eqns 2, 4, and 5 supply the necessary parameters for the grid-roofed Hyperflo models.

If λ_m is the geometric porosity of the mesh used, and S_o is the total canopy surface area,

$$A_m = \frac{\lambda_g}{\lambda_m} S_o \ ,$$

where λ_g is the geometric porosity of the mesh-roofed model. Then λ_{rg} is given by Eqn 5 in terms of a ratio of flow coefficients.

Experimentally, only the product $K\lambda$ is determined (Appendix II), so that reliable values for K require accurate knowledge of λ, the geometric porosity of the material involved. In the case of the ribbon grids, λ_{rg} may be evaluated quite easily, and so K_{rg}, the flow coefficient for the grids, may be specified. However, in the case of fine mesh, the measurement of λ_m is difficult; for example, studies of a nickel-wire mesh carried out with a microscope and an optical comparator gave λ_m values in the range of 40% to 56%. In addition, the actual open area of a woven grid is somewhat larger than that indicated by a flat projection (Ref 3). Hence, K_m cannot be directly evaluated.

In an earlier study of Hyperflo parachutes (Ref 2), textile canopies which utilized perlon screen as the porous roof material were considered. The remaining portions of these canopies were constructed from heavy (300 lb/in.) nylon, and from neoprene-coated nylon. Models of 5%, 10%, and 15% geometric porosity were studied. If such models are scaled to the models of this test program by a total area ratio, then the roof area covered by perlon screen on the scaled canopies is

$$A_p = A_p^{II} \frac{S_o}{S_o^{II}} \ ,$$

where the superscript denotes the values on the original models (Ref 2). The mass flow through rigid wire mesh-roofed Hyperflo canopies may then be equated to that through such scaled perlon-roofed models, neglecting the porosity of the heavy-cloth regions:

$$A_m(K\lambda)_m \simeq A_p(K\lambda)_p \ .$$

Hence

$$A_m \simeq A_p^{II} \frac{S_o}{S_o^{II}} \frac{(K\lambda)_p}{(K\lambda)_m} \quad . \tag{6}$$

Equation 6 may be used in Eqns 1 and 5 to compute the parameters necessary for construction of the rigid Hyperflo models of matched mass flow.

To compute the geometric porosities of the mesh-type models thus constructed, note that

$$\lambda_g = \lambda_m \frac{A_m}{S_o} \simeq \frac{\lambda_p A_p^{II}}{S_o^{II}} \frac{K_p}{K_m} \simeq \lambda_g^{II} \frac{K_p}{K_m} \quad ,$$

neglecting the porosity of the heavy-cloth regions of the textile models. Although K_p/K_m cannot be directly evaluated, by choosing the wire mesh of the rigid models geometrically similar to the perlon screen of the textile models (59 wires of 0.0061 in. diameter/inch, for the wire; 64 strands of 0.0060 in. diameter/inch, for the perlon), the flow coefficients should be about equal, so that the rigid mesh-roofed Hyperflo models have geometric porosities of approximately 5%, 10%, and 15%.

For the grid-type models, the geometric porosity is

$$\lambda_g = \lambda_{rg} \frac{A_{1_{max}}}{S_o} = \frac{A_m}{S_o} \frac{(K\lambda)_m}{K_{rg}} \simeq \frac{A_p^{II}}{S_o^{II}} \frac{(K\lambda)_p}{K_{rg}} \quad .$$

The rigid grid-roofed Hyperflo models have geometric porosities of 5.05%, 10.9%, and 16.8%, compared to the nominal values of 5%, 10%, and 15%.

The results of the calculations are given in Tables XIV and XV.

TABLE XIV

Mesh-edge Coordinates for Hyperflo Models

APPROX. λ_g	ℓ_1/R_p	X_c/R_p	Y_c/R_p
5%	0.572	0.555	0.105
10%	0.803	0.753	0.221
15%	0.980	0.878	0.343

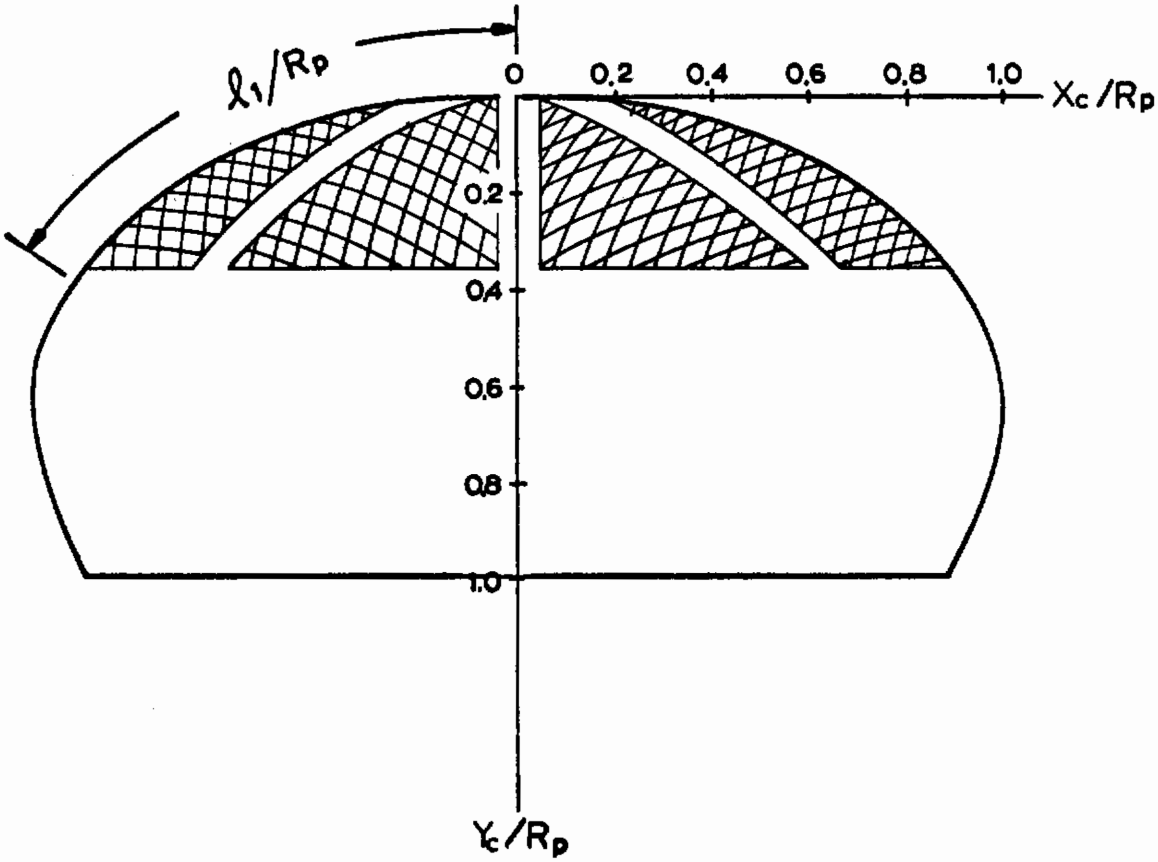

TABLE XV

Construction Parameters for Ribbon Grid Hyperflo Models

NOMINAL CANOPY GEOMETRIC POROSITY	B_R/ℓ_R	COMPUTED CANOPY GEOMETRIC POROSITY
5%	1.69	5.05%
10%	0.91	10.9%
15%	0.56	16.8%

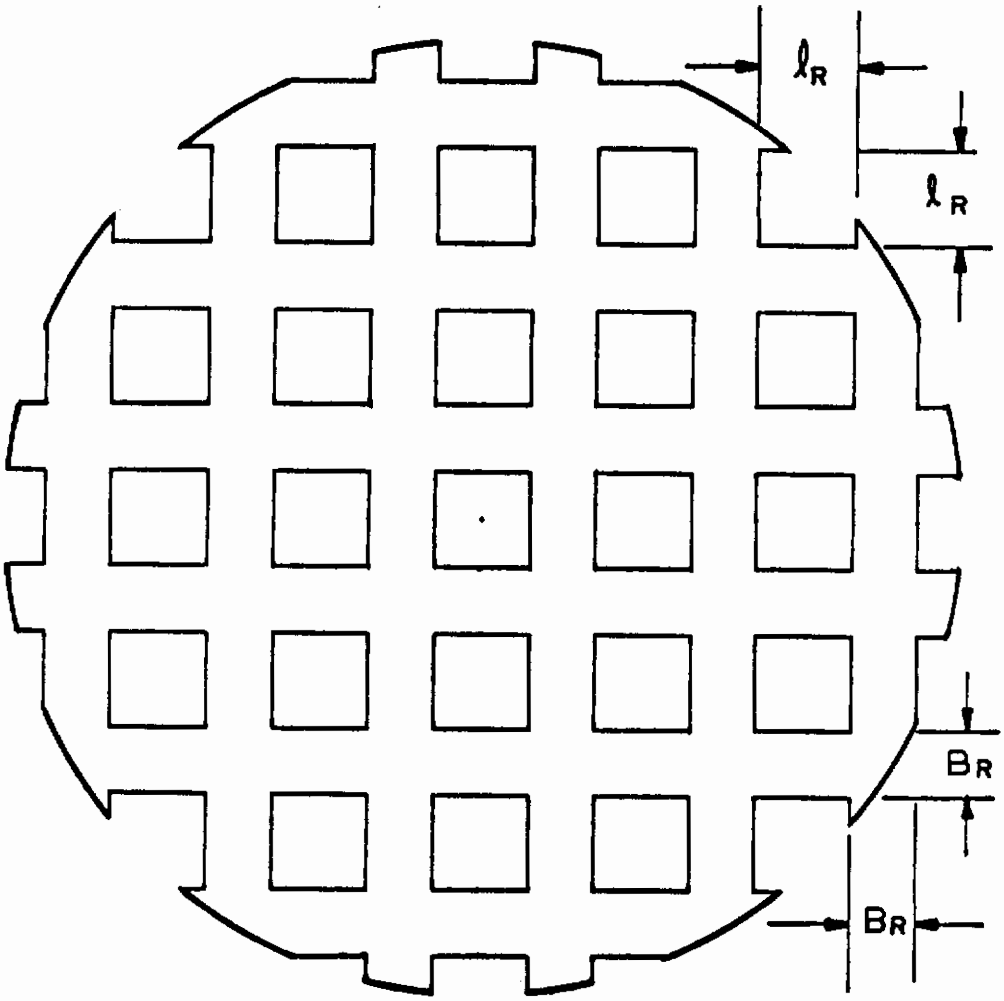

APPENDIX II

FLOW COEFFICIENT MEASUREMENT

To measure the flow coefficient K of a porous material, both the ideal and the actual mass flows must be determined.

The test apparatus (Fig 49) was constructed according to the ASME standards on flow measurement (Ref 4), and the actual mass flow $\dot{m}_a$ can be shown to be

$$\dot{m}_a = 0.806 \times 10^{-3} d^2 \, K \, Y \sqrt{\Delta p_{1-2} \gamma_a p_1} \quad \text{slugs/sec},$$

where d is measured in inches, Δp_{1-2} in inches of water, γ_a in lbs/ft3, and p_1 in psia. K and Y are obtained from Ref 4.

For supercritical flow through a porous region, the ideal mass flow is $\dot{m}_i = \rho^* a^* A_\lambda$, where A_λ is the open area of the sample, and ρ^* and a^* are the critical density and the speed of sound, respectively. Use of the ideal gas law gives

$$\dot{m}_i = \sqrt{\frac{\gamma}{RT^*}} \; p^* A_\lambda \quad .$$

In the notation of Fig 49, $p^* = 0.5283 p_3$, $T^* = 0.8333 T_3$, with $T_3 = 540°R$ as average value (Ref 5), and so

$$\dot{m}_i = 0.1025 p_3 A_\lambda \quad \text{slugs/sec},$$

with p_3 in psia and A_λ measured in ft^2.

Hence, the ratio of actual mass flow to ideal mass flow is

$$K = \frac{1}{\lambda} \; \frac{\dot{m}_a}{0.1025 p_3 A} \quad ,$$

where A is the total sample area in ft^2, and λ is its geometric porosity. It is clear that K can be determined only if λ is known. Therefore, because of the difficulty in obtaining an accurate measurement of the open area, the product $K\lambda$ was evaluated.

For conditions of supercritical flow, the average values of a large number of measurements gave $(K\lambda)_m = 0.464$ for the wire mesh used in this test program, while $(K\lambda)_p = 0.456$ for the perlon screen of the textile models studied in Ref 2.

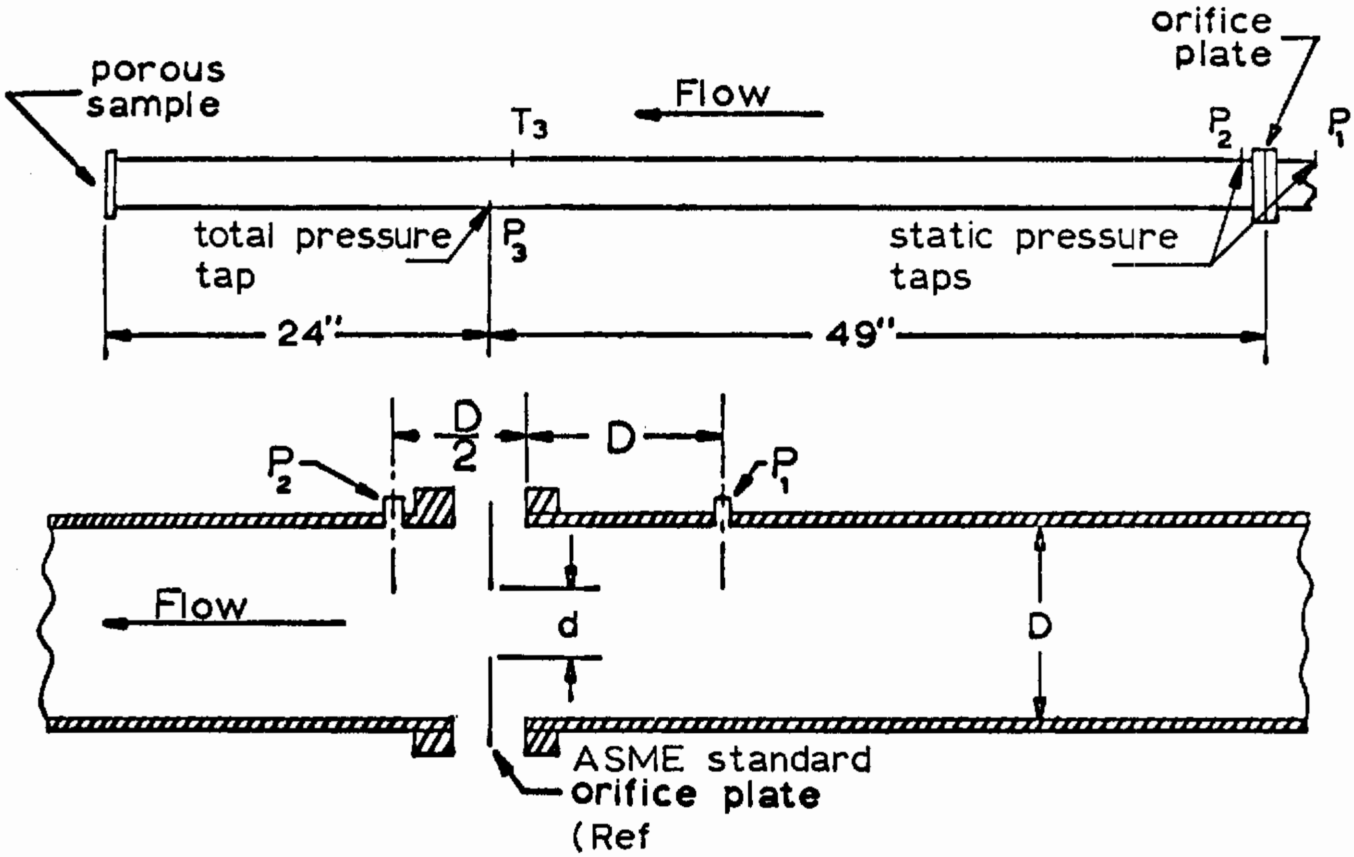

$$\dot{m}_a = 0.806 \times 10^{-3}\, d^2\, K Y \sqrt{\Delta P_{1-2}\, P_1\, \gamma_a} \quad \text{slugs/sec}$$

d = **orifice diameter** in inches

K = **ASME orifice coefficient** (Ref 4)

Y = **ASME expansion factor** (Ref 4)

ΔP_{1-2} = **pressure differential across orifice** in inches of H_2O

γ_a = **weight density** in lbs/ft^3 at T_1 and 29.92 in. of Hg.

Fig 49. Flow Coefficient Measurement Apparatus

In the case of the ribbon grids where measurements were relatively simple, the coefficient K was evaluated, and Fig 50 gives K_{rg} as a function of the solid ribbon width B_R for various ribbon spacings ℓ_R.

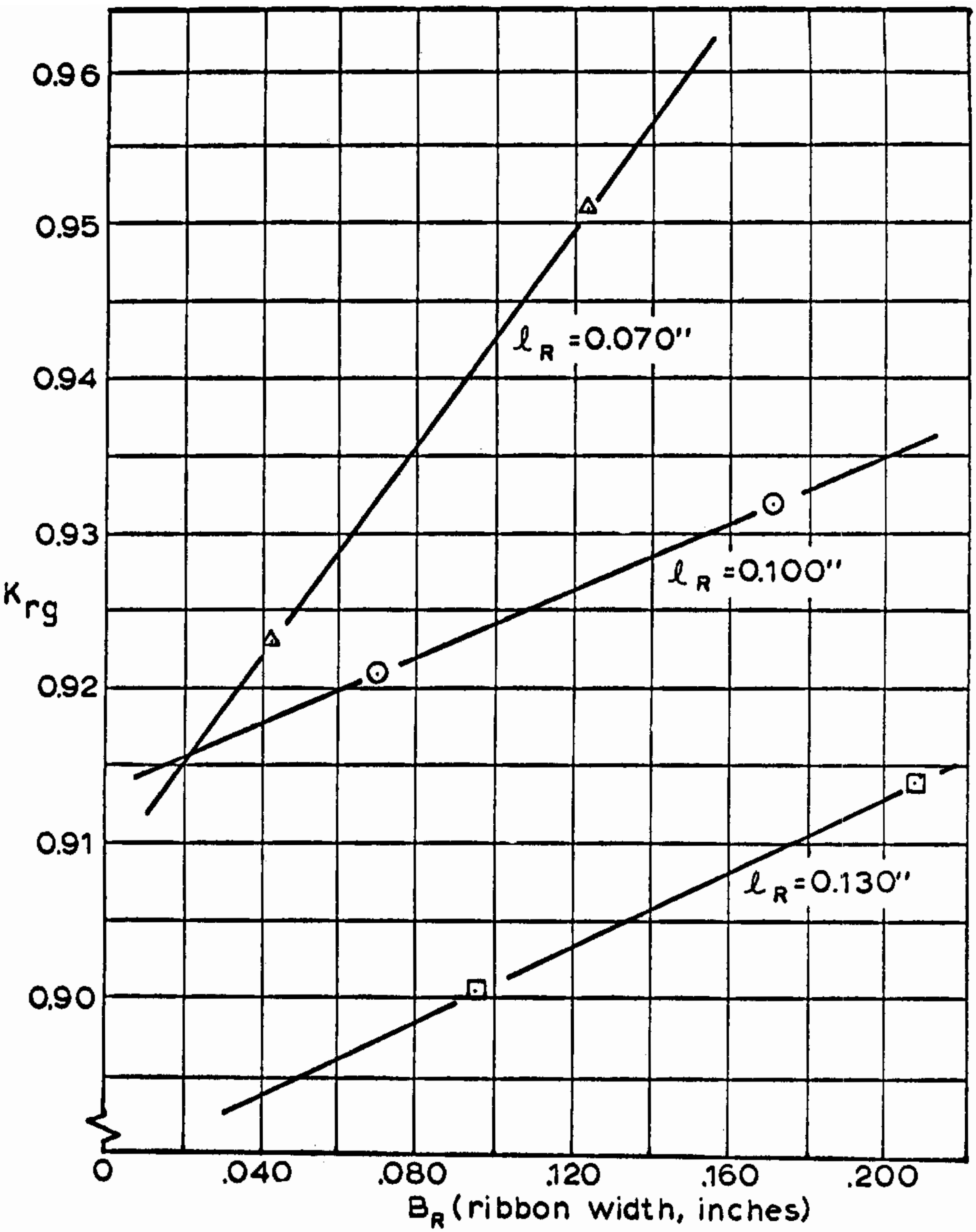

Fig 50. Flow Coefficient of Ribbon Grids as a Function of Grid Ribbon Width

APPENDIX III

$M_\infty \doteq 3.0$ WAKE SURVEY

Using a forty-nine (49) probe cruciform rake (Fig 51), a forebody wake survey was performed at Mach 3 for X/D_B = 6, 7, 8, and 9. Both the vertical plane and the horizontal plane (in which lie the support wings of the forebody) were surveyed. A similar pressure survey was conducted under freestream conditions at Mach 3.

The results of the survey are presented in Tables XVI to XVIII, and Figs 52 to 55, in terms of the local total pressure behind a normal shock, P_{O_ℓ}, to freestream total pressure ratio, P_{O_∞}; and the local static pressure, P_ℓ, to freestream total pressure ratio. The positions of the recompression shock waves indicated on these figures have been determined using Schlieren photographs.

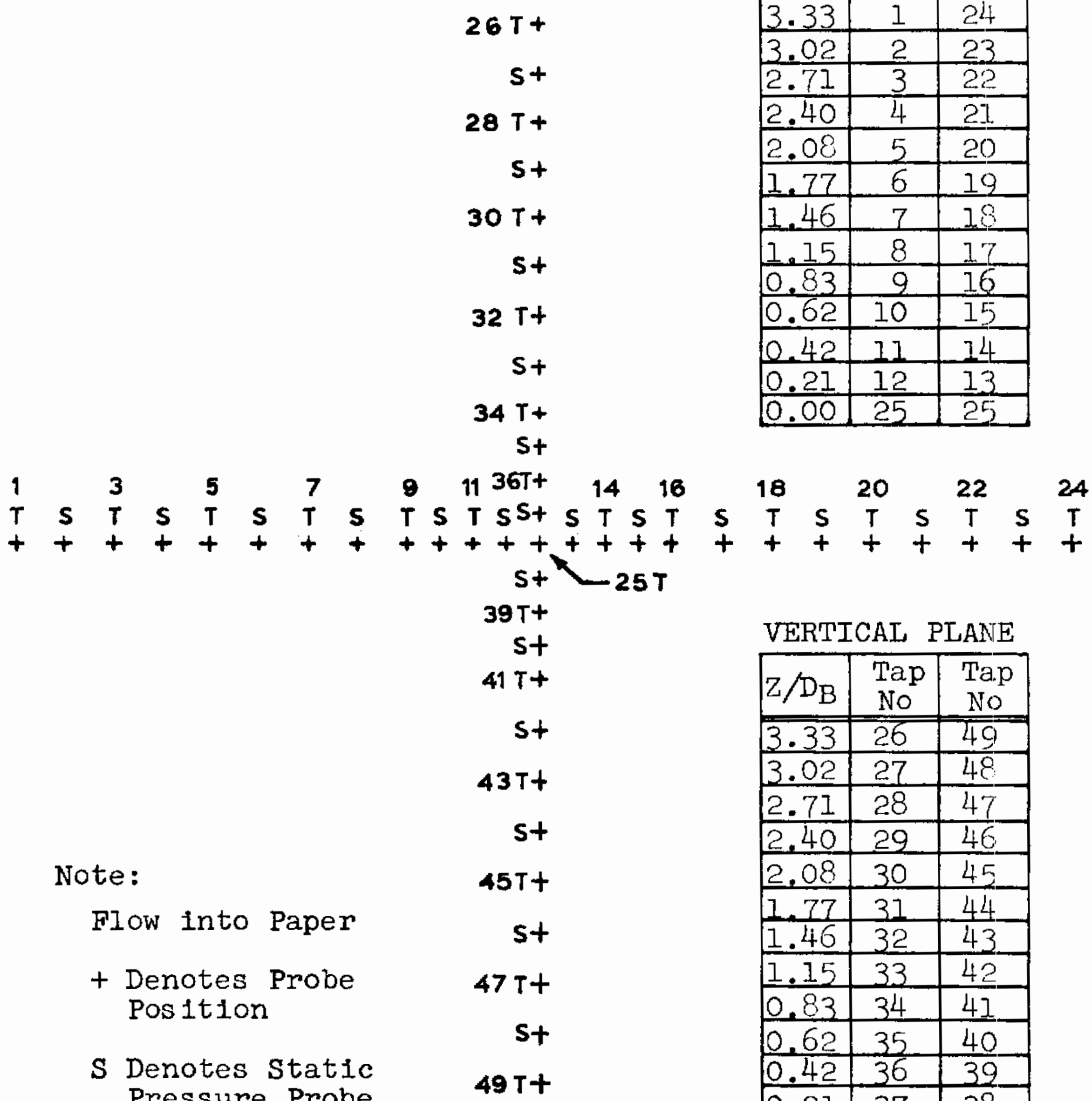

HORIZONTAL PLANE

Y/D_B	Tap No	Tap No
3.33	1	24
3.02	2	23
2.71	3	22
2.40	4	21
2.08	5	20
1.77	6	19
1.46	7	18
1.15	8	17
0.83	9	16
0.62	10	15
0.42	11	14
0.21	12	13
0.00	25	25

VERTICAL PLANE

Z/D_B	Tap No	Tap No
3.33	26	49
3.02	27	48
2.71	28	47
2.40	29	46
2.08	30	45
1.77	31	44
1.46	32	43
1.15	33	42
0.83	34	41
0.62	35	40
0.42	36	39
0.21	37	38
0.00	25	25

Note:

Flow into Paper

\+ Denotes Probe Position

S Denotes Static Pressure Probe

T Denotes Total Pressure Probe

Fig 51. Schematic of Cruciform Rake as Used for Forebody Wake Survey at $M_\infty \doteq 3.0$ (3/4 scale), and Dimensionless Rake Probe Location Relative to Center Line

TABLE XVI

Wake Pressure Ratios X/D_B = 6 and 7 ($M_\infty \doteq 3.0$)

$p'_{o\ell}/p_{o\infty}$, $X/D_B = 6$

Tap No	Horizontal Plane	Tap No	Vertical Plane
1	.2981	26	.3307
3	.3053	28	.2986
5	.2965	30	.2959
7	.3206	32	.3534
9	.3255	34	.3285
11	.3006	36	.2265
25	.2236	25	.2236
14	.3042	39	.2968
16	.3231	41	.3366
18	.3190	43	.3565
20	.2627	45	.3000
22	.2898	47	.3140
24	.2849	49	.3498

$p_\ell/p_{o\infty}$, $X/D_B = 6$

Tap No	Horizontal Plane	Tap No	Vertical Plane
2	.02626	27	.02424
4	.02409	29	.02315
6	.02215	31	.03203
8	.02878	33	.02914
10	.02791	35	.02720
12	.02770	37	.02720
13	.02777	38	.02734
15	.02899	40	.02777
17	.02806	42	.02986
19	.02164	44	.02193
21	.02489	46	.02215
23	.02626	48	.02734

$p'_{o\ell}/p_{o\infty}$, $X/D_B = 7$

Tap No	Horizontal Plane	Tap No	Vertical Plane
1	.3072	26	.3192
3	.2886	28	.3070
5	.2728	30	.3181
7	.3167	32	.3395
9	.3255	34	.3176
11	.2994	36	.2394
25	.2337	25	.2337
14	.2993	39	.2915
16	.3264	41	.3304
18	.3149	43	.3421
20	.2706	45	.2964
22	.2855	47	.2983
24	.2996	49	.3260

$p_\ell/p_{o\infty}$, $X/D_B = 7$

Tap No	Horizontal Plane	Tap No	Vertical Plane
2	.02945	27	.02132
4	.02140	29	.02154
6	.02745	31	.03306
8	.02766	33	.02687
10	.02737	35	.02521
12	.02594	37	.02608
13	.02608	38	.02550
15	.02716	40	.02608
17	.02716	42	.02680
19	.02716	44	.02766
21	.02269	46	.02190
23	.02565	48	.02348

TABLE XVII

Wake Pressure Ratios X/D_B = 8 and 9 ($M_\infty \doteq 3.0$)

$p'_{o\ell}/p_{o\infty}$, $X/D_B = 8$

Tap No	Horizontal Plane	Tap No	Vertical Plane
1	.3064	26	.2819
3	.2953	28	.2891
5	.3070	30	.3466
7	.3213	32	.3446
9	.3186	34	.3208
11	.2932	36	.2437
25	.2406	25	.2406
14	.2906	39	.2934
16	.3183	41	.3352
18	.3224	43	.3367
20	.3075	45	.3299
22	.2760	47	.2834
24	.2981	49	.2897

$p_\ell/p_{o\infty}$, $X/D_B = 8$

Tap No	Horizontal Plane	Tap No	Vertical Plane
2	.02408	27	.02011
4	.02292	29	.02480
6	.02645	31	.03323
8	.02667	33	.02768
10	.02602	35	.02588
12	.02610	37	.02588
13	.02573	38	.02566
15	.02660	40	.02688
17	.02595	42	.02725
19	.02652	44	.02581
21	.02379	46	.01903
23	.02357	48	.02011

$p'_{o\ell}/p_{o\infty}$, $X/D_B = 9$

Tap No	Horizontal Plane	Tap No	Vertical Plane
1	.3120	26	.2853
3	.2985	28	.2998
5	.3117	30	.3124
7	.3216	32	.3223
9	.3134	34	.3141
11	.2905	36	.2504
25	.2439	25	.2439
14	.2931	39	.2857
16	.3124	41	.3240
18	.3173	43	.3162
20	.3060	45	.3117
22	.2901	47	.2844
24	.3128	49	.2921

$p_\ell/p_{o\infty}$, $X/D_B = 9$

Tap No	Horizontal Plane	Tap No	Vertical Plane
2	.02266	27	.01864
4	.02684	29	.02403
6	.02705	31	.03706
8	.02669	33	.02605
10	.02576	35	.02525
12	.02569	37	.02504
13	.02569	38	.02525
15	.02609	40	.02576
17	.02648	42	.02569
19	.02691	44	.02353
21	.02734	46	.02267
23	.02209	48	.02072

TABLE XVIII

Wake Pressure Ratios $X/D_B = \infty$ ($M_\infty \doteq 3.0$)

$p'_{o\ell}/p_{o\infty}$, $X/D_B = \infty$

Tap No	Horizontal Plane	Tap No	Vertical Plane
1	.3390	26	.3220
3	.2849	28	.3111
5	.3351	30	.3120
7	.3283	32	.3201
9	.3346	34	.3280
11	.3291	36	.3280
25	.3286	25	.3286
14	.3330	39	.3292
16	.3322	41	.3229
18	.3339	43	.3126
20	.3353	45	.3108
22	.3363	47	.3263
24	.3385	49	.3334

$p_\ell/p_{o\infty}$, $X/D_B = \infty$

Tap No	Horizontal Plane	Tap No	Vertical Plane
2	.02678	27	.02392
4	.02693	29	.02377
6	.02627	31	.03493
8	.02685	33	.02553
10	.02605	35	.02612
12	.02583	37	.02575
13	.02583	38	.02627
15	.02627	40	.02583
17	.02590	42	.02451
19	.02620	44	.02333
21	.02730	46	.02407
23	.02700	48	.02612

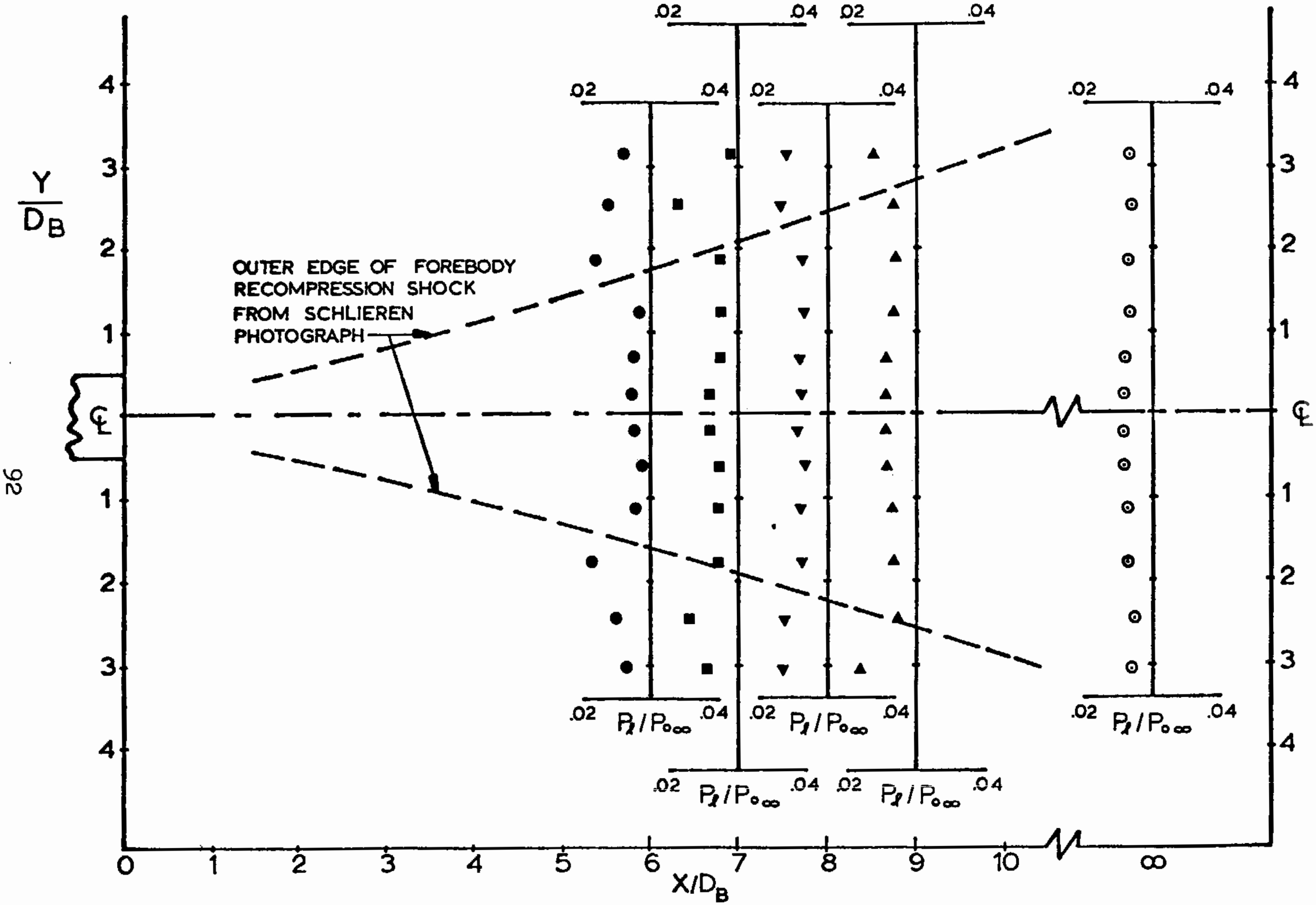

Fig 52. Wake Static to Freestream Total Pressure Ratios in the Horizontal Plane ($M_\infty \doteq 3.0$)

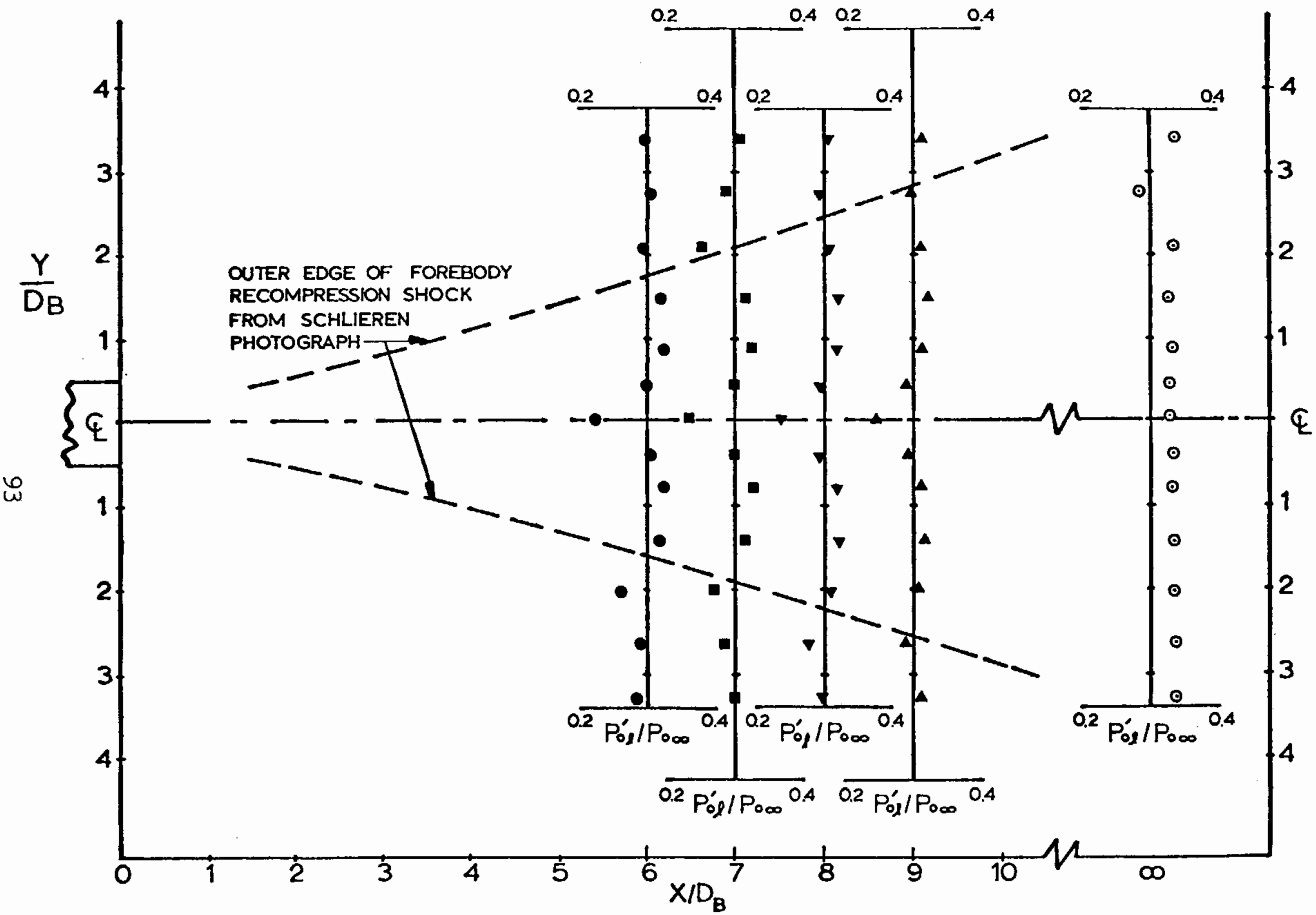

Fig 53. Wake Total Pressure Ratios in the Horizontal Plane ($M_\infty \doteq 3.0$)

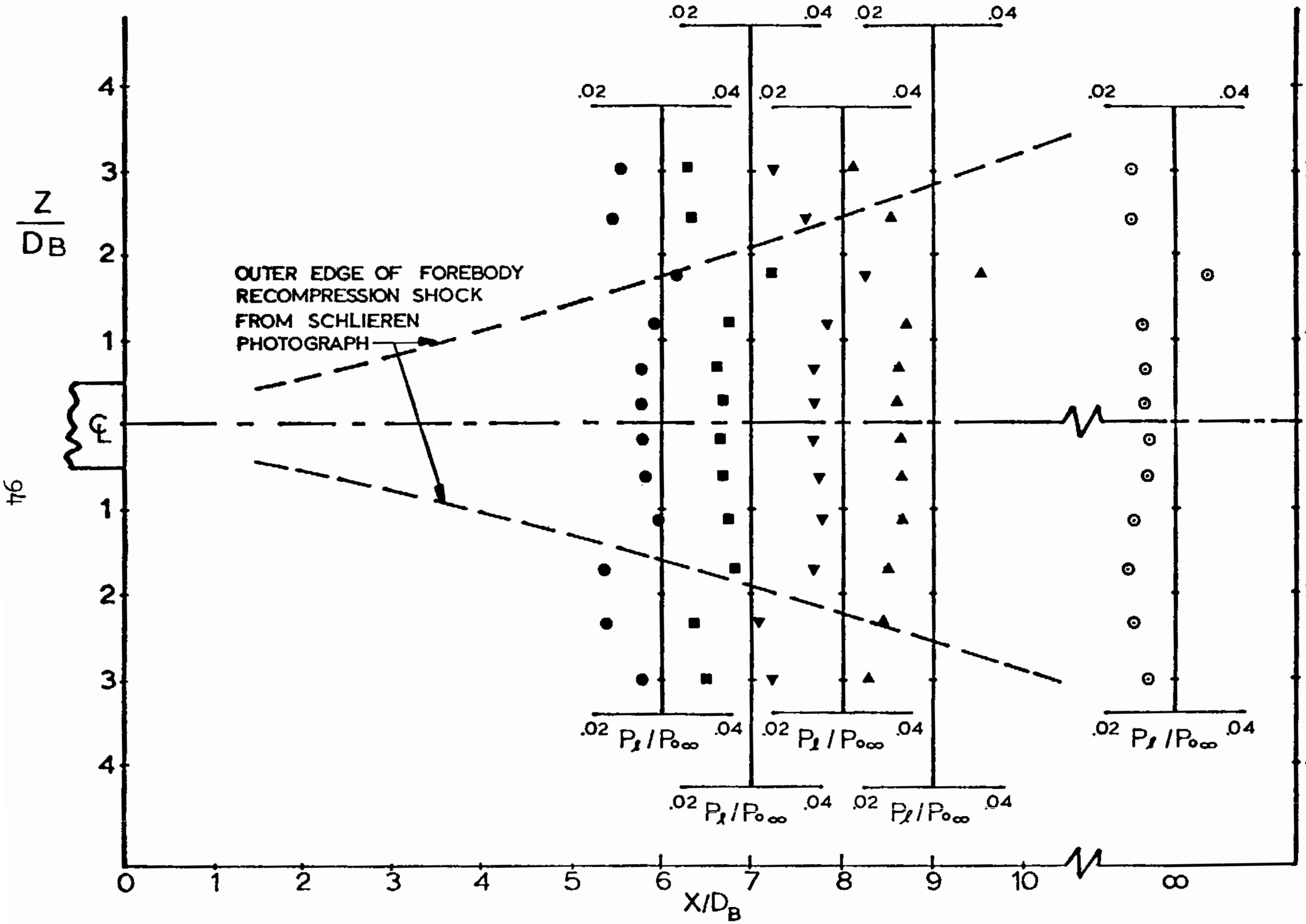

Fig 54. Wake Static to Freestream Total Pressure Ratios in the Vertical Plane ($M_\infty \doteq 3.0$)

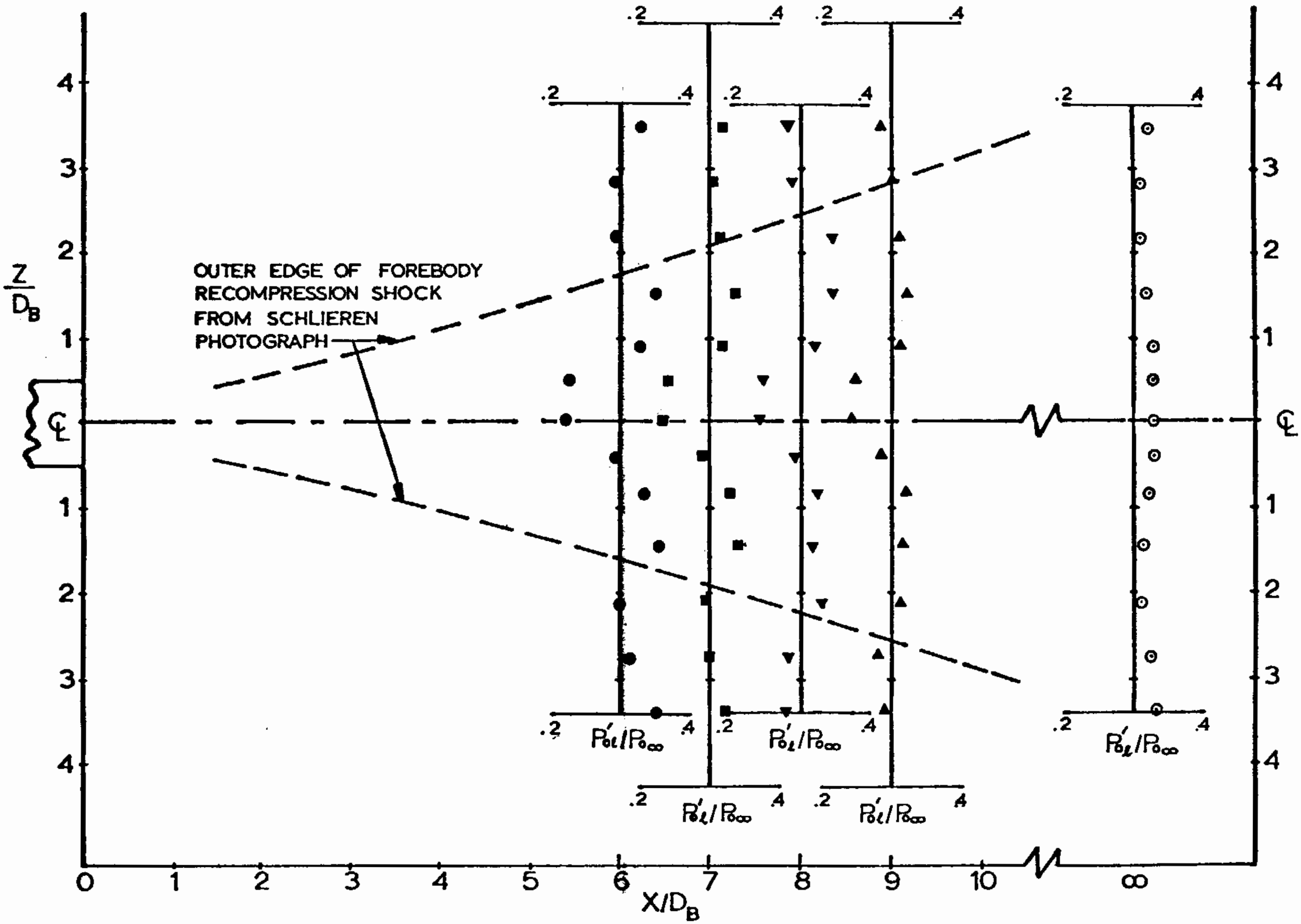

Fig 55. Wake Total Pressure Ratios in the Vertical Plane ($M_\infty \doteq 3.0$)

UNCLASSIFIED
Security Classification

DOCUMENT CONTROL DATA - R&D

(Security classification of title, body of abstract and indexing annotation must be entered when the overall report is classified)

1. ORIGINATING ACTIVITY *(Corporate author)* University of Minnesota Minneapolis, Minnesota 55455	2a. REPORT SECURITY CLASSIFICATION UNCLASSIFIED 2b. GROUP N/A

3. REPORT TITLE

Pressure Distribution Measurements on Several Rigid Hyperflo Models at Mach 3.0 and 4.0

4. DESCRIPTIVE NOTES *(Type of report and inclusive dates)*

Final Report May 1966 - May 1967

5. AUTHOR(S) *(Last name, first name, initial)*

Noreen, R. A.
Hosker, R. P.

6. REPORT DATE	7a. TOTAL NO. OF PAGES	7b. NO. OF REFS
September 1967	95	5

8a. CONTRACT OR GRANT NO. AF33(615)-5029 b. PROJECT NO. 6065 c. Task No. 606503 d.	9a. ORIGINATOR'S REPORT NUMBER(S) None 9b. OTHER REPORT NO(S) *(Any other numbers that may be assigned this report)* AFFDL-TR-67-84

10. AVAILABILITY/LIMITATION NOTICES

This document is subject to special export controls and each transmittal to foreign governments or foreign nationals may be made only with prior approval of the Air Force Flight Dynamics Laboratory.

11. SUPPLEMENTARY NOTES	12. SPONSORING MILITARY ACTIVITY
	AFFDL (FDFR) Wright-Patterson AFB, Ohio 45433

13. ABSTRACT

The internal and external surface pressures on rigid wind tunnel models of Hyperflo canopies of 5%, 10%, and 15% geometric porosity, with mesh and grid porous areas, were measured, and Schlieren flow photographs were taken. The measurements were conducted in a 12 in. x 12 in. supersonic wind tunnel in free-stream and in the wake of a cone-cylinder forebody at Mach numbers of 3.0 and 4.0 and Reynolds numbers/ft. from 0.86×10^6 to 2.99×10^6.

DD FORM 1 JAN 64 1473

UNCLASSIFIED
Security Classification

UNCLASSIFIED
Security Classification

14. KEY WORDS	LINK A		LINK B		LINK C	
	ROLE	WT	ROLE	WT	ROLE	WT
Supersonic						
Pressure Distribution						
Supersonic Parachute						
Wind Tunnel Tests						
Hyperflo						

INSTRUCTIONS

1. ORIGINATING ACTIVITY: Enter the name and address of the contractor, subcontractor, grantee, Department of Defense activity or other organization *(corporate author)* issuing the report.

2a. REPORT SECURITY CLASSIFICATION: Enter the overall security classification of the report. Indicate whether "Restricted Data" is included. Marking is to be in accordance with appropriate security regulations.

2b. GROUP: Automatic downgrading is specified in DoD Directive 5200.10 and Armed Forces Industrial Manual. Enter the group number. Also, when applicable, show that optional markings have been used for Group 3 and Group 4 as authorized.

3. REPORT TITLE: Enter the complete report title in all capital letters. Titles in all cases should be unclassified. If a meaningful title cannot be selected without classification, show title classification in all capitals in parenthesis immediately following the title.

4. DESCRIPTIVE NOTES: If appropriate, enter the type of report, e.g., interim, progress, summary, annual, or final. Give the inclusive dates when a specific reporting period is covered.

5. AUTHOR(S): Enter the name(s) of author(s) as shown on or in the report. Enter last name, first name, middle initial. If military, show rank and branch of service. The name of the principal author is an absolute minimum requirement.

6. REPORT DATE: Enter the date of the report as day, month, year; or month, year. If more than one date appears on the report, use date of publication.

7a. TOTAL NUMBER OF PAGES: The total page count should follow normal pagination procedures, i.e., enter the number of pages containing information.

7b. NUMBER OF REFERENCES: Enter the total number of references cited in the report.

8a. CONTRACT OR GRANT NUMBER: If appropriate, enter the applicable number of the contract or grant under which the report was written.

8b, 8c, & 8d. PROJECT NUMBER: Enter the appropriate military department identification, such as project number, subproject number, system numbers, task number, etc.

9a. ORIGINATOR'S REPORT NUMBER(S): Enter the official report number by which the document will be identified and controlled by the originating activity. This number must be unique to this report.

9b. OTHER REPORT NUMBER(S): If the report has been assigned any other report numbers *(either by the originator or by the sponsor)*, also enter this number(s).

10. AVAILABILITY/LIMITATION NOTICES: Enter any limitations on further dissemination of the report, other than those imposed by security classification, using standard statements such as:

(1) "Qualified requesters may obtain copies of this report from DDC."

(2) "Foreign announcement and dissemination of this report by DDC is not authorized."

(3) "U. S. Government agencies may obtain copies of this report directly from DDC. Other qualified DDC users shall request through ______________."

(4) "U. S. military agencies may obtain copies of this report directly from DDC. Other qualified users shall request through ______________."

(5) "All distribution of this report is controlled. Qualified DDC users shall request through ______________."

If the report has been furnished to the Office of Technical Services, Department of Commerce, for sale to the public, indicate this fact and enter the price, if known.

11. SUPPLEMENTARY NOTES: Use for additional explanatory notes.

12. SPONSORING MILITARY ACTIVITY: Enter the name of the departmental project office or laboratory sponsoring *(paying for)* the research and development. Include address.

13. ABSTRACT: Enter an abstract giving a brief and factual summary of the document indicative of the report, even though it may also appear elsewhere in the body of the technical report. If additional space is required, a continuation sheet shall be attached.

It is highly desirable that the abstract of classified reports be unclassified. Each paragraph of the abstract shall end with an indication of the military security classification of the information in the paragraph, represented as *(TS)*, *(S)*, *(C)*, or *(U)*.

There is no limitation on the length of the abstract. However, the suggested length is from 150 to 225 words.

14. KEY WORDS: Key words are technically meaningful terms or short phrases that characterize a report and may be used as index entries for cataloging the report. Key words must be selected so that no security classification is required. Identifiers, such as equipment model designation, trade name, military project code name, geographic location, may be used as key words but will be followed by an indication of technical context. The assignment of links, rules, and weights is optional.

UNCLASSIFIED
Security Classification